Correlation Effects in the Electronic Structure of Transition Metals and Their Compounds

een wetenschappelijke proeve op het gebied van de
Natuurwetenschappen, Wiskunde en Informatica

Proefschrift

ter verkrijging van de graad van doctor
aan de Radboud Universiteit Nijmegen,
op gezag van de rector magnificus prof. mr. S. C. J. J. Kortmann,
volgens besluit van het College van Decanen
in het openbaar te verdedigen op woensdag 23 september 2009
om 10.30 uur precies

door

Igor Di Marco

geboren op 24 april 1978
te Teramo, Italië

Promotor:

    Prof. dr. M. I. Katsnelson

Manuscriptcommissie:

    Prof. dr. T. Rasing (voorzitter)

    Prof. dr. O. Eriksson (Uppsala University)

    Prof. dr. A. I. Lichtenstein (Hamburg University)

Contents

List of acronyms

DFT   Density Functional Theory

DMFT   Dynamical Mean-Field Theory

LDA   Local Density Approximation

LSDA   Local Spin Density Approximation

GGA   Generalized Gradient Approximation

SIC   Self-Interaction Correction

CPA   Coherent Potential Approximation

DLM   Disordered Local Moments

ASA   Atomic Sphere Approximation

FP   Full Potential

LMTO   Liner Muffin-Tin Orbital

NMTO   Nth order Muffin-Tin Orbital

KKR   Korringa-Kohn-Rostoker

USPP-APW   UltraSoft Pseudopotential Projector Augmented Plane-Wave

SPTF   Spin-Polarized T-matrix Fluctuation-Exchange

NCA   Non-Crossing Approximation

OCA   One-Crossing Approximation

IPT   Iterative Perturbation Theory

QMC   Quantum Monte-Carlo

HIA   Hubbard I Approximation

RPA   Random Phase Approximation

AMF   Around Mean-Field

AL   Atomic Limit

FM   FerroMagnetic

AFM   AntiFerroMagnetic

STS   Scanning Tunnelling Spectroscopy

XPS   X-ray Photoelectron Spectroscopy

Chapter 1

Introduction

The description of condensed matter can be often related to microscopic models governed by the rules of quantum mechanics. Moreover in solid state theory the electronic problem can be decoupled from the nuclear problem, because of the large difference between the corresponding masses and thus time-scales (Born-Oppenheimer approximation). Then our task becomes *simply* to solve the Schrödinger equation for the many-body Hamiltonian[1]

$$\hat{H} = -\frac{\hbar^2}{2m}\sum_i \nabla_i^2 + \sum_{i,I}\frac{Z_I e^2}{|\mathbf{r}_i - \mathbf{R}_I|} + \frac{1}{2}\sum_{i\neq j}\frac{e^2}{|\mathbf{r}_i - \mathbf{r}_j|}\;, \qquad (1.1)$$

where the electrons, with mass m, are denoted with the lower case subscript and the nuclei are denoted with the upper case subscript. We have three terms to analyze: the kinetic energy of the electrons, the potential due to the nuclei and the mutual Coulomb repulsion between the electrons themselves. It is exactly this last term that makes the problem extremely complicated, correlating the motion of all the electrons. As a result an exact solution can be obtained for at most a few tens of particles, surely not enough for the description of a real solid, where the components are of the order of the Avogadro number 10^{23}.

Given the impossibility of an exact solution, we have two options to access the physical information about our system. The first way, adopted by the community of many-body physics, is to simplify the Hamiltonian (1.1) with the exclusion of secondary degrees of freedom, obtaining a model that we can solve more or less exactly. The second possible way is to work directly with the full Hamiltonian, looking for an approximate solution. The last approach has been adopted by the electronic structure community: the many-body problem is solved within a single-particle scheme where every electron moves in a time-averaged potential determined by the nuclei and the other electrons. This is the assumption behind the density-functional theory in local density approximation (DFT-LDA)[2] [1, 2, 3]

---

[1]For simplicity we have neglected relativistic effects associated to the spin-orbit coupling

[2]In principle it is true also for other functionals commonly used in the Kohn-Sham equations.
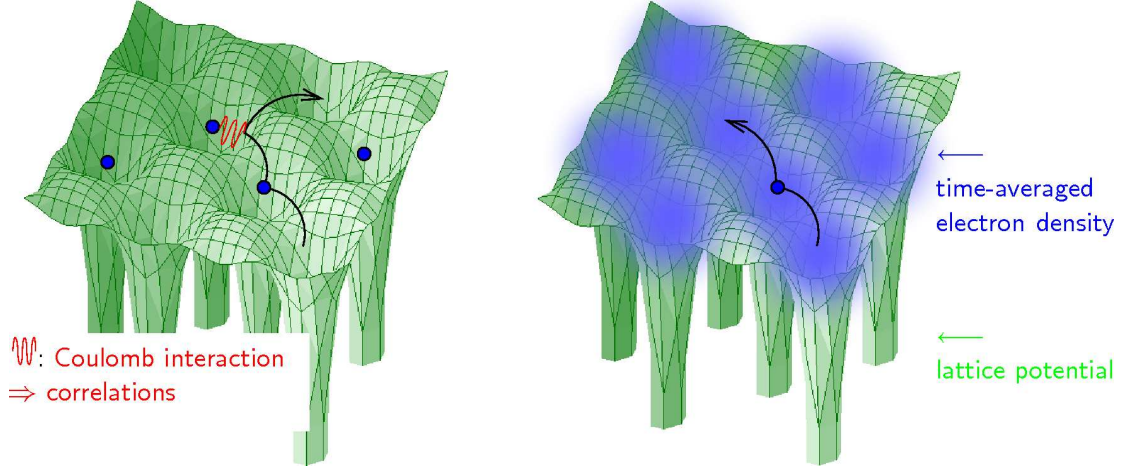
Figure 1.1: Left side: the electrons (blue points) move into the potential wells of the crystal (green manifold). In case of electronic localization, it becomes important to know the behavior of all the electrons, since they strongly influence on each other via Coulomb repulsion (red wiggled line). Right side: In DFT-LDA a given electron (blue point) moves in the potential of the nuclei and in an effective time-averaged potential due to the other electrons (blue clouds). Picture from Ref. [5]

and, while it can appear rather drastic, gives an excellent description of various solids, in particular sp bonded. In fact, due to the Bloch theorem, the electrons can be considered delocalized along the whole crystal, fitting with the picture of an effective potential.

Nevertheless there exist some materials where the electrons, usually associated with narrow d and f bands, can acquire more localized character by spending more time around a given atom. In this case the behavior of the real system becomes very different from the one-particle approximation of DFT-LDA, as depicted respectively at the left and right sides of Figure 1.1. Because of the strong Coulomb repulsion, the motion of a given electron is substantially influenced by the presence of all the other electrons around. We speak, then, of a strongly correlated system [4, 5].

These qualitative arguments can be reformulated in a more rigorous way with the help of a simplified Hubbard model [6, 7, 8]. Let us consider electrons in a generic lattice of single-level ions (see Figure 1.2) whose Hamiltonian in second quantization reads

$$\hat{H}_{hub} = -t \sum_{\mathbf{R},\mathbf{R}'} \hat{c}^{\dagger}_{\mathbf{R},\sigma}\hat{c}_{\mathbf{R}',\sigma} + U \sum_{\mathbf{R}} \hat{n}_{\mathbf{R},\uparrow}\hat{n}_{\mathbf{R},\downarrow}, \qquad (1.2)$$

and where for simplicity the first sum is intended only between nearest neighbors. Two parameters determine the behavior of the system. The hopping parameter t
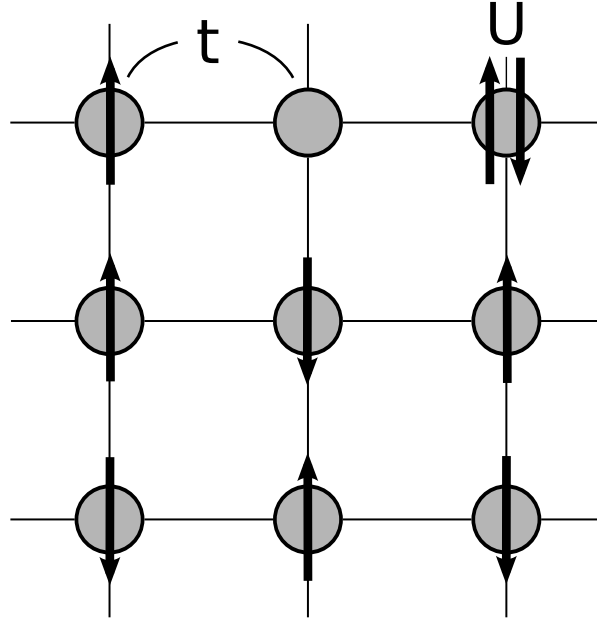
Figure 1.2: The single-orbital Hubbard model consists of a lattice of ions where the electrons are represented in tight-binding scheme: t is the kinetic energy gained moving between nearest neighbors (upper left corner) and U is energy cost for a double occupation (upper right corner) due to the local Coulomb repulsion. At half-filling, if $U \gg t$, the electrons do not find it energetically favorable to move from site to site and the system turns into a Mott insulator (bottom).

is the energy gained by an electron jumping from site to site, and quantifies the tendency to the delocalization. The Hubbard U is the energy due to the local Coulomb repulsion, that is the cost in energy for accommodating two electrons with different spins on the same site. This parameter expresses the tendency to the localization: if U is too strong the electrons cannot move any more and they are forced to stay at their own site, as shown at the bottom of Figure 1.2 for an half-filled lattice. Then the system becomes a Mott insulator [9, 10].

Besides its apparent simplicity, the Hubbard model contains all the fascinating physics based on the competition between itinerant and localized character of the electrons, and is a good prototype for studying correlation effects in real materials. A significant difference is that in a real material t is orbital-dependent and not only limited to nearest neighboring sites, then the more accessible bandwidth W is usually used as significant parameter. After having specified the energy scales of the problem, we can individuate three regimes of correlations associated to the ratio U/W. When U/W is small, the electrons retain much of their wave-like

character and the system behaves as a weakly correlated metal. An analysis based on DFT-LDA is appropriate and usually successful. On the other hand when U/W is big, the electrons acquire a more particle-like character and the hopping from site to site becomes impossible: the system turns into a Mott insulator and a description based on waves in the **k**-space is not sufficient any more. However, as we have seen above, an equivalently simple description based on the real space can be formulated: the problem is still reducible to a single-particle system, as in the self-interaction correction (SIC) [11] method or in the LDA+U [12, 13] approach. The most difficult task is to treat systems where U and W are of the same order: in this case the electrons hesitate between being itinerant and being localized [4], and we need an approach able to catch phenomena on different time scales. The dynamics visualized at the left hand side of Figure 1.1 must be taken into account and this is not possible with single-particle methods, where all the fluctuations are frozen.

The dynamical mean-field theory (DMFT) has represented a breakthrough for the study of strongly correlated materials [14, 15]. In the DMFT the complicated lattice problem is solved non-perturbatively by mapping it onto a Single-Impurity Anderson model [16]. It means that the environment surrounding a given atom is replaced by an effective fermionic bath to be determined self-consistently. The idea is similar [4] to the Weiss theory of molecular field for the Ising model, but in the DMFT the effective medium is a fully dynamical quantum object. As a result genuine many-body effects are considered, e.g. temperature-dependent spin fluctuations, and the interesting physics at the crossover of the Mott metal-insulator transition can be studied. Although originally designed for effective models, the DMFT can be easily combined with DFT-LDA to describe realistic materials with local Coulomb correlations: the resulting LDA+DMFT scheme [17, 18] is presently the most universal practical *ab-initio* technique for calculating the electronic structure of a solid in any of the three U/W regimes specified above.

In the last decade the LDA+DMFT scheme has been successfully applied to a number of important problems. The most famous results include the calculation of the ground-state properties and the excitation spectrum of δ-Pu [19, 20, 21, 22, 23], the explanation of the volume-collapse associated to the α-γ transition in cerium [24, 25, 26] and the investigation of the itinerant magnetism and the spectral properties of the late transition metals Fe and Ni [27, 28, 29]. Other important studies concern the half-metallic ferromagnets [30, 31], the control of the metal-insulator transition in Cr doped V_2O_3 [32], and many others transition metals oxides, e.g. the superconducting Sr_2RuO_4 [33] or the heavy-fermion compound LiV_2O_4 [34]. Within this last class of systems, it is also worth to mention the recent study of the paradigmatic heavy-fermion material $CeIrIn_5$ [35].

Despite all success stories of LDA+DMFT, the method is still less than a decade old and at a stage of active development. Most available implementations

apply some drastic simplifications, and in particular, many LDA+DMFT codes are embedded into atomic sphere approximation (ASA)-based LDA codes. Two examples are the linear muffin-tin orbital (LMTO)-ASA code of Ref. [18] and the Korringa-Kohn-Rostoker (KKR)-ASA code of Ref. [36]. These schemes might work well for close-packed crystal structures, but they are insufficient for open structures and low-dimensional geometries.

The present thesis is dedicated to the study of real strongly correlated materials by means of an appositely developed LDA+DMFT code based on the full-potential (FP) LMTO method of Ref. [37], which does not suffer from the limitations mentioned in the previous paragraph.

The result of our work will be presented in the following way. Being Chapter 1 this introduction, Chapter 2 discusses the main theoretical framework: the density functional theory in local density approximation, and the reasons behind its successes or its failures. Finally the LDA+DMFT scheme is introduced through a parallelism with the Weiss molecular field theory. In Chapter 3 we treat the technical details of our implementation. After a brief derivation of the generic LMTO method, the computational expressions used in our code are given. Special attention is given to the interface between the DFT and the DMFT parts of the code, including the shape of the correlated orbitals and the LDA+DMFT equations. Chapter 4 concerns the single-particle excitations of the bulk late transition metals: Fe, Co and Ni. While these systems can be considered as weakly correlated metals, still some important correlations effects can be observed such as the shrinking of the $3d$ band and the formation of non-coherent satellites in the photoemission spectrum. In Chapter 5 our study is extended to the surfaces of Fe, Co and Ni, and comparison is made with the corresponding bulk systems, showing an increase of the correlation effects. The role of the surface states is analyzed in the last Section of the Chapter, when the theoretical results are compared with experimental data from photoemission spectroscopy. Then, in Chapter 6, we focus on the formation of a pseudo-gap in the density of states of a monolayer of Fe on the surface (001) of W. Experimental data from Scanning Tunneling Spectroscopy (STS) are compared with our calculations, showing a reasonable agreement. Chapter 7 is dedicated to the calculation of the ground state properties in the LDA+DMFT scheme. The implementation of the corresponding total energy functional is described in details, and results are shown for ferromagnetic Ni and antiferromagnetic Mn. The latter element is also the object of Chapter 8: because of the stronger correlation effects, we analyze the dependence of the results of the LDA+DMFT scheme on the magnetic phase and on the method used to solve the effective impurity model. Moreover the possibility of a combination of the LDA+DMFT scheme and the disordered local moment (DLM) approach is presented, together with an application to the photoemission spectrum within the one-step model. Finally Chapter 9 contains the last project included in this

Mott
transition

U/W

Fe Co Ni
bulk
(Chap. 4)

1 ML of Fe
on W(001)
(Chap.6)

SmB$_6$
YbB$_{12}$
YbInCu$_4$
(Chap. 9)

Fe Co Ni
surface
(Chap. 5)

Mn
bulk
(Chap. 7-8)
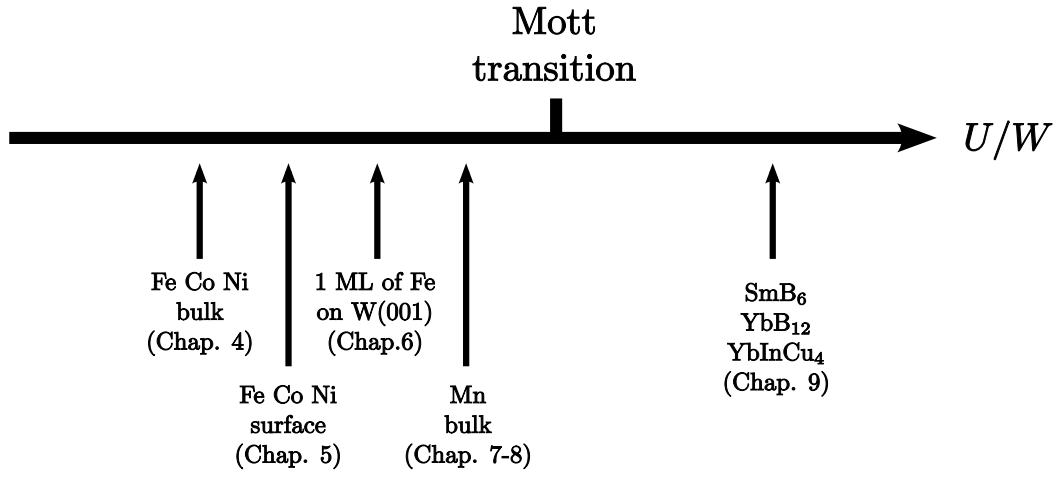
Figure 1.3: An overview of the real materials studied in the present thesis, with reference to the corresponding Chapters. The systems are ordered in terms of the degree of correlation with respect to the critical value for the Mott metal-insulator transition.

work: a study of the mixed-valence compounds SmB$_6$, YbB$_{12}$ and YbInCu$_4$ in the Hubbard I approximation.

A summary of the previous overview is given in Figure 1.3: the systems are ordered in terms of the degree of correlation with respect to the critical value for the Mott metal-insulator transition.

Chapter 2

Theoretical methods

In this Chapter we present the main theoretical framework of the LDA+DMFT scheme for the electronic structure calculation of strongly correlated materials. The density-functional theory and the Kohn-Sham equations are illustrated in details. Then we focus on the local density approximation and the reasons of its successes in terms of the exchange-correlation hole. Finally we introduce the LDA+U Hamiltonian as correction to the bare DFT-LDA Hamiltonian, and the dynamical mean-field theory is explained as analogy to the Weiss theory of the molecular field.

2.1 Density functional theory

The idea of describing a system of many electrons in terms of the corresponding charge density was introduced for the first time in the method that Thomas and Fermi [38, 39] proposed in 1927[1]. Although their approximation is not accurate enough for the computational standards of the modern condensed matter physics, they suggested that the calculation of the ground state properties of a quantum system can be made without requiring the knowledge of the full many-body wavefunction. The modern density-functional theory is based on two theorems proved in the mid-sixties by Hohenberg and Kohn [1] to reformulate the seminal intuition of Thomas and Fermi as an exact theory of many-body systems. The formulation can be applied to any system of interacting particles in an external potential $V_{ext}(\mathbf{r})$, whose Hamiltonian can be written as

$$\hat{H} = -\frac{\hbar^2}{2m} \sum_i \nabla_i^2 + \sum_i V_{ext}(\mathbf{r}_i) + \frac{1}{2} \sum_{i \neq j} \hat{V}_{int}(\mathbf{r}_i, \mathbf{r}_j) \,, \qquad (2.1)$$

---

[1]Later, in 1930, Dirac [40] extended their approximation to include the exchange term due to the statistics of indistinguishable particles

$$V_{ext}(\mathbf{r}) \xleftarrow{\quad \text{HK THEOREM} \quad} n_0(\mathbf{r})$$

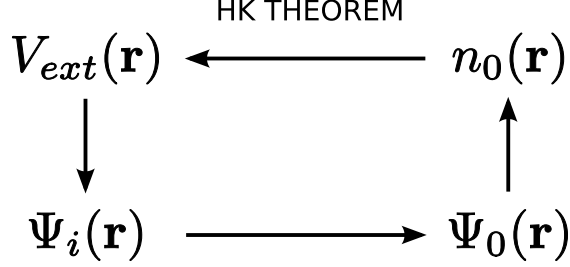$$\Psi_i(\mathbf{r}) \xrightarrow{\hspace{3cm}} \Psi_0(\mathbf{r})$$

Figure 2.1: Meaning of the Hohenberg-Kohn theorem in a quantum-mechanical hierarchy of observables. The external potential V_{ext} determines the Hamiltonian and then all the states Ψ_i of the system, including the ground state Ψ_0. This eigenfunction describes all the properties of the system, and then also the electron density n_0. The circle is closed by the Hohenberg-Kohn theorem that relates the external potential to the ground state electron density.

where the index i enumerates the particles and $\mathbf{r}_i$ their positions. For our purposes we contextualize the discussion to the Coulomb interaction potential:

$$\hat{V}_{int}(\mathbf{r}_i, \mathbf{r}_j) = \frac{e^2}{|\mathbf{r}_i - \mathbf{r}_j|}. \tag{2.2}$$

The first theorem of Hohenberg and Kohn states that *there is a one-to-one correspondence between $V_{ext}(\mathbf{r})$ and the ground-state density $n(\mathbf{r})$, up to a constant shift of the potential.*

The proof is disarmingly trivial, in particular if we limit the demonstration to a non-degenerate ground state. Under this assumption it becomes obvious that $V_{ext}(\mathbf{r})$ determines uniquely the ground-state wavefunction Ψ, and then $n_0(\mathbf{r})$, as reported in the scheme of Figure 2.1. The fact that $n_0(\mathbf{r})$ determines only one $V_{ext}(\mathbf{r})$ is proved as *reductio absurdum*. Suppose that two external potentials $V_{ext}^{(1)}$ and $V_{ext}^{(2)}$ exist such that $V_{ext}^{(1)} \neq V_{ext}^{(2)}$ and that they lead to the same ground-state density $n_0(\mathbf{r})$. If the difference is more than a constant, these potentials generate two different Hamiltonians $\hat{H}^{(1)} \neq \hat{H}^{(2)}$ which have two different ground-state wavefunctions $\Psi^{(1)} \neq \Psi^{(2)}$ that, as we supposed, are associated to the same $n_0(\mathbf{r})$. The variational principle states that the minimum expectation value of the Hamiltonian is obtained for its ground-state wavefunction, then it is straightforward to show that

$$E^{(1)} = \langle \Psi^{(1)} | \hat{H}^{(1)} | \Psi^{(1)} \rangle < \langle \Psi^{(2)} | \hat{H}^{(1)} | \Psi^{(2)} \rangle . \tag{2.3}$$

With a little bit of algebra we can rewrite the expectation value of the first Hamil-

tonian in the ground-state of the second Hamiltonian as

$$\langle \Psi^{(2)} | \hat{H}^{(1)} | \Psi^{(2)} \rangle = \langle \Psi^{(2)} | \hat{H}^{(2)} | \Psi^{(2)} \rangle - \langle \Psi^{(2)} | \hat{H}^{(2)} - \hat{H}^{(1)} | \Psi^{(2)} \rangle \tag{2.4}$$

$$= \langle \Psi^{(2)} | \hat{H}^{(2)} | \Psi^{(2)} \rangle - \int d\mathbf{r} \, [V_{ext}^{(2)}(\mathbf{r}) - V_{ext}^{(1)}(\mathbf{r})] n_0(\mathbf{r}) \tag{2.5}$$

Furthermore we can repeat the same procedure for $\hat{H}^{(2)}$, obtaining the following system of equations:

$$
\begin{aligned}
E^{(1)} &< E^{(2)} - \int d\mathbf{r} \, [V_{ext}^{(2)}(\mathbf{r}) - V_{ext}^{(1)}(\mathbf{r})] n_0(\mathbf{r}) \\
E^{(2)} &< E^{(1)} - \int d\mathbf{r} \, [V_{ext}^{(1)}(\mathbf{r}) - V_{ext}^{(2)}(\mathbf{r})] n_0(\mathbf{r}) \, .
\end{aligned}
\tag{2.6}
$$

If now we add together the previous equations, we arrive at the contradictory inequality

$$E^{(1)} + E^{(2)} < E^{(1)} + E^{(2)} \, , \tag{2.7}$$

demonstrating the desired result.

An important corollary descends from the first theorem of Hohenberg and Kohn: since the Hamiltonian is fully determined by $n_0(\mathbf{r})$, then all the eigenfunctions are fully determined by $n_0(\mathbf{r})$ and so all the properties of the system, including non ground-state properties. This is a not trivial consequence of the Hohenberg and Kohn's construction, and we will come back to this point during the discussion of the operative application of the density functional theory.

The second theorem of Hohenberg and Kohn states that *for a given $V_{ext}(\mathbf{r})$ an energy functional of the density $n(\mathbf{r})$ can be defined such as its minimum is the ground-state energy of the system, and this energy is obtained for the ground-state density $n_0(\mathbf{r})$.* The proof is based on the corollary to the first theorem: if all the properties are uniquely determined when $n_0(\mathbf{r})$ is given, then also the kinetic energy T and the particle-particle interaction energy E_{int} are completely determined. As a result, the ground state energy can be written by means of the following density functional

$$E_{HK}[n] = T[n] + E_{int}[n] + \int d\mathbf{r} \, V_{ext}(\mathbf{r}) n(\mathbf{r}), \tag{2.8}$$

evaluated for $n(\mathbf{r}) = n_0(\mathbf{r})$. Furthermore this functional can be easily shown to be variational. Consider a system whose ground-state density is $n^{(1)}(\mathbf{r})$, corresponding to an external potential $V_{ext}^{(1)}$ and to an Hamiltonian $\hat{H}^{(1)}$. Following the definition of the functional E_{HK}, it is clear that it is equal to the expectation value of $\hat{H}^{(1)}$ in its unique ground-state wavefunction $\Psi^{(1)}$ associated to $n^{(1)}(\mathbf{r})$:

$$E^{(1)} = E_{HK}[n^{(1)}] = \langle \Psi^{(1)} | \hat{H}^{(1)} | \Psi^{(1)} \rangle \, . \tag{2.9}$$

If we consider that any other density $n^{(2)}(\mathbf{r}) \neq n^{(1)}(\mathbf{r})$ is associated to a many-body wavefunction $\Psi^{(2)} \neq \Psi^{(1)}$, it follows immediately that

$$E^{(2)} = \langle \Psi^{(2)} | \hat{H}^{(1)} | \Psi^{(2)} \rangle > E^{(1)} \, . \tag{2.10}$$

Thus the energy given by the functional (2.8) evaluated for the ground state density $n_0(\mathbf{r})$ is always lower than the values obtained for any other density $n(\mathbf{r})$.

The second theorem of Hohenberg and Kohn states that a variational functional of the ground state density exists, but does not provides us with its explicit expression. In fact all the difficulties of the original many-body problem are moved into the functional

$$F_{HK}[n] \equiv T[n] + E_{int}[n] \,, \tag{2.11}$$

which is not known. Fortunately F_{HK} satisfies an important property: it is *universal*, i.e. it depends only on the density, and not on the external potential that defines the particular problem. The universality of the Hohenberg and Kohn functional is the basis of the Kohn-Sham ansatz, presented in the next Section.

Finally we should mention that both the theorems of Hohenberg and Kohn can be easily generalized to spin-dependent densities and degenerate ground states [41]. Moreover the degeneracy is taken into account from the outset in the alternative formulation of density-functional theory by Levy and Lieb [42, 43].

2.2   Kohn-Sham equations

The density functional theory outlined in the previous Section establishes that the ground state properties of any many-body system described by the Hamiltonian (2.1) can be determined without solving the full Schrödinger equation. Unfortunately our construction has no practical use if we do not find a way to determine the Hohenberg-Kohn functional (2.8) in terms of the density. The *ansatz* of Kohn and Sham [2] consists in replacing the many-body problem by an auxiliary problem of independent particles in an effective potential whose (single-particle) Hamiltonian is

$$\hat{H}_{KS}^\sigma = -\frac{\hbar^2}{2m}\nabla^2 + V_{KS}^\sigma(\mathbf{r}). \tag{2.12}$$

Let's suppose then that we can build such a system in a way that its ground state density coincides with the ground state density of the original system. Under this assumption, naming the eigenvalues of equation (2.12) as ε_i^σ and the corresponding eigenvectors as $\psi_i^\sigma(\mathbf{r})$, the electron density can be written as

$$n(\mathbf{r}) = \sum_\sigma n(\mathbf{r}, \sigma) = \sum_\sigma \sum_{i=1}^{N^\sigma} |\psi_i^\sigma(\mathbf{r})|^2, \tag{2.13}$$

where the sum over the quantum number i runs over the states with the lowest energies until the total number of electrons N^σ is reached. The knowledge of the single-particle wavefunctions allows us to express the kinetic energy of the auxiliary system as

$$T_s = -\frac{\hbar^2}{2m}\sum_\sigma \sum_{i=1}^{N^\sigma} \langle \psi_i^\sigma | \nabla^2 | \psi_i^\sigma \rangle = \frac{\hbar^2}{2m}\sum_\sigma \sum_{i=1}^{N^\sigma} |\nabla \psi_i^\sigma|^2 \,. \tag{2.14}$$

In the following we will associate to T_s the functional dependence from $n(\mathbf{r})$. While in fact this dependence is not explicit, it is related to the ψ_i^σ. Another important quantity in the Kohn-Sham construction is the classical Coulomb energy of an electron density interacting with itself, i.e. the Hartree energy

$$E_H[n] = \frac{1}{2} \int d\mathbf{r} d\mathbf{r}' \frac{n(\mathbf{r})n(\mathbf{r}')}{|\mathbf{r} - \mathbf{r}'|}. \tag{2.15}$$

Then the kinetic energy and the Hartree energy of the independent particle system are related to the original system by rewriting the Hohenberg-Kohn functional (2.8) as

$$E_{KS}[n] = T_s[n] + \int d\mathbf{r}\, V_{ext}(\mathbf{r})n(\mathbf{r}) + E_H[n] + E_{xc}[n], \tag{2.16}$$

where the unknown exchange-correlation energy contains all the differences between the actual functional and the exact one:

$$E_{xc}[n] \equiv (T[n] - T_s[n]) + (E_{int}[n] - E_H[n]). \tag{2.17}$$

The expression (2.16) is exact in the sense that it is a simple restatement of the Hohenberg-Kohn formulation and no further approximation has been done, except assuming the existence of a non-interacting fictitious system whose ground state density can reproduce the "real" ground state density. This assumption relies on an interesting representability issue, and while it has been demonstrated for simple systems like one or two electron problems or for system with small deviations from the homogeneous electron gas, no general proof has been produced for "realistic systems" [44]. Moreover we must notice that the problem still retains all the original complexity, and all the difficulties of the solution of the many-body system have simply been moved to the unknown exchange-correlation functional. On the other hand the advantage of the Kohn-Sham formulation is that by explicitly separating out the independent particle kinetic energy and the long range Hartree terms, the remaining exchange-correlation energy (2.17) can reasonably be approximated as a local or nearly local functional of the density, as we will see in the next Section.

Before analyzing the general properties of the exchange-correlation functional and the most widely used approximations, we have to make an explicit connection between the real system described by the functional (2.16) and the fictitious system described by the Hamiltonian (2.12). Since T_s and $n(\mathbf{r})$ are directly expressed as a functional of the orbitals $\psi_i(\mathbf{r})$, we can minimize the expression (2.16) with respect to the variation of those wavefunctions

$$\frac{\delta E_{KS}}{\delta \psi_i^\sigma(\mathbf{r})} = \frac{\delta T_s}{\delta \psi_i^\sigma(\mathbf{r})} + \left[\frac{\delta E_{ext}}{\delta n(\mathbf{r}, \sigma)} + \frac{\delta E_H}{\delta n(\mathbf{r}, \sigma)} + \frac{\delta E_{xc}}{\delta n(\mathbf{r}, \sigma)} \right] \frac{\delta n(\mathbf{r}, \sigma)}{\delta \psi_i^\sigma(\mathbf{r})} = 0. \tag{2.18}$$

By imposing the orthonormalization constraint $\langle \psi_i^\sigma | \psi_j^{\sigma'} \rangle = \delta_{i,j}\delta_{\sigma,\sigma'}$ through the use of the Lagrange multipliers ε_i^σ, it is straightforward to obtain the Schrödinger-like

equations

$$(\hat{H}^{\sigma}_{KS} - \varepsilon^{\sigma}_i)\psi^{\sigma}_i(\mathbf{r}) = 0, \tag{2.19}$$

where H_{KS} has the form of equation (2.12). The whole many-body problem is moved to the determination of the Kohn-Sham potential

$$V^{\sigma}_{KS}(\mathbf{r}) = V_{ext}(\mathbf{r}) + \frac{\delta E_H}{\delta n(\mathbf{r}, \sigma)} + \frac{\delta E_{exc}}{\delta n(\mathbf{r}, \sigma)} \tag{2.20}$$

$$= V_{ext}(\mathbf{r}) + V_H(\mathbf{r}) + V^{\sigma}_{xc}(\mathbf{r}), \tag{2.21}$$

in particular to the third term: the unknown exchange-correlation potential $V^{\sigma}_{xc}(\mathbf{r})$.

2.3   Local density approximation

As Kohn and Sham noticed in their original paper [2] many solids can be considered close to the limit of the homogeneous electron gas, where the exchange and correlation effects are local in character. In the local density approximation (LDA) we assume this locality to be valid also in our generic electron system. Because of the universality of the Hohenberg-Kohn functional, it follows that

$$E_{xc}[n] = \int d\mathbf{r}\, n(\mathbf{r})\epsilon^{hom}_{xc}(n(\mathbf{r})), \tag{2.22}$$

where $\epsilon^{hom}_{xc}(n(\mathbf{r}))$ is the exchange-correlation energy of the homogeneous electron gas with density equal to $n(\mathbf{r})$. The only element needed is the function ϵ^{hom}_{xc}. The contribution of the exchange can be obtained as a simple analytical expression. The remaining contribution of the correlations can be either calculated through perturbative many-body techniques [45], or obtained as fitting [11, 46] of numerically exact quantum Monte-Carlo (QMC) simulations [47, 48, 49, 50]. Although this approximation seems rather crude, indeed it can successfully describe various systems, ranging from isolated atoms and molecules to extended solids. It is necessary to stress that the LDA is an "uncontrolled" approximation, in the sense that the validity of the method is established by its ability to reproduce experimental results.

As originally pointed out by Gunnarson and Lundqvist [51], the success of the local density approximation can be explained in terms of an exchange-correlation hole. Given that the electronic interactions are pair interactions, almost all the properties of the physical system can be obtained from the pair correlation function[2] $g(\mathbf{r}, \mathbf{r}')$, corresponding to the joint probability of finding one electron in $\mathbf{r}$ and another electron in $\mathbf{r}'$. It is convenient to extend the discussion to a generic strength of the electron-electron interaction λV_{int}, with the parameter λ varying

---

[2]For simplicity we neglect the spin degrees of freedom.

from zero (non-interaction system) to one (fully interacting system). Then we can redefine the normalized version of the previous correlation function:

$$\rho_{xc}(\mathbf{r}, \mathbf{r}', [n], \lambda) = \frac{g(\mathbf{r}, \mathbf{r}')}{n(\mathbf{r})}, \tag{2.23}$$

where the dependence from λ has been made explicit. ρ_{xc} is the density of the exchange-correlation hole and describes the space in $\mathbf{r}'$ from which an electron is *missing*, once that it is known to be in $\mathbf{r}$. The missing electron is expressed by the sum rule

$$\int d\mathbf{r}' \, \rho_{xc}(\mathbf{r}, \mathbf{r}', [n], \lambda) = -1, \tag{2.24}$$

easily obtainable [51] from the normalization of $n(\mathbf{r})$.

By considering a continuous transition between the non-interacting and the interacting systems (adiabatic connection [52]), it is possible to rewrite the exact exchange-correlation energy (2.17) as

$$E_{xc}[n] = \frac{e^2}{2} \int d\mathbf{r} \int d\mathbf{r}' \frac{n(\mathbf{r})w(\mathbf{r}, \mathbf{r}')}{|\mathbf{r} - \mathbf{r}'|} \tag{2.25}$$

where

$$w(\mathbf{r}, \mathbf{r}') = \int_0^1 d\lambda \, \rho_{xc}(\mathbf{r}, \mathbf{r}', [n], \lambda). \tag{2.26}$$

In other words the exchange-correlation energy can be understood in terms of the potential energy of the exchange-correlation hole averaged over the strength of the interactions.

Moreover, if we define

$$\epsilon_{xc}([n(\mathbf{r})], \mathbf{r}) = \frac{1}{2} \int d\mathbf{r}' \frac{w(\mathbf{r}, \mathbf{r}')}{|\mathbf{r} - \mathbf{r}'|}, \tag{2.27}$$

the exchange-correlation energy (2.25) can be clearly recast in the LDA form (2.22), with the only difference that the dependence on the electron density is now in a form of a functional, instead of a simple function.

We can now individuate two main reasons behind the success of the LDA. First of all it respects the sum rule (2.24), since the LDA exchange-correlation hole is the exact hole for some Hamiltonian (the homogeneous electron gas), even if it is not the correct Hamiltonian! Consequently various constraints are satisfied, leading to an important error cancellation in the different contributions to the energies [44]. In second place, while the shape of the exchange-correlation hole can vary considerably between different systems, the spherical average defined by the integral (2.27) presents a much more uniform character. Then the LDA works reasonably well also for systems apparently very different from the homogeneous electron gas.

All the previous discussion can be easily generalized to spin-polarized systems, leading to the Local Spin-Density Approximation (LSDA). Unfortunately in electronic structure literature the acronym "LSDA" is often (not always) substituted with the basic acronym "LDA", leaving a certain ambiguity. Usually the correct meaning can be extracted from the context: "LDA" must be read "LDA" for non magnetic systems and "LSDA" for magnetic ones. We will also adopt this convention in the rest of the thesis, unless explicitly specified in the text.

2.4 Localized electrons and LDA+U Hamiltonian

In the Introduction we have mentioned that, besides the many successes of the DFT-LDA approach, there exists a large class of materials for which this technique seems to fail. Usually these materials contain non-filled shells of localized electrons. Despite the "feeling" that a functional based on the homogeneous electron gas can be inappropriate in describing a localized density with high gradients, it is instructing to analyze what exactly goes wrong with such states. The Hartree potential felt by a given electron through the equation (2.20), is defined as an electrostatic potential determined uniquely by the electron density. This density is due to all the electrons, including the same electron under consideration: roughly speaking, the electron interacts with itself! This unphysical self-interaction term is present also in a generic many-body method, e.g. Hartree-Fock, but in the latter case it is cancelled by the exchange. Also in the exact exchange-correlation potential there is a contribution that cancels the spurious self-interaction term in the Hartree potential. Unfortunately in an approximated functional as (2.22) this cancellation is only partial and in the case of a localized state becomes the major source of errors. A correction[3] is possible in the self-interaction correction (SIC) method [11], where the exchange-correlation functional is redefined removing the unphysical terms. However, as stressed in the previous paragraph, LDA is an uncontrolled approximation, so the extraction of the wrong contribution is quite cumbersome, and the method results numerically unstable. As a result, the tendency to the localization is strongly overestimated, and so are the magnetic properties. Then, besides the significant contribution to the description and comprehension of transition metal oxides [53], high-T_c superconductors [54] and rare-earth compounds [55], SIC did not manage to become a de facto alternative to the usual LDA approach.

Nowadays the standard computational methods used in the simulation of the strongly correlated systems are the LDA+U scheme and the LDA+DMFT scheme. We prefer to use the word "scheme" instead of "method" since they are based on

---

[3]While it is not mentioned we refer to extended systems. In fact for finite systems the implementation of the correction to the self-interaction Hartree term is much simpler and was introduced already by Hartree himself in 1928.

an heuristic correction to the one-particle LDA Hamiltonian. It is not a trivial task to justify the application of such a correction: in the following we present the historical arguments that lead to its formulation; at the end of the Section we will mention a connection to more rigorous arguments.

At the end of the eighties, just after the discovery of the high T_c superconductivity, much attention was dedicated to the study of simplified model Hamiltonians, among which the already mentioned Hubbard model [6, 7, 8] and Anderson model [16] are the most known. Albeit these models approaches were based on parameters obtained through DFT-LDA, they were remarkably accurate for the simulation of various different systems, as rare-earth compounds [56], $3d$-transition metal Mott insulators [57], impurity systems [58] and high-T_c superconductors [59, 60].

It is clearly a paradoxical situation: on the one hand the DFT-LDA cannot describe the physics of the strongly correlated systems, on the other hand all the needed information is apparently there. Cannot we build a method able to *repair* directly the deficiencies of the LDA, without passing through model Hamiltonians?

For the construction of this method we have to better understand the relation between the LDA and the Hubbard model. Let us refer to the energy scale mentioned in the Introduction, by considering the limit $U \gg W$, i.e. the physical picture of Mott insulators. In this regime a mean-field solution of the Hamiltonian (1.2) gives the correct description of the system [12]. It follows that the main problem of the LDA approximation in treating Mott insulators is not its mean-field nature, but more the absence of an *explicit* Hubbard term for the electron-electron interactions[4]. It is now natural to correct [12] the LDA Hamiltonian with an Hubbard type interaction to be evaluated within the Hartree-Fock method (LDA+U) or within more sophisticated methods (LDA+DMFT).

In practical terms the whole procedure is based on the choice of a set of orbitals whose description is not good enough in the LDA. We call them "correlated orbitals" and indicate them with $|\mathbf{R}, \xi\rangle$, where $\mathbf{R}$ is the vector specifying the Bravais lattice site and the ξ is an index that enumerates the orbitals within the unit cell of the crystal. The choice of $\{|\mathbf{R}, \xi\rangle\}$ is dictated by physical motivations for the problem under consideration and always implies some degree of arbitrariness (see the discussion below). Usually the correlated orbitals are derived from d or f atomic states and the index ξ stands for the atomic quantum numbers l, m, σ. Natural choices can be linear muffin-tin orbitals [61] or Wannier functions [62, 63]. Apart from the atomic states, hybridized orbitals can also be chosen depending on the problem. For example in the transition metal oxides the crystal field splits the LDA bands in two distinct groups, well separated in energy and suitable to be determined through downfolding of the original problem via the NMTO approach [64].

---

[4]Already in the Introduction we had mentioned that this regime could be explored within one-particle approaches.

After having decided the set $\{|\mathbf{R}, \xi\rangle\}$, the Hubbard interaction term is added to the DFT-LDA Hamiltonian [12, 13]:

$$\hat{H} = \hat{H}_{LDA} + \frac{1}{2} \sum_{\mathbf{R}} \sum_{\xi_1, \xi_2, \xi_3, \xi_4} U_{\xi_1, \xi_2, \xi_3, \xi_4} \hat{c}^\dagger_{\mathbf{R}, \xi_1} \hat{c}^\dagger_{\mathbf{R}, \xi_2} \hat{c}_{\mathbf{R}, \xi_4} \hat{c}_{\mathbf{R}, \xi_3}. \qquad (2.28)$$

This is the so-called LDA+U Hamiltonian, and to understand its meaning, we need to specify what is H_{LDA} and how to obtain $U_{\xi_1, \xi_2, \xi_3, \xi_4}$. From Sections 2.2 and 2.3, we can write that

$$\hat{H}_{LDA} = \sum_{i=1}^{N} \hat{H}^{\sigma_i}_{KS}(\mathbf{r}_i), \qquad (2.29)$$

where the exchange-correlation potential is supposed to come from equation (2.22). It is useful to rewrite the band-structure problem with respect to a basis set of one-particle wavefunctions $|\mathbf{R}, \chi\rangle$ centered at the sites $\mathbf{R}$ and enumerated by a generic quantum number χ, including also the spin σ. This is what happens, for example, in the tight-binding method or the LMTO method of our implementation. Notice that we can consider the correlated basis set $\{|\mathbf{R}, \xi\rangle\}$ and the LDA basis set $\{|\mathbf{R}, \chi\rangle\}$ as independent, and that the latter one is much bigger, given that it contains all the orbitals of the problem, and not only a subset[5]. Passing to the formalism of the second quantization, the expansion into the given basis brings

$$\hat{H}_{LDA} = \sum_{\mathbf{R}_1, \chi_1} \sum_{\mathbf{R}_2, \chi_2} t_{\mathbf{R}_1 \chi_1, \mathbf{R}_2 \chi_2} \hat{c}^\dagger_{\mathbf{R}_1, \chi_1} \hat{c}_{\mathbf{R}_2, \chi_2}, \qquad (2.30)$$

where the "hopping" matrix elements are defined as

$$t_{\mathbf{R}_1 \chi_1, \mathbf{R}_2 \chi_2} = \int d\mathbf{r} \, \langle \mathbf{R}_1, \chi_1 | \mathbf{r} \rangle \, H^{\sigma_{\chi_2}}_{KS}(\mathbf{r}) \, \langle \mathbf{r} | \mathbf{R}_2, \chi_2 \rangle. \qquad (2.31)$$

Now we can see that the Hamiltonian (2.28) represent an effective Hubbard model with the hopping determined by the LDA problem and the Coulomb repulsions specified from the outset. It is clear that in this context the meaning of the matrix elements $U_{\xi_1, \xi_2, \xi_3, \xi_4}$ is not obvious. We could be tempted to think them as matrix elements of the bare Coulomb repulsion, but this idea would not have any justification. Instead we can identify the added correction as an effective interaction that renormalizes the low energy excitations (to describe broader energy scales the U term should be, in general, energy dependent [65]). This picture is intimately related to the idea of the Wilson's renormalization group method [66] and is based on the removal of the unimportant degrees of freedom, as the non localized valence electrons. Unfortunately the removed electrons participate in the screening of the interactions between the correlated electrons (see Appendix B for more details), so that it becomes very complicated to calculate $U_{\xi_1, \xi_2, \xi_3, \xi_4}$

---

[5]Ideally $\{|\mathbf{R}, \chi\rangle\}$ should be complete, but this is not possible in numerical simulations.

with a good precision. In principle we can obtain these matrix elements through two methods: constrained density functional theory [67, 68], which is outlined in Appendix B, and constrained Random Phase Approximation (RPA) [65], which is the extraction of static values from the dynamical polarization of the GW method. Nevertheless it is a common practice to evaluate the strength of the screened effective Coulomb repulsions using semi-empirical procedures [69, 27]. This may seem to be inadequate, since the strength of the effective Coulomb interaction should depend on the set of correlated orbitals, being strictly connected to a mapping of the original electronic Hamiltonian into the equation (2.28). However, if the orbitals $\{|\mathbf{R}, \xi\rangle\}$ are chosen appropriately, the results are quite stable with respect to this ambiguity, as it was first noticed for the LDA+U method [13].

We will give an explicit expression for $U_{\xi_1,\xi_2,\xi_3,\xi_4}$ in the next Chapter, after having described our choices of the correlated orbitals.

2.5 Dynamical mean-field theory

The dynamical mean-field theory can be obtained in many ways, which differ between each other for the mathematical formalism adopted and the degree of complexity [14, 15]. The most pedagogical derivation [4] starts probably from a comparison with the Weiss molecular field theory for the Ising model.

The Ising model is a lattice of classical spins S_i described by the Hamiltonian

$$H = -J \sum_{(i,j)} S_i S_j - h \sum_i S_i, \tag{2.32}$$

where h is the energy of single spin in an external (magnetic) field and J is the ferromagnetic energy due to a spin-spin interaction. To keep the model realistic the first sum is limited to indices that run for pairs of nearest neighbors. The presence of the interaction term correlates the spin between each other, which makes the system hard to solve directly. However, if we focus on one physical quantity, we can try to reduce it to a simpler equivalent system that we are able to solve. Let us focus on the magnetization at a site i

$$m_i \equiv \langle S_i \rangle, \tag{2.33}$$

that is the thermal average of a spin at a single site. Our equivalent system is a lattice of non-interacting spins moving in an effective site-dependent field h_i^{EFF} and the corresponding Hamiltonian is

$$H_{EFF} = -\sum_i h_i^{EFF} S_i. \tag{2.34}$$

The effective field should be chosen to reproduce the same magnetization m_i of the original lattice. Calculating the sum over all the possible configurations for

(2.34), we can write down an explicit expression for the effective field:

$$\beta h_i^{EFF} = \tanh^{-1} m_i, \qquad (2.35)$$

where $\beta = 1/K_B T$. Up to now we have not made any approximation, but we still have not obtained a relation with the original system. In the Weiss mean-field theory the effective field is approximated by the thermal average of the local field seen by a spin at a given site:

$$h_i^{EFF} \simeq h + J \sum_j \langle S_j \rangle = h + Jzm_i. \qquad (2.36)$$

In the last step we have contextualized our discussion to a translationally invariant system with z nearest neighbors for every site. The equations (2.35) and (2.36) can be solved analytically, leading to the approximated magnetization. We have to stress that the procedure of the *mapping* into an equivalent non-interacting system is exact with respect to the chosen observable: the approximation is made when establishing a relation between the Weiss field and the neighboring sites. Furthermore the approximation becomes exact in the limit of $z \to \infty$. This result is quite intuitive: the neighbors of a given site can be globally treated as bath when their number becomes large.

All these ideas can be easily extended to the Hubbard model. Being a fully-interacting quantum many-body system, the mapping procedure is not as obvious as above, but can be established on rigorous basis. For simplicity we consider the one-band model (1.2), but in the next Chapter all the equations will be referred to the LDA+U Hamiltonian (2.28). Instead of the magnetization, we focus on the local Green's function at a single site:

$$G_{\mathbf{R},\mathbf{R}'}^\sigma (\tau - \tau') \equiv -\langle \mathcal{T} \hat{c}_{\mathbf{R},\sigma}(\tau) \hat{c}_{\mathbf{R}',\sigma}^\dagger(\tau') \rangle. \qquad (2.37)$$

Here τ and τ' are imaginary times in the Matsubara's formalism for the perturbation theory at finite temperature and $\mathcal{T}$ is the time-ordering super-operator[6].

As before, we would like to chose the reference system as a single site embedded in an effective field. Since the Green's function (2.37) is time-dependent, the new field must also evolve in time, i.e. must be dynamical. The simplest field we can imagine is a *bath* of non-interacting electrons. The single site, the bath and their coupling can be described by the following Hamiltonian:

$$\hat{H}_{EFF} = \hat{H}_{atom} + \hat{H}_{bath} + \hat{H}_{coupling}. \qquad (2.38)$$

The first term

$$\hat{H}_{atom} = U \hat{c}_\uparrow^\dagger \hat{c}_\uparrow \hat{c}_\downarrow^\dagger \hat{c}_\downarrow \qquad (2.39)$$

---

[6]An overview of the basic definitions and the mathematical details of the Green's function formalism is presented in Appendix A
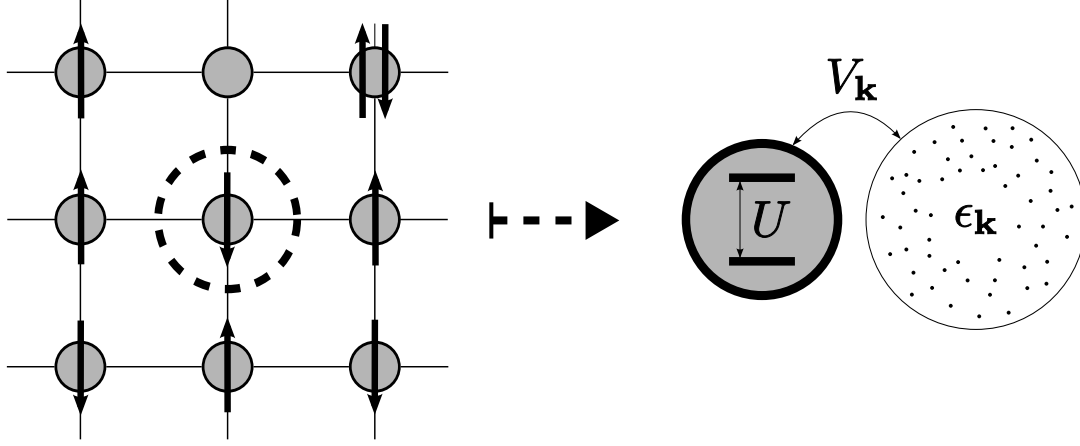
Figure 2.2: In DMFT the lattice problem is mapped into a model of a single atom embedded in an electronic bath. The latter one is fully specified by the bath Green's function $\mathcal{G}_0$ and must be determined self-consistently to preserve the value of the local Green's function of the mapped site.

is the Coulomb repulsion of two electrons at the atomic site, and c and $c^\dagger$ are the corresponding spin-dependent annihilation and creation operators. Notice that this term comes directly from the initial equation (1.2). To assure a formal distinction between the operators of the original model and the lattice model we have omitted the index $\mathbf{R}$. The second term of equation (2.38) is

$$\hat{H}_{bath} = \sum_{\mathbf{k},\sigma} \epsilon_{\mathbf{k},\sigma} \hat{a}^\dagger_{\mathbf{k},\sigma} \hat{a}_{\mathbf{k},\sigma} \tag{2.40}$$

and represents the fictitious sea of electrons whose quantum numbers are their spin σ and wavevector $\mathbf{k}$. We use $\hat{a}$ and $\hat{a}^\dagger$ for the corresponding annihilation and creation operators, and $\epsilon_{\mathbf{k},\sigma}$ for the dispersion relation. Finally the last term of equation (2.38)

$$\hat{H}_{coupling} = \sum_{\mathbf{k},\sigma} V_{\mathbf{k},\sigma} (\hat{a}^\dagger_{\mathbf{k},\sigma} \hat{c}_\sigma + \hat{c}^\dagger_\sigma \hat{a}_{\mathbf{k},\sigma}), \tag{2.41}$$

describes the exchange of electrons between site and bath at an energy $V_{\mathbf{k},\sigma}$. The system is schematized in Figure 2.2.

The Hamiltonian (2.38) is a well-known problem in many-body physics: it is a single impurity Anderson model [16]. In the last 40 years it has been studied extensively and nowadays can be solved through many methods, depending on the range of the parameters and on the allowed approximations [70]. Some of them are used in this thesis, and will be analyzed in the next Chapters, contextually to their application. By now we are interested in finding the connection of the parameters $\epsilon_{\mathbf{k},\sigma}$ and $V_{\mathbf{k},\sigma}$ with the full solution of the problem, i.e. the analogous

formula to equation (2.35). To this aim we treat the first term of equation (2.38) as a perturbation; then the other two terms determine the unperturbed Green's function of the bath $\mathcal{G}_0$. Passing from the imaginary time τ to the Matsubara frequencies[7] $i\omega_n$, we have

$$\mathcal{G}_0^\sigma(i\omega_n) = \frac{1}{i\omega_n + \mu - \Delta^\sigma(i\omega_n)} \qquad (2.42)$$

where μ is the chemical potential, which sets the correct number of particles, and the quantity

$$\Delta^\sigma(i\omega_n) = \sum_{\mathbf{k}} \frac{|V_{\mathbf{k},\sigma}|^2}{i\omega_n - \epsilon_{\mathbf{k}}} \qquad (2.43)$$

is called hybridization function. In terms of many-body perturbation theory [71, 72] the full Green's function of the Hamiltonian (2.38) can be obtained by means of the Dyson equation

$$G_{imp}^\sigma(i\omega_n) = [\mathcal{G}_0^\sigma(i\omega_n)^{-1} - \Sigma_{imp}^\sigma(i\omega_n)]^{-1}, \qquad (2.44)$$

where Σ_{imp} is the self-energy function and contains all the effects of the interactions. Σ_{imp} depends only on the unperturbed Green's function $\mathcal{G}_0$ and the interaction term equation (2.39). The parameters $\epsilon_{\mathbf{k},\sigma}$ and $V_{\mathbf{k},\sigma}$ enter in the full problem only through $\mathcal{G}_0$, which takes the meaning of the "Weiss" field and which is determined to have the impurity full Green's function (2.44) coincide with the local Green's function (2.37):

$$G_{imp}^\sigma(i\omega_n) = G_{\mathbf{R},\mathbf{R}'}^\sigma(i\omega_n). \qquad (2.45)$$

The fact that the parameters do not appear explicitly in the mapping procedure makes it more rigorous to redefine the problem in terms of an effective action formalism, instead of the Hamiltonian (2.38). Integrating out the bath degrees of freedom, we can write down [14] the effective action for the orbital of the impurity as

$$S = -\int_0^\beta d\tau \int_0^\beta d\tau' \sum_\sigma \hat{c}_\sigma^\dagger(\tau) [\mathcal{G}_0^\sigma(\tau - \tau')]^{-1} \hat{c}_\sigma(\tau') +$$

$$U \int_0^\beta d\tau \hat{c}_\uparrow^\dagger(\tau) \hat{c}_\uparrow(\tau) \hat{c}_\downarrow^\dagger(\tau) \hat{c}_\downarrow(\tau). \quad (2.46)$$

The action S fully determines the dynamics of the local site under consideration: the first term takes into account electrons jumping from the bath on the site at τ and coming back to the bath at τ'; the second term includes the Coulomb repulsion when two electrons with opposite spins are present on the site at the same time.

---

[7]Again see Appendix A for more details.

Now we have the most rigorous expression for the full Green's function of the impurity:

$$G_{imp}^{\sigma}(\tau - \tau') \equiv -\langle \mathcal{T}\hat{c}_{\sigma}(\tau)\hat{c}_{\sigma}^{\dagger}(\tau')\rangle_S. \tag{2.47}$$

Anyway we must stress again that in both the formulations in terms of Dyson's equation or in terms of the effective action, the central point is the preservation relation (2.45).

Up to now the representation of the chosen observable of the original lattice is exact. The approximation is done with the next step: the connection of the two systems. In the DMFT the lattice self-energy is only local and coincides with the self-energy of the impurity model:

$$\Sigma_{\mathbf{R},\mathbf{R}'}^{\sigma}(i\omega_n) = \delta_{\mathbf{R},\mathbf{R}'}\Sigma_{imp}^{\sigma}(i\omega_n). \tag{2.48}$$

In the reciprocal space it means that the self-energy becomes $\mathbf{k}$-independent.

While the approximation (2.48) can appear rather arbitrary, indeed is mathematically very similar to equation (2.36). In fact it becomes exact in the limit of infinite nearest neighboring sites, or equivalently, infinite dimensions, as was proved by Metzner and Vollhardt in a work [73] that is considered the first milestone of the DMFT. One year later, Georges and Kotliar [74] completed the main framework of the theory by proving that in the same limit the Hubbard model can be exactly mapped into the Anderson impurity model. Their proof is based on the fact that the topology of all the irreducible Feynman diagrams becomes the same in the two systems: simply the local contribution of all the diagrams.

The parallelism between the Weiss mean-field theory for the classical Ising model and the quantum Hubbard model is summarized in Table 2.1. In addi-

Table 2.1: The Weiss molecular field theory can be generalized to a generic quantum system, as summarized in this table. The original system, the fictitious reference system, the chosen observable and the approximation are shown for the three Hamiltonians specified in the main text.

Original System	Ising Model	Hubbard Model	Electron Hamiltonian
Mapping System	Spins in an Effective Field	Single Impurity Anderson Model	Electrons in an Effective Potential
Selected Observable	Magnetization m_i	Green's Function $G_{\mathbf{R},\mathbf{R}'}(\tau - \tau')$	Electron Density $n(\mathbf{r})$
Approximation	$h_i^{EFF} \simeq h + zJm_i$	$\Sigma_{\mathbf{R},\mathbf{R}'}^{\sigma} \simeq \delta_{\mathbf{R},\mathbf{R}'}\Sigma_{imp}^{\sigma}$	$E_{xc}[n] \simeq E_{xc}^{LDA}[n]$

tion we show also that the same representation can be constructed [75, 15] for the Kohn-Sham equations. In this case the original system is the many-electron Hamiltonian (1.1), and the mapping system is the non-interacting electron gas (2.12) in the effective potential V_{KS}. The approximation comes with the LDA exchange-correlation functional (2.22). It is clear that a strong mathematical connection exists between these *generalized mean-field* theories. More precisely all the three of them can be seen as generalization of the thermodynamical Legendre transformation [4]. We will come back to this point in Chapter 7, when we will need to specify an explicit total-energy functional for the LDA+DMFT scheme.

Before ending the Chapter we should emphasize that the convergence of the DMFT approximation with respect to the number of neighbors is very fast, and this makes it applicable also for more realistic cases, like a 3-dimensional solid. Moreover there are two other limits for which the DMFT becomes exact:

- in the atomic limit $t = 0$ the sites are decoupled from each other, so that the hybridization function $\Delta(i\omega_n)$ is zero; as a result the self-energy has only on-site components, i.e. it is local

- in the non-interacting limit $U = 0$ the self-energy becomes zero, and then again trivially local.

Chapter 3

Implementation of the DMFT into FP-LMTO

The LDA+DMFT scheme is based on a many-body correction to the LDA Hamiltonian, and requires the definition of a subset of localized orbitals. These functions are in principle independent on the basis set of the bandstructure problem, but the physical quantities must be projected from one representation to the other one. In particular the calculation of the local Green's function requires an inversion of a matrix whose elements are defined on the LDA basis set, and this operation results one of the most expensive parts of the LDA+DMFT cycle. It is clear that band structure methods based on many basis functions, as plane waves, are not really convenient, while methods based on localized orbitals represent a better option. This is why the first applications of the DMFT to real materials were based on tight-binding or LMTO methods. Our implementation is based on FP-LMTO method. The definition of MTO and the concept of linearization are presented in the first Section of this Chapter. After that we focus on the expression of the Bloch sums in the FP-LMTO, and on the construction of the wave functions of the correlated orbitals. Finally we present the LDA+DMFT equations used in our implementation Brianna [76, 77], and the Spin-Polarized T-matrix Fluctuation-Exchange (SPTF) [78] perturbative approach to the effective impurity model.

3.1 Muffin-tin orbitals and linearization

The augmented methods are based on the separation of the physical space into two distinct parts: spheres centered on the atoms and interstitial areas between them, as schematically depicted in Figure 3.1(a). At the beginning this distinction was made to treat with a potential with spherical symmetry inside the spheres and
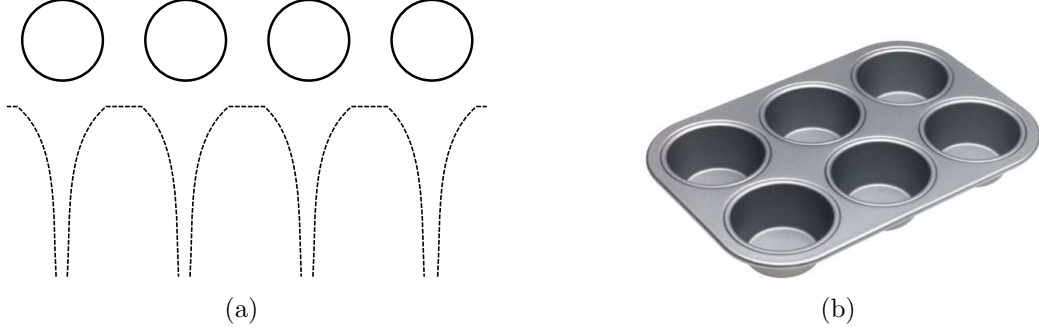
<div align="center">(a)   (b)</div>

Figure 3.1: a) The physical space in the solid is divided into spheres, centered at the atoms, and interstitials between them. In the ASA, the potential is assumed to be spherical inside the spheres and constant in the interstitials. b) In two dimensions the potential used in ASA assumes just the shape of a muffin-tin!

constant outside:

$$V_{KS}(\mathbf{r}) = V_{KS}(r) \qquad\qquad \texttt{MT} \qquad\qquad (3.1)$$

$$V_{KS}(\mathbf{r}) = V_0 \qquad\qquad \texttt{INT} \qquad\qquad (3.2)$$

In two-dimensions the potential takes just the shape of a "muffin-tin", that is the typical mold where muffins or cupcakes are baked, shown in Figure 3.1(b). Therefore the spheres are usually called muffin-tin spheres.

Such approximation, named atomic-sphere approximation (ASA), is particularly useful for close packed structures, where various equations can be reduced to a simpler form, and more compact analytical expressions can be obtained. However for open structures and systems with arbitrary geometry, the description offered by ASA is insufficient, and a full-potential treatment is mandatory: we need to renounce the assumptions (3.1) and (3.2). In any case we can still separate the space in muffin-tins and interstitials for sake of an appropriate and efficient numerical treatment.

The muffin-tin orbitals (MTO) have been introduced by Andersen *et al* [79, 80] as a localized basis continuous in value and derivative at the muffin-tin boundaries. The functions are initially defined as atomic-like, and can be enumerated with the angular quantum numbers[1] l and m. Inside the muffin-tin sphere the basis function ψ_{lm} is composed by an angular part, expressed by the spherical harmonic Y_{lm}, and a radial part ϕ_l, obtained as solution of the radial Schrödinger equation at a given energy ε:

$$\left[\frac{\hbar^2}{2m} \left(\frac{d^2}{dr^2} - \frac{l(l+1)}{r^2} \right) + V_{KS}(r) - \varepsilon \right] r\phi_l(r, \varepsilon) = 0. \qquad (3.3)$$

---

[1]In this Section we neglect the index $\boldsymbol{\tau}$ for different sites (spheres).

In the interstitials the flatness of the potential suggests us to approximate the radial functions with the solutions of the radial Helmholtz equation

$$\left[\left(\frac{d^2}{dr^2} - \frac{l(l+1)}{r^2}\right) - \kappa^2\right] r f_l(r) = 0, \tag{3.4}$$

where we have grouped the energy variables within

$$\kappa^2 \equiv \frac{2m}{\hbar^2}(\varepsilon - V_0). \tag{3.5}$$

These solutions are the spherical Bessel functions $j_l(\kappa r)$ and spherical Neumann functions $n_l(\kappa r)$, where

$$j_l(x) = +(-1)^l x^l \left(\frac{d}{x dx}\right) \frac{\sin x}{x} \tag{3.6}$$

$$n_l(x) = -(-1)^l x^l \left(\frac{d}{x dx}\right) \frac{\cos x}{x}. \tag{3.7}$$

Up to now the functions inside and outside the spheres have been defined with respect to two mutually dependent parameters ε and κ. This construction is completely analogous to the one used in the Korringa Kohn Rostoker (KKR) method [81, 82]. The direct application of the KKR formalism would imply applying the matching condition at the muffin-tin boundaries between the wavefunction ϕ_l and the asymptotic forms

$$\begin{cases} -j_l(\kappa r) + \tan \eta_l(\varepsilon) n_l(\kappa r) & \kappa^2 > 0 \\ -j_l(\kappa r) + \tan \eta_l(\varepsilon) h_l(\kappa r) & \kappa^2 < 0 \end{cases} \tag{3.8}$$

where the phase shifts η_l are related to the scattering due to the potential, and where $h_l = n_l - i j_l$ are spherical Hankel functions of first kind corrected with a factor $-i$. However these orbitals are not suitable as a basis set, since for negative energies the Bessel functions are unbounded. Then they cannot be normalized, apart from the trivial case when κ corresponds to physical eigenvalues.

A solution is obtained removing the Bessel functions inside and outside the muffin-tin, so that we can write down to the following definition of the muffin-tin orbitals:

$$\psi_{lm}^{MTO}(\varepsilon, \kappa, \mathbf{r}) = \mathcal{Y}_{lm}(\hat{\mathbf{r}}) \begin{cases} \phi_l(\varepsilon, r) + \mathcal{J}_l(\kappa, r) \cot\left[\eta_l(\varepsilon)\right] & \texttt{MT} \\ \mathcal{K}_l(\kappa, r) & \texttt{INT} \end{cases}, \tag{3.9}$$

where the original Andersen's notation has been adopted:

$$\mathcal{Y}_{lm}(\hat{\mathbf{r}}) = i^l Y_{lm}(\hat{\mathbf{r}}) \tag{3.10}$$

$$\mathcal{J}_l(\kappa, r) = \kappa^{-l} j_l(\kappa r) \tag{3.11}$$

$$\mathcal{K}_l(\kappa, r) = \kappa^{l+1} \begin{cases} n_l(\kappa r) & \kappa^2 > 0 \\ h_l(\kappa r) & \kappa^2 < 0 \end{cases} \tag{3.12}$$

The muffin-tin orbitals are well defined for all the energies, and can be normalized for all the values of κ. The so-called "head", i.e. the part inside the muffin-tin, is not a radial function any more, since it has been modified by the "tails" of the neighboring atoms. This is the crucial point of the MTO method: the basis functions are constructed by taking into account the structure of the solid. The equations for many atoms are obtained expanding the Neumann or Hankel function extending into another sphere in terms of the (Bessel) functions centered in that sphere. For sake of simplicity we limit to the Hankel functions and we make the notation lighter by grouping the angular numbers l and m into L. Using the corresponding addition theorem [83] we obtain that

$$h_l(\kappa|\mathbf{r} - \mathbf{R}|)Y_L(\widehat{\mathbf{r} - \mathbf{R}}) = \sum_{L'} B_{L'L}^{\mathbf{R'R}}(\kappa) j_{l'}(\kappa|\mathbf{r} - \mathbf{R'}|)Y_{L'}(\widehat{\mathbf{r} - \mathbf{R'}}) \tag{3.13}$$

where we have introduced the structure constants

$$B_{L'L}^{\mathbf{R'R}}(\kappa) = 4\pi \sum_{L''} i^{-l+l'-l''} C_{LL'L''} h_{l''}^*(\kappa|\mathbf{R} - \mathbf{R'}|)Y_{L''}^*(\widehat{\mathbf{R} - \mathbf{R'}}). \tag{3.14}$$

In the previous expression the coefficients

$$C_{LL'L''} \equiv \int d\Omega Y_L(\Omega)Y_{L'}^*(\Omega)Y_{L''}(\Omega) \tag{3.15}$$

are integrals of three spherical harmonics over the solid angle Ω, and they can be reduced to standard Gaunt numbers.

Now we have all the equations needed to formulate the band structure problem. If we required the total wavefunction to be a solution both inside and outside the spheres, i.e. ε and κ to be related as in equation (3.5), we would come back to the non-linear KKR equations. The structure constants and the phase shift would be mutually connected, on the basis of the so-called "tail cancellation" condition. However we prefer to take advantage of the fact that we can treat ε and κ separately. By choosing fixed κ we obtain a major simplification, since the structure constants do not depend on the energy any more, so they can be calculated once and for all. The errors connected to this procedure will be discussed in the next Section.

The main disadvantage of the muffin-tin orbitals is that they still depend on the energy, so that the direct application of the Rayleigh-Ritz variational method would lead to non-linear equations. While simpler than KKR, our method would be much more complicated than the ones based on plane waves or fixed shape orbitals. The solution of this problem is the Andersen's *linearization* technique [84]. The key-idea is to expand the radial wavefunction around a given energy ε_ν:

$$\phi_l(\varepsilon, r) = \phi_l(\varepsilon_\nu, r) + (\varepsilon - \varepsilon_\nu)\dot{\phi}_l(\varepsilon_\nu, r) \tag{3.16}$$

where $\dot{\phi}_l$ denotes the first derivative with respect to ε. The trial wavefunction turns to be correct up to the first order in the energy difference, but the final total energy can be recast into a form that is correct up to the third order [85]. Already the simplest choice of ε_ν, i.e. the middle point of the energy band, gives a very good approximation.

Finally the linear muffin-tin orbitals $\psi_\chi^{LMTO}(\mathbf{R}, \mathbf{r})$ have been obtained: the basis functions are enumerated with the global quantum number χ, which stays for l and m, and for the "tail energy" κ. In addition χ can contain also the site index $\boldsymbol{\tau}$ if more than one atom per cell is present. Our "minimal" basis set is ready for the application of the variational method. In a crystal, it is convenient to construct the so-called "Bloch sums":

$$\psi_\chi^{LMTO}(\mathbf{k}, \mathbf{r}) = \sum_{\mathbf{R}} e^{i\mathbf{k}\cdot\mathbf{R}} \psi_\chi^{LMTO}(\mathbf{R}, \mathbf{r}), \tag{3.17}$$

i.e. linear combinations of the localized orbitals that satisfy the Bloch theorem. Because of the lattice periodicity, the sum over $\mathbf{k}$ is such as

$$\sum_{\mathbf{k}} \equiv \frac{1}{V_{BZ}} \int_{BZ} d\mathbf{k} \qquad\qquad \sum_{\mathbf{k}} 1 = 1, \tag{3.18}$$

where BZ stays for Brillouin Zone. The Bloch sums are then used for expanding the Kohn-Sham eigenfunctions:

$$\psi_{i\mathbf{k}}(\mathbf{r}) = \sum_{\chi} c_{i\chi}(\mathbf{k})\psi_\chi^{LMTO}(\mathbf{k}, \mathbf{r}) \tag{3.19}$$

By evaluating the expectation value of the equation (2.19) with the functions (3.19), we obtain the secular equation

$$\sum_{\chi'} [H_{KS}(\mathbf{k})_{\chi,\chi'} - \varepsilon_i(\mathbf{k})S(\mathbf{k})_{\chi,\chi'}]c_{i\chi'}(\mathbf{k}) = 0, \tag{3.20}$$

where S is the overlap matrix between the Bloch sums, which are not necessarily orthonormal. The system (3.20) has a non trivial solution if the determinant of the term in the square bracket is zero. This is equivalent to finding the coefficients $c_{i\chi}(\mathbf{k})$ that for each $\mathbf{k}$ point determine the basis set for which the Hamiltonian H_{KS} is diagonal.

In the following we will drop the superscript LMTO when referring to the functions (3.17).

3.2   FP-LMTO

After the description of the LMTO basis set in the real space, we can formulate
the explicit expressions used in our computational scheme [37]. Again, we have
to stress that the division of the space in muffin-tin spheres does not carry any
approximation on the geometry of the problem, but it is only a matter of com-
putational convenience. In principle the radii of the muffin-tins are variational
parameters, and the best choice would minimize the total energy. However, in
practice, if the basis set is chosen wisely inside and outside the spheres, the en-
ergy is insensitive to this choice. A good criterion of choice is usually to construct
spheres such that the minimum of the density and the maximum of the potential
along the line between two neighbors fall in the interstitial space.

One exception to this rule is given by the relativistic corrections, since in our
code they are applied only inside the muffin-tin spheres. In this case the choice of
the radii must be taken with care and should follow physical guidelines [86].

Within a given muffin-tin sphere, it is convenient to define a system of local
coordinates with respect to its center $\boldsymbol{\tau}$. Using the rotation operator $\mathcal{D}_{\boldsymbol{\tau}}$ we can
easily express the new coordinates as

$$\mathbf{r}_{\boldsymbol{\tau}} \equiv \mathcal{D}_{\boldsymbol{\tau}}(\mathbf{r} - \boldsymbol{\tau}). \tag{3.21}$$

From the computational point of view, the functions inside the muffin-tins are
expressed in harmonic series:

$$f(\mathbf{r})\Big|_{r_{\boldsymbol{\tau}} < s_{\boldsymbol{\tau}}} = \sum_{h} f_{ht}(r_{\boldsymbol{\tau}}) D_{ht}(\mathcal{D}_{\boldsymbol{\tau}}\hat{\mathbf{r}}) \tag{3.22}$$

where t is the symmetry type inside the unit cell and

$$D_{ht} = \sqrt{\frac{4\pi}{2l_h + 1}} \sum_{m} \alpha_{ht} \mathcal{Y}_{l_h m}. \tag{3.23}$$

The latter coefficients are named spherical harmonic invariants and make clear the
reasons behind the rotation of coordinates at every sphere. In fact, if the local
coordinates are chosen in such a way that it is possible to find a transformation $\mathcal{T}$
for which

$$\mathcal{D}_{\boldsymbol{\tau}'} = \mathcal{D}_{\boldsymbol{\tau}} \mathcal{T}^{-1} \qquad\qquad \texttt{if} \qquad \mathcal{T}\boldsymbol{\tau} = \boldsymbol{\tau}' \tag{3.24}$$

then the spherical harmonic invariants depend only on the global symmetry type,
and not on the given site. Moreover the number of harmonics needed in the
expansion (3.22) is strongly reduced.

In the interstitials the functions are expressed in Fourier series:

$$f(\mathbf{r})\Big|_{r \in \mathcal{I}} = \sum_{\mathcal{S}} f(\mathcal{S}) D_{\mathcal{S}}(\mathbf{r}) \tag{3.25}$$

where

$$D_{\mathcal{S}}(\mathbf{r}) = \sum_{\mathbf{g} \in \mathcal{S}} e^{i\mathbf{g} \cdot \mathbf{r}}. \qquad (3.26)$$

Here $\mathbf{g}$ are vectors of the reciprocal lattice and $\mathcal{S}$ are the corresponding symmetry stars.

Now we can write down the explicit expressions for the Bloch sums (3.17) in in the interstitials, at the muffin-tin boundaries and inside the spheres. In the interstitials we have that

$$\psi_{\chi}(\mathbf{k}, \mathbf{r})\Big|_{\mathbf{r} \in \mathcal{I}} = \sum_{\mathbf{R}} e^{i\mathbf{k} \cdot \mathbf{R}} \mathcal{K}_{l_{\chi}}(\kappa_{\chi}, |\mathbf{r} - \boldsymbol{\tau}_{\chi} - \mathbf{R}|) \mathcal{Y}_{l_{\chi} m_{\chi}}(\mathcal{D}_{\boldsymbol{\tau}_{\chi}}(\mathbf{r} - \boldsymbol{\tau}_{\chi} - \mathbf{R})), \quad (3.27)$$

where usually the function at right hand side is called envelope function. Notice that for given angular quantum numbers, we can define functions for different κ. This is done for compensating the error introduced during the creation of the LMTO, by separating κ from ε. Without the multiple κ, we would have a poor basis in the interstitials, and our description would be reliable only for closed packed structure. Unfortunately there is not a simple scheme to choose a good set of tail energies. The optimum set would lead to the minimum of the energy, but this procedure would be extremely time consuming. It is observed, however, that the set of tails obtained trough minimization for simple systems in representative configurations can be extended to general systems[2].

At the boundaries of the muffin-tin spheres the Bloch sums can be elegantly written as

$$\psi_{\chi}(\mathbf{k}, \mathbf{r})\Big|_{r_{\boldsymbol{\tau}} = s_{\boldsymbol{\tau}}} = \sum_{L} \mathcal{Y}_{L}(\mathcal{D}_{\boldsymbol{\tau}} \hat{\mathbf{r}}_{\boldsymbol{\tau}}) K_{l}(\kappa_{\chi}, s_{\boldsymbol{\tau}}) S_{L, L_{\chi}}(\kappa_{\chi}, \boldsymbol{\tau} - \boldsymbol{\tau}_{\chi}, \mathbf{k}), \qquad (3.28)$$

where we have introduced a two-component row vector

$$K_{l}(\kappa, r) = \begin{bmatrix} \mathcal{K}_{l}(\kappa, r) & \mathcal{J}_{l}(\kappa, r) \end{bmatrix} \qquad (3.29)$$

and a two-component column vector

$$S_{L, L'}(\kappa, \boldsymbol{\tau} - \boldsymbol{\tau}', \mathbf{k}) = \begin{bmatrix} \delta_{\boldsymbol{\tau}, \boldsymbol{\tau}'} \delta_{L, L'} \\ B_{L, L'}(\kappa, \boldsymbol{\tau} - \boldsymbol{\tau}', \mathbf{k}) \end{bmatrix}. \qquad (3.30)$$

The coefficients B are unitarily equivalent to the Fourier transform of the structure constants (3.14). The unitary transformation takes into account the local coordinates described above, and rotates B from left and right.

---

[2]The situation is quite different when a high range of pressures is explored.

Inside the muffin-tin the Bloch sum is constructed as a linear combination of the radial function and its derivative, as for (3.16). In compact form we can introduce the two-component row vector

$$U_{tl}(\varepsilon_\nu, r) \equiv \begin{bmatrix} \phi_{tl}(\varepsilon_\nu, r) & \dot{\phi}_{tl}(\kappa, r) \end{bmatrix}. \tag{3.31}$$

Then the condition of continuous and differentiable matching at the muffin-tin boundaries can be reduced to find the two-by-two matrix Ω such as

$$U_{tl}(\varepsilon_\nu, s)\Omega_{tl}(\varepsilon_\nu, \kappa) = K_l(\kappa, s) \tag{3.32}$$

$$U'_{tl}(\varepsilon_\nu, s)\Omega_{tl}(\varepsilon_\nu, \kappa) = K'_l(\kappa, s) \tag{3.33}$$

We can finally write down the Bloch sums within the muffin-tin spheres:

$$\psi_\chi(\mathbf{k}, \mathbf{r})\Big|_{r_\tau < s_\tau} = \sum_L \mathcal{Y}_L(\mathcal{D}_\tau \hat{\mathbf{r}}_\tau) U_{tl}(\varepsilon_\chi, r)\Omega_{tl}(\varepsilon_\chi, \kappa_\chi) S_{L,L_i}(\kappa_\chi, \boldsymbol{\tau} - \boldsymbol{\tau}_\chi, \mathbf{k}). \tag{3.34}$$

Some comments must be added concerning the linearization energy ε_χ. The basis set should be flexible enough to describe energy levels derived from atomic states that have different principle quantum numbers, but the same angular momentum quantum number. For example for actinides both the $6p$ and $7p$ states have to be included in the problem. This is usually achieved by considering different basis functions, each with their own "panel" of linearization energies. However this creates technical problems when the energies overlap: the set of eigenvectors is not an orthogonal set and the so-called ghost-bands can arise. Consequently in our method we adopt a different strategy: functions corresponding to multiple principle quantum numbers are included within a single fully hybridizing basis set. The latter one is obtained by using ϕ and $\dot{\phi}$ calculated with linearization energies corresponding to different n.

3.3 Choice of the correlated orbitals

After having solved the LDA problem, we focus on the LDA+U Hamiltonian (2.28), and the first step is the choice of the orbitals spanning the correlated subspace. These orbitals must be localized and should form an orthonormal set, since the standard solvers of the impurity model require this property. In our code we implemented two different definitions, both of them atomic-like and derived from d or f states. The first, more traditional, uses the basis functions $\psi_\chi(\mathbf{R}, \mathbf{r})$ of the FP-LMTO method, defined in first two Sections of this Chapter. They offer a straightforward implementation, given that their orthonormality is assured by construction. We call this definition orthogonalized LMTO (ORT) correlated subspace. Unfortunately these functions present three problems. First of all they

are poorly localized, because of the long decaying tails. In second place they do not have pure l, m character, again because of the tails. Finally they can be defined only with one tail energy κ. While we can still use multiple κ for the other electrons involved in the problem, e.g. sp states, the accuracy of this procedure depends on the system at study: if the state is not very dispersive, as it should be for localized orbitals, then the involved errors become small.

Our second choice is somewhat opposite, since it deals with extremely localized correlated orbitals. We name this option as the muffin-tin only (MT) correlated subspace. The chosen definition is

$$\psi_\xi(\mathbf{R}, \mathbf{r}) = \begin{cases} \phi_l(|\mathbf{r} - \mathbf{R} - \boldsymbol{\tau}_\xi|) Y_{lm}(\widehat{\mathbf{r} - \mathbf{R} - \boldsymbol{\tau}_\xi}) & \texttt{MT} \\ 0 & \texttt{INT} \end{cases}, \tag{3.35}$$

Inside the muffin-tin we use the pure solution of the radial Schrödinger equation (3.3) without linearization. Still this function is evaluated at an energy ε_ξ, and we choose it as the "center of gravity" of the l-projected density of states of the given atom type.

The correlated orbitals in equation (3.35) are zero outside a given muffin-tin, and are thus ultimately local. Furthermore they have pure angular momentum character, and, at the same time, are orthogonal by definition (since they do not overlap). We can now use a basis set with multiple κ for d and f electrons, which gives better LDA description. Note that the correlated orbitals obviously do not form a complete basis set within the Hilbert space of one-electron wavefunctions (since the interstitial region is not included at all). This is not a problem, given that they are only used to define the Hubbard-U term in the Hamiltonian (2.28). The "hopping" term is still the LDA Hamiltonian defined using the FP-LMTO basis set, which we assume to be sufficiently complete. The drawback of this choice is that a numerical projection is necessary (see next Section), and this can introduce small errors. The difference between the two correlated subsets has been visualized in the Figure 3.2.

The following step is the construction of the matrix $U_{\xi_1, \xi_2, \xi_3, \xi_4}$. We have that

$$U_{\xi_1, \xi_2, \xi_3, \xi_4} = \delta_{\boldsymbol{\tau}_1, \boldsymbol{\tau}_2, \boldsymbol{\tau}_3, \boldsymbol{\tau}_4} \delta_{l_1, l_2, l_3, l_4} U_{m_1\sigma_1, m_2\sigma_2, m_3\sigma_3, m_4\sigma_4} \tag{3.36}$$

i.e. we consider only intra-site interactions at the type $\boldsymbol{\tau}$ for a given shell l. Since our correlated orbitals are atomic-like, we can borrow the expansion of the bare Coulomb interaction in terms of spherical harmonics [44], usually used in Hartree-Fock method. We have that

$$U_{m_1\sigma_1, m_2\sigma_2, m_3\sigma_3, m_4\sigma_4} = \delta_{\sigma_1, \sigma_3} \delta_{\sigma_2, \sigma_4} \sum_{n=0}^{2l} a_n(m_1, m_3, m_2, m_4) F^n, \tag{3.37}$$
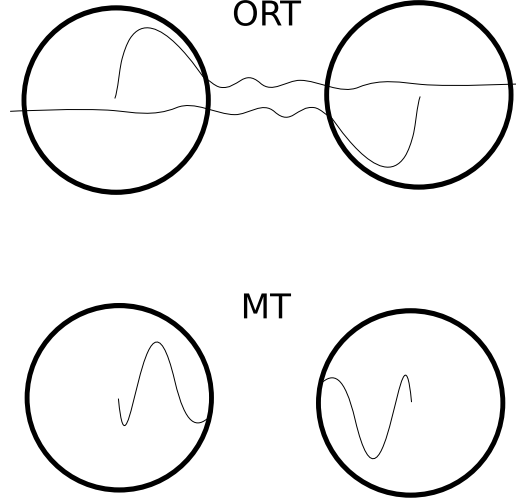
Figure 3.2: Two different choices for the correlated orbitals. In the subset ORT (Top) the FP-LMTO functions are considered: they have long-decaying tails and do not have pure angular character, but they are orthonormal by construction. In the subset MT (Bottom) only the pure wavefunctions of the radial Schrödinger equation are considered: they have pure angular character and they are trivially orthonormal because of the localization.

where the Kronecker symbols express the fact that the interaction is independent on the spin. The coefficients a_n are defined as

$$a_n(m_1, m_3, m_2, m_4) = \frac{4\pi}{2n+1} \sum_{q=-n}^{+n} \langle lm_1|Y_{nq}|lm_3\rangle \langle lm_2|Y_{nq}^*|lm_4\rangle, \qquad (3.38)$$

where the terms $\langle lm_1|Y_{nq}|lm_3\rangle$ and $\langle lm_2|Y_{nq}^*|lm_4\rangle$ are integrals over products of three spherical harmonics, and can be reduced to Gaunt numbers[3]. The definition (3.38) implies that $a_n \neq 0$ only when n is even and smaller than $2l$: that's why the sum in equation (3.37) contains only a few terms. The variables F^n are called Slater integrals and they are defined as

$$F^n = \int_0^\infty \int_0^\infty dr dr' r^2 r'^2 |\phi(r)|^2 |\phi(r')|^2 \frac{r_<^n}{r_>^{n+1}}, \qquad (3.39)$$

where $r_<$ and $r_>$ are the lesser and the greater between r and r', and ϕ indicates the atomic radial wavefunction, independent on m. Because of the screening, we cannot calculate these integrals directly, but we have to find a way to connect them to the average direct and exchange integrals of the screened interaction U and J.

---

[3]In fact the general form of equation (3.37) for $l_1 \neq l_2 \neq l_3 \neq l_4$ is usually expressed directly in terms of Gaunt numbers [44]. Furthermore consider that for such a case the F^n would depend on the orbital indices.

The latter ones can be extracted through sophisticated techniques (see Appendix B) or determined semi-empirically. The connection can be made by means of two useful sum rules [87]. The first one is

$$U = \frac{1}{(2l+1)^2} \sum_{mm'} U_{m,m',m,m'} \tag{3.40}$$

$$= F^0, \tag{3.41}$$

and implies that we can identify F^0 with the Hubbard U. The second sum rule is

$$U - J = \frac{1}{2l(2l+1)} \sum_{m \neq m'} (U_{m,m',m,m'} - U_{m,m',m',m}) \tag{3.42}$$

$$= F^0 - \frac{1}{2l}(C_{lk}^{000})^2 F^k, \tag{3.43}$$

where C_{lk}^{000} is a Clebsh-Gordon coefficient. For d and f correlated electrons, we have that

$$J = \frac{1}{14}(F^2 + F^4) \qquad\qquad d \tag{3.44}$$

$$J = \frac{1}{6435}(286F^2 + 195F^4 + 250F^6) \qquad\qquad f. \tag{3.45}$$

Moreover we can use the well-known fact that the ratios between the Slater integrals F^2, F^4 and F^6 are reasonably constant for a given electronic shell [88, 13], which has been verified both experimentally and computationally (Hartree-Fock). Following the previous references, we assume that for $3d$ electrons

$$\frac{F^2}{F^4} = 0.625. \tag{3.46}$$

Then we have reduced the determination of the full 4-index U-matrix to two values of U and J.

A slightly different approach can be also used: by considering that F^2, F^4 and F^6 are not heavily screened, we can evaluate them directly through (3.39). In this case the full 4-index U-matrix requires only the direct Hubbard U to be set by hand. This has been our choice for the mixed-valence systems presented in Chapter 9.

3.4 LDA+DMFT equations

The DMFT formalism of Section 2.5 was obtained for the one-orbital Hubbard model, but the generalization to the multi indices LDA+U Hamiltonian (2.28) is straightforward. Instead of using functions in the positions representation, we

prefer to adopt the Dirac formalism for vectors in an abstract Hilbert space. Then we indicate the LDA basis set with $\{|\mathbf{k}, \chi\rangle\}$ and the set of the correlated orbitals with $\{|\mathbf{R}, \xi\rangle\}$, like in Section 2.4. The relation with the functions defined in the previous Sections is straightforward:

$$\psi_\chi(\mathbf{k}, \mathbf{r}) = \langle \mathbf{r}|\mathbf{k}, \chi\rangle \qquad\qquad \psi_\xi(\mathbf{R}, \mathbf{r}) = \langle \mathbf{r}|\mathbf{R}, \xi\rangle . \qquad (3.47)$$

We have assumed the correlated subset $\{|\mathbf{R}, \xi\rangle\}$ to be orthonormal, but the LDA functions $\{|\mathbf{k}, \chi\rangle\}$ are in general neither orthogonal nor normalized. As a result for every $\mathbf{k}$ point, the algebra involves an overlap matrix

$$S(\mathbf{k})_{\chi_1, \chi_2} = \langle \mathbf{k}, \chi_1|\mathbf{k}, \chi_2\rangle \qquad (3.48)$$

and a conjugate basis set $\{|\mathbf{k}, \tilde{\chi}\rangle\}$. The latter one is defined by the relations

$$\langle \mathbf{k}, \tilde{\chi}_1|\mathbf{k}, \chi_2\rangle = \langle \mathbf{k}, \chi_1|\mathbf{k}, \tilde{\chi}_2\rangle = \delta_{\chi_1, \chi_2} \qquad (3.49)$$

$$\sum_\chi |\mathbf{k}, \tilde{\chi}\rangle \langle \mathbf{k}, \chi| = \hat{1} \qquad (3.50)$$

or explicitly as

$$|\mathbf{k}, \tilde{\chi}_1\rangle = \sum_{\chi_2} \left[S(\mathbf{k})^{-1} \right]_{\chi_2, \chi_1} |\mathbf{k}, \chi_2\rangle \qquad (3.51)$$

$$\langle \mathbf{k}, \tilde{\chi}_1| = \sum_{\chi_2} \left[S(\mathbf{k})^{-1} \right]_{\chi_1, \chi_2} \langle \mathbf{k}, \chi_2|. \qquad (3.52)$$

If, and only if, the basis set $\{|\mathbf{k}, \chi\rangle\}$ is orthogonal and normalized, then $\{|\mathbf{k}, \tilde{\chi}\rangle\}$ coincides with $\{|\mathbf{k}, \chi\rangle\}$.

The matrix elements of an operator are indicated as

$$A(\mathbf{k})_{\chi_1, \chi_2} = \langle \mathbf{k}, \chi_1|\hat{A}|\mathbf{k}, \chi_2\rangle , \qquad (3.53)$$

and for every $\mathbf{k}$ we obtain the following spectral representation:

$$\hat{A}(\mathbf{k}) = \sum_{\chi_1, \chi_2} |\mathbf{k}, \tilde{\chi}_1\rangle A(\mathbf{k})_{\chi_1, \chi_2} \langle \mathbf{k}, \tilde{\chi}_2| . \qquad (3.54)$$

This convention leads to the following rules of operator-to-matrix correspondence

$$\hat{A} \to A \qquad\qquad\qquad \text{operator} \qquad (3.55)$$
$$\hat{1} \to S \qquad\qquad\qquad \text{unity operator} \qquad (3.56)$$
$$\hat{A}\hat{B} \to A S^{-1} B \qquad\qquad \text{product of two operators} \qquad (3.57)$$
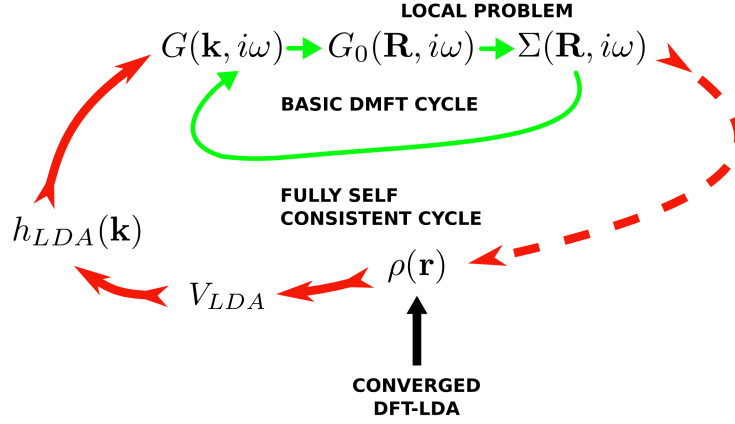$$\hat{A}^{-1} \to S A^{-1} S \qquad\qquad \text{inverse of an operator} \qquad (3.58)$$

Figure 3.3: Schematic representation of the iterative procedure to follow in the LDA+DMFT scheme. As a first step the DFT-LDA problem is solved and a ground state electron density $\rho(\mathbf{r})$ is obtained. From $\rho(\mathbf{r})$ we can extract the matrix elements of the single-particle LDA Hamiltonian, and then build the one-electron Green's function $G(\mathbf{k}, i\omega_n)$ at the Matsubara frequencies $i\omega_n$. Now the basic DMFT cycle starts: the Green's function $G(\mathbf{k}, i\omega_n)$ is projected onto the correlated orbitals, defining the bath Green's function $\mathcal{G}_0^{-1}(\mathbf{R}, i\omega_n)$ of the effective impurity model by means of equation (3.66). The solution of the local problem through one of the available "solvers" leads to a self-energy function $\Sigma_{\mathbf{R}}(i\omega_n)$. After a back projection to the LDA basis set, a new one electron Green's function $G(\mathbf{k}, i\omega_n)$ and a new chemical potential μ are calculated. The procedure is repeated iteratively until convergence in the self-energy and the chemical potential. Once the convergence of the basic DMFT cycle has been reached, a new electron density $\rho(\mathbf{r})$ can be calculated from $G(\mathbf{k}, i\omega_n)$. This is the fully self-consistent cycle and should be continued until convergence in $\rho(\mathbf{r})$.

We can now write down the equations of the LDA+DMFT scheme for a generic basis set. As guideline, we have schematized the LDA+DMFT cycle in Figure 3.3. The starting point of the LDA+DMFT problem is the evaluation of the one-electron Green's function (see Appendix A):

$$\hat{G}(i\omega_n) = [(i\omega_n + \mu)\hat{\mathbf{1}} - \hat{H}_{KS} - \hat{\Sigma}(i\omega_n)]^{-1}. \tag{3.59}$$

Since from the FP-LMTO we have access to the matrix elements of the Kohn-Sham Hamiltonian (2.29), we can conveniently write down

$$G(\mathbf{k}, i\omega_n)_{\chi_1,\chi_2} = [S(\mathbf{k})(i\omega_n - \mu) - H_{KS}(\mathbf{k}) - \Sigma(i\omega_n)]^{-1}_{\chi_1,\chi_2}. \tag{3.60}$$

Let us consider $\Sigma = 0$, corresponding to the first DMFT iteration. Then these matrix elements can be calculated without problems. The next step is the calculation of the local Green's function. By definition

$$\hat{G}(\mathbf{R}, i\omega_n) = \hat{P}_{\mathbf{R}}\hat{G}(i\omega_n)\hat{P}_{\mathbf{R}}, \tag{3.61}$$

where

$$\hat{P}_{\mathbf{R}} = \sum_{\xi} |\mathbf{R}, \xi\rangle \langle \mathbf{R}, \xi| \qquad (3.62)$$

is the projection operator to the correlated subspace belonging to site $\mathbf{R}$. The local Green's function is fully specified by its matrix elements

$$G(\mathbf{R}, i\omega_n)_{\xi_1, \xi_2} \equiv \langle \mathbf{R}, \xi_1 | \hat{G}(\mathbf{R}, i\omega_n) | \mathbf{R}, \xi_2 \rangle = \langle \mathbf{R}, \xi_1 | \hat{G}(i\omega_n) | \mathbf{R}, \xi_2 \rangle. \qquad (3.63)$$

By using equations (3.55–3.58), we obtain our operational expression

$$G(\mathbf{R}, i\omega_n)_{\xi_1, \xi_2} = \sum_{\mathbf{k}, \chi_1, \chi_2} \langle \mathbf{R}\xi_1 | \mathbf{k}, \chi_1 \rangle \, G(\mathbf{k}, i\omega_n)_{\chi_1, \chi_2} \, \langle \mathbf{k}, \chi_2 | \mathbf{R}\xi_2 \rangle \qquad (3.64)$$

The set of equations (3.60–3.64) is crucial in all the LDA+DMFT implementations. In case of big systems with many atoms per unit cell, the inversion (3.60) is one of the most time-consuming parts of the code. Now it is clear why LMTO-based programs offer a great advantage compared to other methods: the matrix (3.60) does not become prohibitively big, since the number of basis functions is minimal. Consequently systems with 30 or 40 atoms per unit cell are still accessible on standard super computers, which allows for studies of surfaces, interfaces, or impurities.

The formula (3.64) can lead to severe numerical errors. In fact it is based on the assumption that the spectralization of the identity operator (3.50) holds. However this relation is strictly valid only if our basis set is (sufficiently) complete, otherwise we lose spectral weight with the projection (3.62). This would represent a big problem, since the local Green's functions would not correspond any more to a set of orthonormalized orbitals.

For the ORT correlated set we are helped by the fact that the functions $\{|\mathbf{R}, \xi\rangle\}$ belong to the same space spanned by the functions $\{|\mathbf{k}, \chi\rangle\}$. Then the projection becomes exact also if the LDA set is not complete.

For the MT correlated set, a carefull check is needed to understand how much spectral weight is lost. An important indicator is the overlap matrix for the correlated orbitals

$$\langle \mathbf{R}, \xi_1 | \mathbf{R}, \xi_2 \rangle = \sum_{\mathbf{k}, \chi} \langle \mathbf{R}, \xi_1 | \mathbf{k}, \tilde{\chi} \rangle \langle \mathbf{k}, \chi | \mathbf{R}, \xi_2 \rangle \qquad (3.65)$$

Table 3.1: Real part of the intrasite overlap matrix between the $3d$ correlated orbitals for the MT subset. On the left side is the matrix for non-magnetic bcc Fe with one tail energy κ. On the right side is the matrix for ferromagnetic bcc Fe with two tail energies κ.

$$
\begin{pmatrix}
0.95439 & 0.00000 & 0.00000 & 0.00000 & -0.00504 \\
0.00000 & 0.95901 & 0.00000 & 0.00000 & 0.00000 \\
0.00000 & 0.00000 & 0.94895 & 0.00000 & 0.00000 \\
0.00000 & 0.00000 & 0.00000 & 0.95902 & 0.00000 \\
-0.00504 & 0.00000 & 0.00000 & 0.00000 & 0.95398
\end{pmatrix}
\qquad
\begin{pmatrix}
0.97161 & 0.00000 & 0.00000 & 0.00000 & 0.00009 \\
0.00000 & 0.97152 & 0.00000 & 0.00000 & 0.00000 \\
0.00000 & 0.00000 & 0.97170 & 0.00000 & 0.00000 \\
0.00000 & 0.00000 & 0.00000 & 0.97152 & 0.00000 \\
0.00009 & 0.00000 & 0.00000 & 0.00000 & 0.97161
\end{pmatrix}
$$

which should be as close as possible to the matrix δ_{ξ_1,ξ_2}. The matrix (3.65) is in general complex, but the imaginary part is evaluated correctly due to the hermiticity of the matrices involved in the sum. Typical values for the real part in the case of $3d$ electrons are reported in Table 3.1. We see that the results are quite close to the identity matrix, and moreover better convergence is obtained with a wise choice of the global tail energies of the LDA set. For $4f$ electrons the approximation is still better, and optimal values as the one reported in Table 3.2 can be obtained.

Another important quantity to check is the inter-site overlap matrix between $\mathbf{R}$ and $\mathbf{R}'$. Ideally it should be zero, but in this case both real and imaginary parts involve errors, which represent a spurious overlap due to the incompleteness. Luckily typical errors are or the order of 10^{-4} or less, as we can see in Table 3.3 for anti-ferromagnetic γ-Mn.

Finally the last check can be made *a posteriori* through comparison of the dependence of the results from the correlated subset MT or ORT. We will make this comparison for ferromagnetic bcc Fe in the next Chapter.

Let us go back to the LDA+DMFT cycle of Figure 3.3. Through the inverse Dyson equation, we evaluate the bath Green's function

$$\mathcal{G}_0(\mathbf{R}, i\omega_n)^{-1}_{\xi_1,\xi_2} = G(\mathbf{R}, i\omega_n)^{-1}_{\xi_1,\xi_2} + \Sigma(\mathbf{R}, i\omega_n)_{\xi_1,\xi_2}. \qquad (3.66)$$

At first iteration it coincides with the local Green's function (3.64). Now the impurity problem is fully determined and must be solved. As we pointed out in Section 2.5 there are many available solvers, and the choice is usually made with respect to the problem under investigation. Given that this thesis is mainly focused on transition metals, the most used solver has been the SPTF solver, and will be described in the Section 3.6. Moreover two other solvers have been used: the numerically exact QMC solver and the Hubbard I approximation. They will be described in the last two Chapters in correspondence with their applications. Once that the effective impurity problem has been solved and a self-energy $\Sigma(\mathbf{R}, i\omega_n)_{\xi_1,\xi_2}$ has been obtained, we must recalculate the one-electron Green's function. Given that the matrix (3.60) is evaluated on the LDA basis set, we must project back

Table 3.2: Real part of the intrasite overlap matrix between the $4f$ correlated orbitals for the MT subset in the case of TmSe with three tail energies κ.

$$\begin{pmatrix} 0.99841 & 0.00000 & 0.00000 & 0.00000 & -0.00001 & 0.00000 & 0.00000 \\ 0.00000 & 0.99840 & 0.00000 & 0.00000 & 0.00000 & 0.00001 & 0.00000 \\ 0.00000 & 0.00000 & 0.99841 & 0.00000 & 0.00000 & 0.00000 & -0.00001 \\ 0.00000 & 0.00000 & 0.00000 & 0.99840 & 0.00000 & 0.00000 & 0.00000 \\ -0.00001 & 0.00000 & 0.00000 & 0.00000 & 0.99841 & 0.00000 & 0.00000 \\ 0.00000 & 0.00001 & 0.00000 & 0.00000 & 0.00000 & 0.99840 & 0.00000 \\ 0.00000 & 0.00000 & -0.00001 & 0.00000 & 0.00000 & 0.00000 & 0.99841 \end{pmatrix}$$

Table 3.3: Real (left) and imaginary (right) part of the inter-site overlap matrix for two different atoms of the anti-ferromagnetic γ-Mn. Three tail energies κ have been used.

$$
\begin{pmatrix}
0.00014 & 0.00025 & 0.00000 & 0.00034 & -0.00018 \\
0.00025 & 0.00081 & 0.00024 & 0.00000 & -0.00034 \\
0.00000 & 0.00024 & 0.00003 & -0.00024 & 0.00000 \\
0.00034 & 0.00000 & -0.00024 & 0.00081 & -0.00025 \\
-0.00018 & -0.00034 & 0.00000 & -0.00025 & 0.00014
\end{pmatrix}
\qquad
\begin{pmatrix}
0.00000 & 0.00025 & 0.00017 & -0.00034 & 0.00000 \\
-0.00025 & 0.00000 & 0.00024 & -0.00085 & 0.00034 \\
-0.00017 & -0.00024 & 0.00000 & -0.00024 & 0.00017 \\
0.00034 & 0.00085 & 0.00024 & 0.00000 & -0.00025 \\
0.00000 & -0.00034 & -0.00017 & 0.00025 & 0.00000
\end{pmatrix}
$$

the self-energy as

$$
\Sigma(\mathbf{k}, i\omega_n)_{\chi_1,\chi_2} = \sum_{\xi_1,\xi_2} \langle \mathbf{k}, \chi_1 | \xi_1 \rangle \, \Sigma(\mathbf{R}, i\omega_n)_{\xi_1,\xi_2} \, \langle \xi_2 | \mathbf{k}, \chi_2 \rangle . \tag{3.67}
$$

The new self-energy changes the number of particles, which makes it necessary to determine a new chemical potential μ. Using the expression of the occupation numbers in terms of the Green's functions, we have:

$$
N = T \sum_{i\omega_n} \sum_{\mathbf{k}} \sum_{\chi_1,\chi_2} S(\mathbf{k})_{\chi_2,\chi_1} G(\mathbf{k}, i\omega_n)_{\chi_1,\chi_2}, \tag{3.68}
$$

where T is the temperature. The sum over the Matsubara poles should include infinite negative and positive frequencies, but obviously in a computational scheme the number of frequencies can only be finite and then a cut-off value ω_{max} needs to be chosen. Unfortunately, as it is clear from the definition (3.60), the Green's functions decay slowly with the energy and then a reliable determination of the number of particles would require a huge cut-off. There are two ways to reach this cut-off: increasing the number of Matsubara frequencies or increasing the spacing between them, which is proportional to the temperature T. None of them is a good solution. The former would imply too big numerical effort (again because of the inversion), while the latter would lead us too far from the $T = 0$ ground-state. One rudimentary solution comes from the empirical consideration that the contribution of the long decaying tails is about $1/2$: then we can just consider the sums in (3.68) as finite and add this term. This strategy can be refined by assuming a constant error, which has to be evaluated at first iteration when we can compare the calculated N with the exact N coming from the LDA. While the previous procedure looks very hazardous, in practice works extremely well. A more sophisticated method will be presented in Chapter 7, and we will be able to explain better the mathematical reasons behind the success of the $1/2$ factor.

Finally we have obtained a new one-electron Green's function, and the the DMFT cycle (Figure 3.3) can be iterated until the self-energy (or equivalently the bath Green's function) is converged. In all the results presented in this thesis the convergence of the self-energy has to be intended up to a tenth of eV or smaller values.

In addition we must mention that, if the correlations are strong, the differences in the population of the Kohn-Sham orbitals lead to a new electron-density $\rho(\mathbf{r})$. In this "full self-consistent cycle" also the convergence of $\rho(\mathbf{r})$ has to be reached. In the present thesis only the basic DMFT cycle is used.

3.5 Hartree-Fock limit and double counting

It is instructive to present the equations for the simplest possible solver of the Anderson impurity model: the Hartree-Fock approximation. By decoupling the annihilation and creation operators in the two-particle term of (2.28), we can easily obtain[4]:

$$\Sigma_{\xi_1,\xi_2} = \sum_{\xi_3,\xi_4} \Big(U_{\xi_1,\xi_3,\xi_2,\xi_4} - U_{\xi_1,\xi_3,\xi_4,\xi_2} \Big) n_{\xi_3,\xi_4}, \tag{3.69}$$

where n indicates the occupation numbers of the correlated orbitals. The self-energy, then, is real, static and also local. If we look at the one-electron Green's function (3.60), it is straightforward to notice that such a correction can be directly added to the Kohn-Sham potential (2.20) and the whole LDA+DMFT machinery becomes not necessary. This construction is equivalent to the LDA+U scheme discussed in the previous Chapters.

One of the most serious (and mysterious!) problems of the LDA+U approach, and also of the LDA+DMFT scheme, is the double-counting. The LDA+U Hamiltonian (2.28) applies a correction to a problem that should already be comprehensive of all possible interactions. As a result there are contributions due to the additional Hubbard term that have already been included in the LDA. It is necessary to remove them, to avoid to count them twice. In terms of the self-energy, we should make the replacement

$$\Sigma \mapsto \Sigma = \Sigma - \Sigma^{DC}, \tag{3.70}$$

where "DC" stays for double counting. Unfortunately the LDA cannot be rewritten in a diagrammatic form and the LDA+DMFT cannot be expressed as a functional of the electron density only. As a result there is no unique one-to-one mapping between different terms in LDA and in the LDA+DMFT, and therefore it is difficult to find a general double-counting correction.

In LDA+U two choices are usually adopted [89], depending on the physical limit to which the system is closer. For metallic systems we assume that the LDA gives a contribution of the same form of (3.69), but with an uniform occupation of the correlated orbitals. In fact this is quite reasonable, if we consider that no orbital polarization is associated to the homogeneous electron gas. Then we have

---

[4]From now on we remove the redundant lattice index $\mathbf{R}$.

that

$$\Sigma^{AMF}_{\xi_1,\xi_2} = \sum_{\xi_3,\xi_4} \Big(U_{\xi_1,\xi_3,\xi_2,\xi_4} - U_{\xi_1,\xi_3,\xi_4,\xi_2} \Big) n^0_{\xi_3,\xi_4}, \qquad (3.71)$$

where

$$n^0_{\xi_3,\xi_4} = \frac{\delta_{\sigma_3,\sigma_4}}{2l_3+1} \sum_m n_{m\sigma_3,m\sigma_3}. \qquad (3.72)$$

Given that the correction creates an artificial atomic polarization around the uniform occupation, this choice is named as around-mean field (AMF) limit.

On the other hand for insulating systems we have to define a different limit. We consider an isolated atom in contact with a reservoir of electrons, which is the system corresponding to our local impurity. The energy of a N degenerate level with Coulomb and exchange parameters U and J, can be written as [89, 13]:

$$E^{AL} = \frac{1}{2}UN(N-1) - \frac{1}{2}JN^\uparrow(N^\uparrow-1) - \frac{1}{2}JN^\downarrow(N^\downarrow-1), \qquad (3.73)$$

where $N^\uparrow$ and $N^\downarrow$ are the relative occupations for spin up and down. Taking the functional derivative of (3.73), we obtain the double-counting correction

$$\Sigma^{AL}_{\xi_1,\xi_2} = \delta_{\xi_1,\xi_2} \left[U\Big(N-\frac{1}{2}\Big) - J\Big(N_{\sigma_1}-\frac{1}{2}\Big) \right]. \qquad (3.74)$$

This atomic-limit (AL) shifts the LDA levels depending on their average occupations. In the extreme cases of empty states, their energy is moved upward by $(U-J)/2$; conversely fully occupied states are rigidly shifted downward by $(U-J)/2$. In practical terms a gap is opened at the Fermi level, and has the same size of the correct Mott-insulating gap. Further this double counting represents the exact correction to the unphysical shape of the LDA energy versus occupation number curve for an isolated atom [88].

The LDA+U scheme works well for both weakly correlated metals (in AMF) and strongly correlated anti-ferromagnetic Mott insulators (in AL). In addition the two double counting corrections can be combined to construct a double-counting independent approach [90], so to explore also the intermediate regimes. However still the main problem remains: it can be easily seen that the LDA+U is only able to emphasize the already existing inhomogeneities in the LDA. If orbital and spin polarization are absent, the LDA+U correction vanishes, and systems as paramagnetic Mott insulators cannot be described. Of course one could introduce an artificial broken-symmetry to reproduce the correct spectral features, but also in this case the results would be unsatisfying for all the dynamical properties, as spectral weight of the Hubbard bands or presence of quasiparticle Kondo resonances [5].

3.6 Spin-polarized T-matrix fluctuation-exchange solver

At the present time no solver is universally considered as the standard approach to the single-impurity Anderson model in DMFT. Usually the choice of the solver is a compromise between accuracy, generality and numerical efficiency. In general we can classify the solvers in two distinct groups. The first category includes numerically exact solvers based on the quantum Monte-Carlo method [91, 92], as the Hirsch-Fye algorithm [93] or the continuous-time algorithm [94, 95]. These approaches are formally exact for all the values of the ratio U/W, but require huge computational effort, also for a few orbitals. Moreover important technical problems can arise when treating with numerical Green's functions, i.e. difficulties in the implementation of the Fourier transforms or in the analytical continuation. The other group of solvers comprises sums of appropriately chosen Feynman diagrams and controlled expansions around given parameters. These approaches are usually very efficient, but they can be applied only in the range of validity of the used approximations. One prototypical example is the Hartree-Fock method of the previous Section, which results into the extremely simple formula (3.69), and is applicable for very large values of U/W. Other examples are the non-crossing approximation (NCA), one-crossing approximation (OCA), iterative perturbation theory (IPT), all reported in the reviews of Refs. [5] and [15].

In the treatment of the moderately strong correlations of the itinerant magnets, a very successful technique has been the SPTF [27, 78, 96] solver, whose acronymous stays for spin-polarized T-matrix fluctuation-exchange. It is based on the fluctuation-exchange approximation of Bickers and Scalapino [97], which captures all the fluctuations that are included in the RPA of the effective interactions in the particle-particle and particle-hole channels, in addition to all the first and second order diagrams. However the emphasis of SPTF is slightly different. Apart from the generalization to the many-orbital system of the original one-orbital formalism, a two-step calculation of the various contributions is adopted. In our derivation we follow the equations used in the relativistic version of SPTF from Ref. [96].

The first step consists in approximating the effective interaction with the T-matrix ladder diagrams. Being $i\Omega_m$ the bosonic Matsubara frequencies (see Appendix A) and using $*$ for the 4-index matrix products, we have that

$$T(i\Omega_m) = U - U * \chi^{PP}(i\Omega_m) * T(i\Omega_m), \tag{3.75}$$

where χ^{PP} stays for the bare particle-particle susceptibility. The latter one has a simpler expression in the imaginary time domain

$$\chi^{PP}_{\xi_1,\xi_2,\xi_3,\xi_4}(\tau) = G_{\xi_1,\xi_3}(\tau)G_{\xi_2,\xi_4}(\tau), \tag{3.76}$$
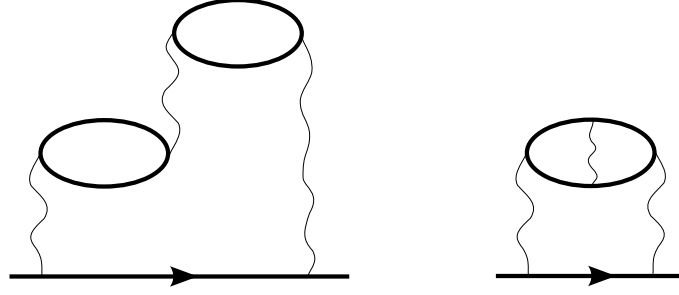
Figure 3.4: Two types of Feynman diagrams that have an important role in describing the magnetic fluctuations. On the left side the screening due to multiple bubbles is sketched. On the right side we can see the ladder interaction inside the bubble itself. These contributions can be reduced to an uniform expression in terms of an anti-symmetrized vertex.

and the transformation to Matsubara frequencies is made through Fourier transform. Now we can write down the Hartree and Fock contributions with the renormalized interaction. Since the T-matrix depends on the frequency, the equations are slightly more complicated than (3.69):

$$\Sigma_{\xi_1,\xi_2}^{TH}(i\omega_n) = \frac{1}{\beta} \sum_{i\Omega_m} \sum_{\xi_3,\xi_4} T_{\xi_1,\xi_3,\xi_2,\xi_4}(i\Omega_m) G_{\xi_4,\xi_3}(i\Omega_m - i\omega_n) \tag{3.77}$$

$$\Sigma_{\xi_1,\xi_2}^{TF}(i\omega_n) = \frac{1}{\beta} \sum_{i\Omega_m} \sum_{\xi_3,\xi_4} T_{\xi_1,\xi_4,\xi_3,\xi_2}(i\Omega_m) G_{\xi_3,\xi_4}(i\Omega_m - i\omega_n). \tag{3.78}$$

Notice that the previous self-energies include exactly all the first and second order contributions.

Once that the particle-particle processes have been described, the second step of SPTF is to analyze the interactions with the particle-hole fluctuations. We want to include all the diagrams that express both the multiple screening of the particle-hole bubble polarization (left side of Figure 3.4) and the particle-hole ladder sum
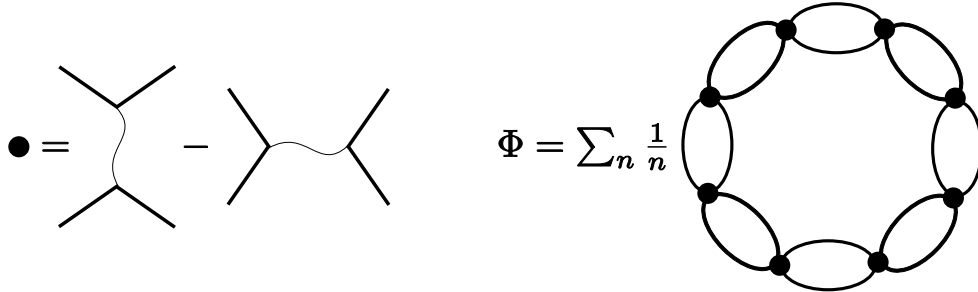

Figure 3.5: Left: the anti-symmetrized vertex of equation (3.79) is represented with a big black dot. Right: Φ-functional that generates all the Feynman diagrams considered in SPTF.

inside the bubble (right side of Figure 3.4). To this aim it is convenient to introduce the anti-symmetrized vertex [96]:

$$U^{AS}_{\xi_1,\xi_2,\xi_3,\xi_4} = T_{\xi_1,\xi_2,\xi_3,\xi_4}(0) - T_{\xi_1,\xi_2,\xi_4,\xi_3}(0), \tag{3.79}$$

where the bare interaction has been replaced with the static value of the T-matrix (3.75). In terms of the anti-symmetrized vertex the diagrammatic contributions can be generated from a simple Φ-functional, as visualized in Figure 3.5.

The functional derivative of Φ with respect to the Green's function gives the self-energy (see Figure 3.6) in the well-know GW form:

$$\Sigma^{PH}_{\xi_1,\xi_2}(\tau) = \sum_{\xi_3,\xi_4} W_{\xi_1,\xi_3,\xi_4,\xi_2}(\tau)G_{\xi_3,\xi_4}(\tau). \tag{3.80}$$

The particle-hole fluctuation potential W is expressed as

$$W(i\Omega) = U^{AS} * \chi^{PH}(i\Omega) * \left[\mathbf{1} - U^{AS} * \chi^{PH}(i\Omega)\right]^{-1} * U^{AS} - W_2(i\Omega), \tag{3.81}$$

where we have introduced the bare particle-hole susceptibility

$$\chi^{PH}_{\xi_1,\xi_2.\xi_3,\xi_4}(\tau) = -G_{\xi_4,\xi_1}(-\tau)G_{\xi_2,\xi_3}(\tau). \tag{3.82}$$

Notice that, in equation (3.81), the last term W_2 removes the second order contribution, which has been already included in (3.77) and (3.78).

The different treatment of the particle-particle and particle-hole channels is motivated by their different role in magnetism. In practical terms the use of the T-matrix effective interaction in the particle-hole channel becomes extremely important for systems far from half-filling, as it has been shown for the Hubbard model [98, 99] through comparison with quantum Monte-Carlo simulations. Furthermore it can be formally justified by the explicit calculation of the electron and magnon Green's functions of a ferromagnet, at least for the spin wave temperature region [100, 101, 102].

Before moving to the next Chapter, we need to spend a few words about our prescription for the double counting. In fact while insulators with a dynamical
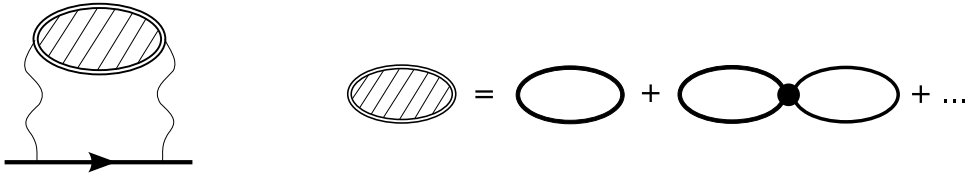

Figure 3.6: On the left side we have the self-energy used for the interactions with the particle-hole fluctuations. The renormalized susceptibility (right side) is expressed in terms of the anti-symmetrized vertex (3.79), sketched as big black dot.

self-energy can still be described through the atomic limit (3.74), for metals we face some conceptual problems, due to the fact that the dynamical contribution to Σ is proportionally more important. The choice of the self-energy (3.71) would imply that the LDA describes the average occupations obtained with the bath Green's function (3.66), where our self-energy is dynamical! This would be unreasonable, and therefore we prefer to adopt the more physical prescription that the LDA describes correctly the orbital average of the *static part* of the self-energy for separate spins, i.e.

$$\Sigma_{\xi_1,\xi_2}^{DC}(i\omega) = \frac{\delta_{\xi_1,\xi_2}}{2l_1+1} \sum_{m_3} \Sigma_{m_3,\sigma_1}(0) \, . \tag{3.83}$$

In the expression the sum reproduces the average over the orbital indices separately for each spin. This choice has shown to be very successful in the description of the moderately correlated systems as transition metals [78, 29], actinides monochalcogenides [96] or metallic plutonium [21]. However the double counting problem is still an open question, and different formulations can be equally successful. For example Chadov *et al* [103] have obtained a very good description of the orbital magnetism of the transition metals by applying the double counting (3.71) to the Hartree-Fock contributions and the double counting (3.83) to the rest of the self-energy.

Chapter 4

Correlation effects in bulk itinerant-electron ferromagnets

The late $3d$ transition metals are materials of great interest. Iron, cobalt, nickel and their compounds are vital for nearly all fields of technology, and the same earth core is believed to be composed predominantly of iron. Considering their importance, it is quite ironic that in the early 21-st century we still lack a complete understanding of these metals.

Before presenting the excitation spectra that have been calculated through the LDA+DMFT scheme, a few words must be spent concerning the definition of excitation energies in an interacting electron system. The ground-state of a non-interacting gas of fermions is determined by occupying all the single-particle states with the lowest energy, compatibly with the Pauli principle. In this way we can form the so-called Fermi sphere, and we can define excited states by adding an electron outside the sphere or removing an electron from the sphere itself. We have then defined the basic idea of "electrons" and "holes". What does it happen when we turn on the interactions? This fundamental problem has been addressed by Landau during the fifties, and lead to the Fermi liquid theory [104]. The original formulation is phenomenological and based on the assumption that the interactions between the particles are short ranged. In fact the theory was first addressed to a different type of Fermi system: a liquid of ^{3}He with hard-core repulsion. At a first sight, it could appear impossible that the long-ranged Coulomb repulsion can fulfill this requirement. However we must consider that the Coulomb interactions experienced by the electrons is effectively short-range due to the screening, as we have seen in the previous Chapters.

The great insight of Landau was to understand that also if the interaction between the bare particles is strong, the elementary excitations at low energy can experience only a reduced number of scattering processes ("restricted phase-space" argument). As a result it is possible to establish a one-to-one correspondence be-

tween the excitations of the Fermi gas and the excitations of the Fermi liquid, which can be called *quasiparticles*. Intuitively the quasiparticles can be visualized as bare particles plus a "cloud" that describes all the quantum fluctuations due to the presence of all the other electrons. The cloud tends to disappear for excitations infinitesimally close to the Fermi energy, since conservation of energy and momentum makes the scattering processes improbable. Microscopic many-body theory using Feynman diagrams provides a complete formal justification of the phenomenological Landau theory [105, 106].

In the LDA+DMFT scheme the applicability of Landau's ideas can be quantitatively investigated. For weakly correlated systems the quasiparticles are well defined in a wide range of energy, and a picture based on the band structure still holds. However Fe, Co and Ni are rather strongly correlated systems. They have partially filled shells of fairly localized $3d$ electrons. These electrons form a narrow d-band, and their behavior shows signs of both atomic-like and free-electron-like behavior [107, 28]. In strongly correlated systems the quasiparticle picture breaks down, except for a close vicinity of the Fermi surface[1]. Quasiparticles become short-lived and therefore they are not well defined, and in many cases noncoherent features such as Hubbard bands and satellites appear in excitation spectra [14, 15]. A treatment based on standard one-particle approaches can still be acceptable, but some deficiencies can be found. For example rather good magnetic moments can be obtained for Fe, Co, and Ni, but the description of the excitations is far to be adequate. Namely, photoemission experiments for these metals [108, 109, 110] demonstrate that calculations based on LDA or GGA (generalized gradient approximation) give too wide majority spin $3d$ band, overestimate the spin splitting and fail to reproduce the 6 eV satellite in nickel, an essentially noncoherent feature. Moreover the presence of a photoemission satellite for bcc iron has been object of scientific discussion [108, 109, 111], while no DFT-LDA simulations or previous LDA+DMFT calculations [27] did reproduce this feature. Here we will investigate all these interesting questions, and we will emphasize that correlation effects based on a full many-body treatment need to be included to describe properly Fe, Co and Ni.

The present Chapter is based on the following publications:

1. A. Grechnev, I. Di Marco, M. I. Katsnelson, A. I. Lichtenstein, J. Wills, and O. Eriksson "Theory of bulk and surface quasiparticle spectra for Fe, Co, and Ni", *Phys. Rev. B* **76**, 035107 (2007)

2. J. Sánchez-Barriga, J. Fink, V. Boni, I. Di Marco, J. Braun, J. Minár, A. Varykhalov, O. Rader, H. A. Dürr, V. Bellini, F. Manghi, H. Ebert, A. I.

---

[1]In case of really strong correlations the quasiparticle pictures breaks down also near the Fermi surface, and the electrons show atomic-like features (see Chapter 9).

Lichtenstein, M. I. Katsnelson, O. Eriksson and W. Eberhardt "Quantitative determination of spin-dependent quasi-particle life-times and electronic correlations in hcp Co", *in preparation for Phys. Rev. Lett.*

4.1 bcc Fe

The first transition metal for which we report the results is Fe. The body-centered-cubic crystal structure is specified by the lattice constant a, which in principle could be determined through the minimization of the total energy within the LDA+DMFT scheme. However, due to the difficulties and the numerical effort that this procedure would imply, we have chosen to use the experimental value of $a = 5.417$ a.u.. Such relaxation of the crystal structure with respect to the lattice constant will be subject of Chapter 7, but it will be applied only to Ni and Mn, and not to Fe.

The band structure problem has been solved including $4s$, $4p$ and $3d$ states among the valence electrons. The $4s$ and $4p$ basis functions have been chosen to have two possible tail energies κ, since they describe dispersive delocalized electrons. For the $3d$ states the number of the tail energies allowed is dependent on the choice of the correlated basis, as explained in the previous Chapter. For the ORT basis set only one κ is permitted, since an exact correspondence between the $3d$ states of the LDA basis set and the ones of the correlated subset must hold. Conversely, for the MT basis set, "double-minimal" wavefunctions with two tail energies have been used. Furthermore a number of 1331 **k**-points have been used in the first Brillouin zone, leading to the convergency of the total energy up to the meV. The next step is the choice of the values of U and J from which we can construct the U-matrix (3.36). Given the bcc Fe has been already studied within the LDA+DMFT scheme, we can use the same values adopted in Refs. [27, 28], i.e. $U = 2.3$ eV and $J = 0.9$ eV. In Section 5.3 we will discuss the choice of the Coulomb parameters for bcc Fe more in detail.

The LDA+DMFT calculations have been made using 1024 Matsubara frequencies for a temperature of 400 K. Due to the high computational effort, the inversion (3.59) is explicitly calculated only for a limited number of frequencies, i.e. 80, distributed on a logarithmic mesh. The passage from the logarithmic mesh to the physical linear mesh is made by means of cubic interpolation.

The result of the LDA+DMFT cycle is the self-energy function Σ evaluated at the Matsubara frequencies $i\omega_n$. However the real physical quantities correspond to operators evaluated at real energies (see Appendix A), then a numerical technique is needed to analytically continue the self-energy in the complex plane. The standard tool used in the strongly correlated community is the Padé approximant method [112]. We should mention that much care must be taken during this operation, since the Padé approximation can introduce severe numerical errors. Due
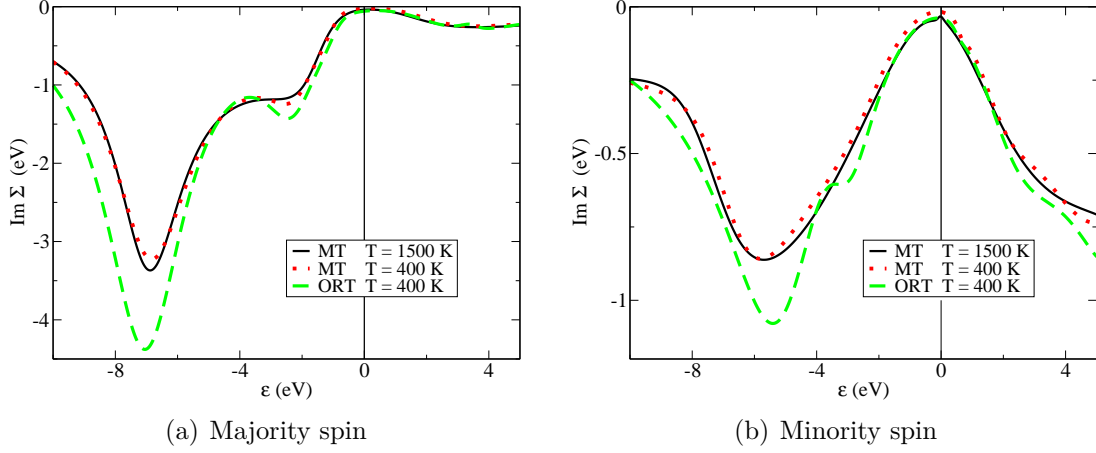
(a) Majority spin

(b) Minority spin

Figure 4.1: Imaginary part of the self-energy $\mathrm{Im}\,\Sigma(\epsilon + i\delta)$ for bcc iron and for the orthogonalized LMTO (ORT) and muffin-tin-only (MT) correlated subspaces. Two different temperatures are considered: $T = 400$ K and $T = 1500$ K. Notice that the axes of the subfigures have different scales, and that the self-energy for minority spin is much smaller than the one for majority spin (see main text).

to the structure of our implementation, the analytical continuation does not enter in the computational cycle, but is needed only for the extraction of the results. This makes it much easier to control the reliability of the procedure. From the practical point of view all the quantities are still evaluated at a finite distance $i\delta$ from the real axis. In the whole Chapter 4 we have adopted $\delta = 60$ meV.

Finally we can start to analyze the correlation effects in bcc Fe. Let us look at the imaginary part of self-energy $\mathrm{Im}\,\Sigma(\epsilon + i\delta)$, reported in Figure 4.1, for both majority and minority spins. In quasiparticle language the matrix elements of the imaginary part of the self-energy define the finite life-times that the excitations acquire because of the electron-electron interaction. Explicitly we have that the life-time is $\tau = \hbar/\Gamma$, where $\Gamma = -\mathrm{Im}\,\Sigma(\epsilon + i\delta)_{\xi,\xi}$. From the last equation, we can see that the life-time is energy-dependent and moreover is different for every orbital of the correlated subset. To give a better visualization, here the self energies are averaged over the orbital indices m, namely[2]

$$\Sigma(z) \equiv \frac{1}{5} \sum_m \Sigma_{mm}(z). \tag{4.1}$$

An important feature that can be seen from Figure 4.1 is that the average self-energy shows a fairly small dependence on the correlated subset. The three curves reported are qualitatively similar, proving that both MT and ORT correlated orbitals (corresponding to well-localized and poorly localized d-states, respectively)

---

[2]The crystal field splitting of Σ is rather small and will not be discussed in detail.
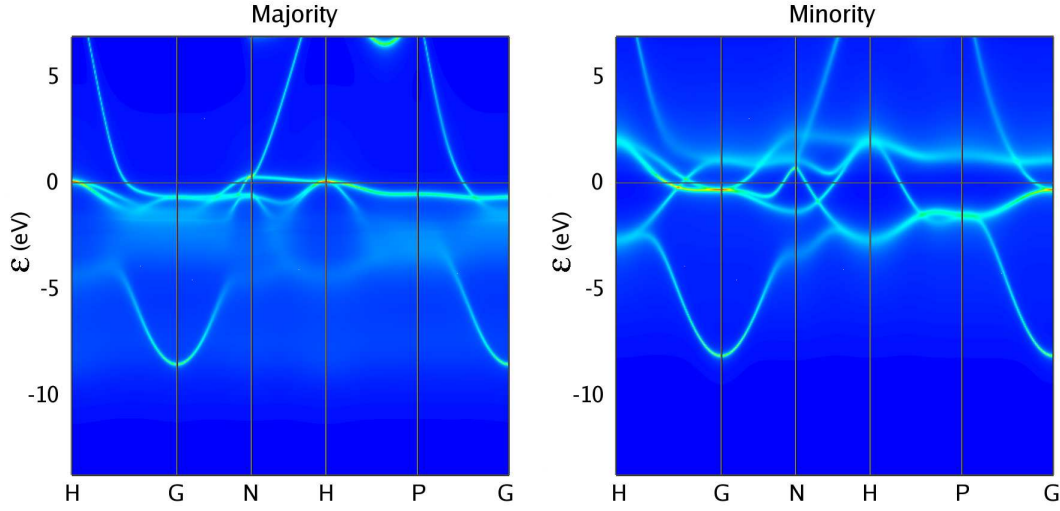
Figure 4.2: Spectral densities of bcc Fe from the LDA+DMFT scheme with MT correlated orbitals at $T = 400$ K.

can be used to adequately describe iron within LDA+DMFT. However, the exact amplitude of the peaks in Σ is sensitive to the choice of the correlated subspace. Also for the other systems that we have studied, the two possible choices of the correlated subset give an adequate description of the correlations and very similar results. With that in mind, and because of the two advantages mentioned in Section 3.3 (better localization and better LDA treatment of d-type electrons), we are going to use the muffin-tin only (MT) correlated orbitals for the rest of this Chapter.

Finally we must spend a few words on the role of the temperature. From Figure 4.1 we can see that the temperature does not influence the self-energy that much, at least not on the energy scale of the order of eV. We must stress that this is due principally to our choice of the double-counting in equation (3.83), which cancels the most of the effects of the exchange. This is in agreement with the fact that the LDA properly describes the magnetic properties of the transition metals.

The effects of the imaginary part of the self-energy can be better observed by means of the spectral density $A(\mathbf{k}, \epsilon + i\delta)$, reported in Figure 4.2. This quantity is a sort of k-resolved density of states or equivalently a band structure plot with the inclusion of the life-times (see Appendix A). In terms of Green's functions the spectral densities are defined for real energies ϵ as

$$A(\mathbf{k}, \epsilon + i\delta) = -\frac{1}{\pi} \sum_{\chi} \langle \mathbf{k}, \tilde{\chi}| \operatorname{Im} \hat{G}(\epsilon + i\delta)|\mathbf{k}, \chi \rangle . \qquad (4.2)$$

As the other quantities accessible from the Green's functions, they have to be evaluated at a finite distance $i\delta$ from the real axis.
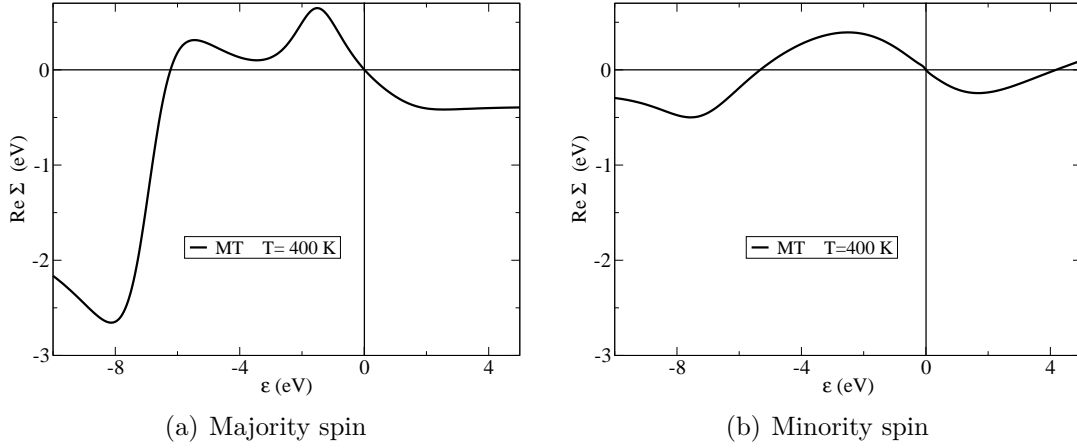
(a) Majority spin   (b) Minority spin

Figure 4.3: Real part of the self-energy $\mathrm{Re}\,\Sigma(\epsilon + i\delta)$ for bcc iron, for both majority and minority spin. Only the results for the MT correlated subspace are presented, and $T = 400$ K.

Consistently with the Landau Fermi liquid theory, the quasiparticles tend to have infinite life-times for energies close to the Fermi level: the self-energy is small, and the spectral density presents well-defined lines of band structure. Conversely for higher energy the scattering processes between the quasiparticles become stronger and stronger. The majority spin $\mathrm{Im}\,\Sigma(\epsilon + i\delta)$ in Figure 4.1(a) has the main peak at $\epsilon \simeq -7$ eV, by reaching the value -3.4 eV. This gives rather strong damping of quasiparticles, as we can observe in Figure 4.2. In this range of energy the lines of the band structure acquire a smearing equal to the parameter Γ defined above. When Γ becomes of the order of the bandwidth W, the definition of band structure becomes meaningless. Notice that the correlation effects are more pronounced for the majority spin electrons, which is common for late transition metals. The reasons are explained in Ref. [113]. Since Fe has fewer electrons (and thus more empty states) in the minority spin band, for any process involving particle-hole pair creation, the pair is more likely to appear in the minority spin band. It means that any scattering process of the majority spin electrons involve creation of minority spin pairs, with effective interaction U. On the other hand, the scattering processes of minority spin electrons also involve creation of minority spin pairs, but the effective interaction for parallel-spin electrons is $U - J < U$. Therefore, the correlation effects are stronger for the majority spin electrons.

Now let us look at $\mathrm{Re}\,\Sigma(\epsilon + i0)$, which is reported for both majority and minority spins in Figure 4.3. From the physical point of view, the real part of the self-energy represents a renormalization energy due to the electron-electron interaction. From the mathematical point of view, it leads to a shift of the poles $H_{KS}(\mathbf{k})$ in the equation (3.60), which defines the Green's function. In the spectral densities this means that the lines that should form the band structure are
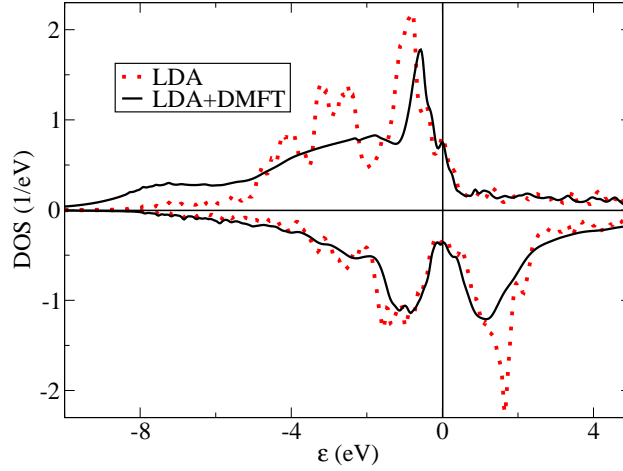
Figure 4.4: Density of states of bcc iron for LDA and LDA+DMFT with the MT correlated orbitals ($T = 400$ K): majority (up) and minority (down) spins.

moved and shrinked, redistributing the spectral weight. These effects are better visible through the density of states, shown in Figure 4.4, and obtainable as trace of the spectral density (4.2) over the electron wave-vector **k**. What we can see is that the LDA+DMFT density of states shows the narrowing of the majority-spin d-band compared to the LDA curve. In Figure 4.3 this corresponds to the positive region of Re Σ for the majority electrons between -6 eV and the Fermi level. Another important feature in the LDA+DMFT density of states is the formation of a non-coherent satellite at $\epsilon \simeq -7$ eV. In terms of the self-energy it corresponds to the sharp negative peak at -8 eV, which "draws" the electrons down in energy. Naturally, the smearing of the quasiparticle bands, given by Im Σ, leads to the smearing of the sharp peaks of the LDA density of states. In addition consider that both the LDA and LDA+DMFT density of states are evaluated at a finite distance $i\delta$ from the real axis, which gives an additional smearing.

The last important issue to discuss is the presence of a possible non-coherent satellite. While the -6 eV photoemission satellite in nickel is common knowledge, the existence of such satellite for bcc iron is still debated. Two independent photoemission experiments [108, 109] reported a weak satellite at about -5 eV (see Figure 4.5), while a third one [114] did not find such feature. A more recent study of Hüfner *et al.* [111] was addressed especially to this problem, and they localized a satellite in Fe at a binding energy of -3.2 eV. On the theoretical side, a LDA+DMFT calculation [27] did not detect any satellite at $U = 2.3$ eV and $J = 0.9$ eV, but only for much larger values of U. The conclusion at that time was, therefore, that there should be no satellite in Fe.

However, in the present thesis we come to a different conclusion. Our self energies and density of states differ from the ones in Ref. [27]. In particular, we
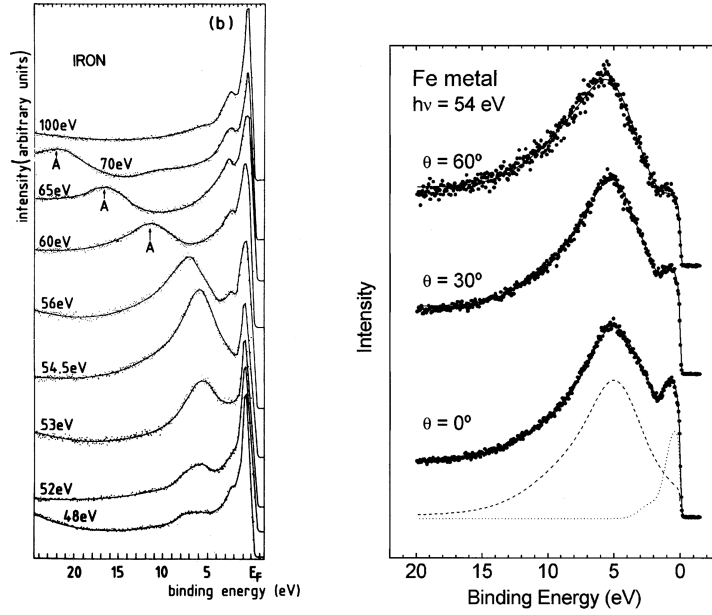
Figure 4.5: Experimental data supporting the existence of a high energy photoemission satellite in the spectrum of bcc Fe. On the left side the photon energy is changed around the resonance energy with the $3p$ transition. Note that for energies higher than the resonance only the Auger peak is visible. Reprinted figure with permission from D. Chandesris, J. Lecante, and Y. Petroff, *Phys. Rev. B* **27**, 2630 (1983). On the right side the photon energy is kept close to the resonance, increasing the height of the satellite peak. This peak does not change with the angle of the incident light, which implies a non-dispersive feature in the Brillouin zone. Reprinted figure with permission from A. Gutierrez and M. F. Lopez, *Phys. Rev. B* **56**, 1111 (1997). [Copyright (2009) by the American Physical Society]

clearly observe a non-coherent satellite at $\epsilon \simeq -7$ eV, which was not observed in the earlier calculation. The reason is that Ref. [27] used a simplified version of the SPTF solver, while in the present paper the full implementation of the SPTF [78] is used. This is confirmed by the comparison of our results with the results obtained with the similar version of the SPTF solver [115].

Apart from the experimental evidence about the satellite in Fe, there are three more reasons why we believe that this full implementation of the SPTF solver is better than the old one. First, in our version we use a complete spin polarized T-matrix, while in the old one there was no spin polarization in the T-matrix. The second reason is the fact that some numerical procedures have been refined, in particular the routines connected to the Fourier transforms have been rewritten to minimize the error due to the slow decaying tails [20]. Finally an important proof of the reliability of this new version of the SPTF solver is represented by the very good agreement of the calculated photoemission spectra of Ni with the experimental data reported in Ref. [29].

We conclude that the presented calculations show the clear existence of the satellite in iron. An important question that is left open is its exact position in the excitation spectrum. The mentioned experimental data differ from each other of about 2 eV, which represents a big indetermination. Unfortunately the theory is not able to give better or more secure answers. In fact the satellite is a pure many-body effect, and its position results to be very sensitive to the value of the effective Hubbard U. We have already discussed how difficult is to determine U in metals with strong screening. In this Section we have presented results for the standard accepted values of U and J. In the Section 5.3 we will discuss the issue of the choice of the Coulomb parameters more in detail and on the basis of photoemission experimental data.

4.2   Co and Ni

The other itinerant ferromagnets with a partially filled 3d-shell are Co and Ni. The ground-state crystal structure of Co is hexagonal close-packed (hcp) with a lattice constant $a = 4.74$ a.u. and a distance between the hexagonal planes $c = 7.69$ a.u.. We have also studied the face centered-cubic (fcc) structure, which is often found in literature. In this case a lattice constant $a = 6.69$ a.u. has been used. For Ni we have adopted the fcc crystal structure with the experimental lattice constant $a = 6.66$ a.u.. All the other computational details concerning the DFT-LDA part of the simulations have been set in the same way as for bcc Fe. As in the previous Section, we have parametrized the U-matrix using semi-empirical values that are generally accepted in literature. For Co we have used $U = 2.3$ eV and $J = 0.9$ eV from previous 3-body scattering calculations [113]. For Ni more data are available, and parameters as $U = 3.0$ eV and $J = 1.0$ eV have already been used with success in previous LDA+DMFT calculations [78, 29].

The LDA+DMFT self-energies for fcc nickel, hcp cobalt and fcc cobalt are presented in Figure 4.6, and the curves for bcc Fe are also shown for comparison. The general structure of the self-energy is similar for all the three metals. The correlation effects for majority spin electrons at energy scale about -7 eV are strongest for Ni and weakest for Fe, at least for the values of U and J used here, which is natural since the bands are narrower for Ni than for the other two elements (only for Ni is the Hubbard U similar in size to the bandwidth W). This is the so-called satellite region and is related with the particle-particle T-matrix renormalization which is largest for the almost filled-band case of Ni. The situation changes for lower excitation energies. The shoulder between -2 eV and -4 eV is most pronounced for Fe and practically disappears for Ni. The reason for this is discussed in Ref. [113]. While the self-energy peaks at about -7 eV are connected to the appearance of the noncoherent satellite, the self-energy features between 0 and -4 eV renormalize the quasiparticle band structure. At this energy scale the correlation effects are
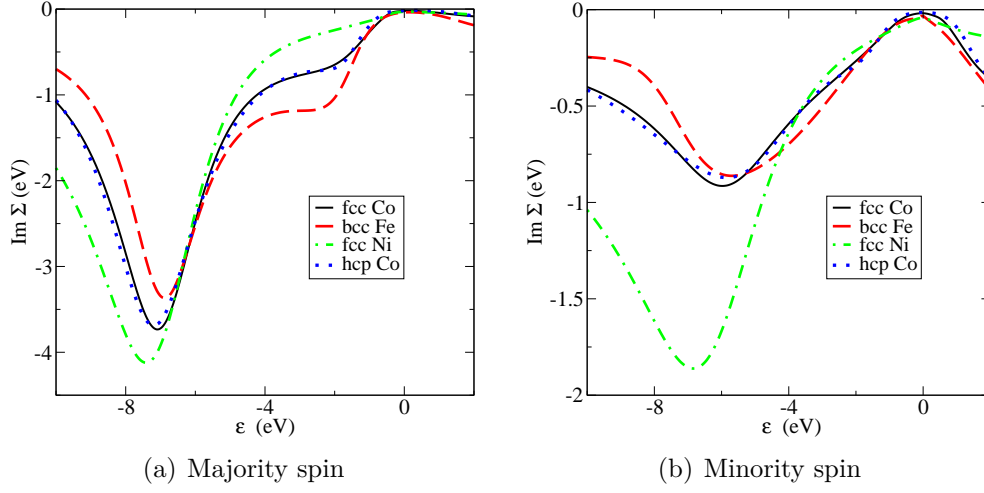
(a) Majority spin (b) Minority spin

Figure 4.6: Imaginary part of the self-energy $\mathrm{Im}\,\Sigma(\epsilon + i\delta)$ for bcc Fe, fcc Ni, fcc Co, and hcp Co. Both majority and minority spins are reported for the MT correlated subspace and at $T = 400$ K. Notice that the scales of the self-energies axes are different.

given by various scattering processes involving creation of electron-hole pairs in the d-band. Of the three elements discussed here Fe is the only one with significant weight of the unoccupied spin up d-band, allowing a creation of electron-hole pairs in this spin channel. Thus the correlation effects caused by electron-hole excitations are strongest among the three metals. Ni, on the other hand, has essentially a filled spin up d-band and thus the weakest correlations of this type. Note that
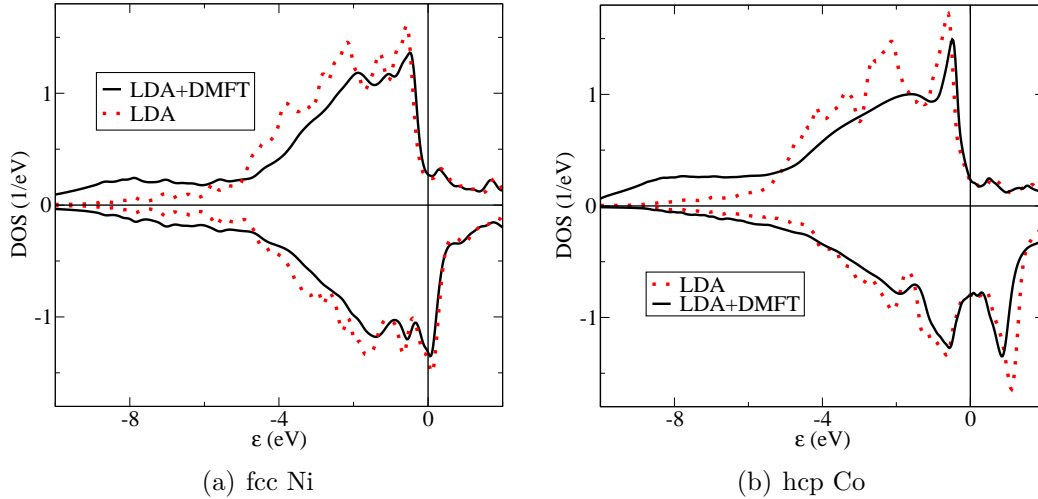

(a) fcc Ni (b) hcp Co

Figure 4.7: Density of states of fcc Ni and hcp Co (LDA vs LDA+DMFT with MT correlated orbitals at $T = 400$ K).
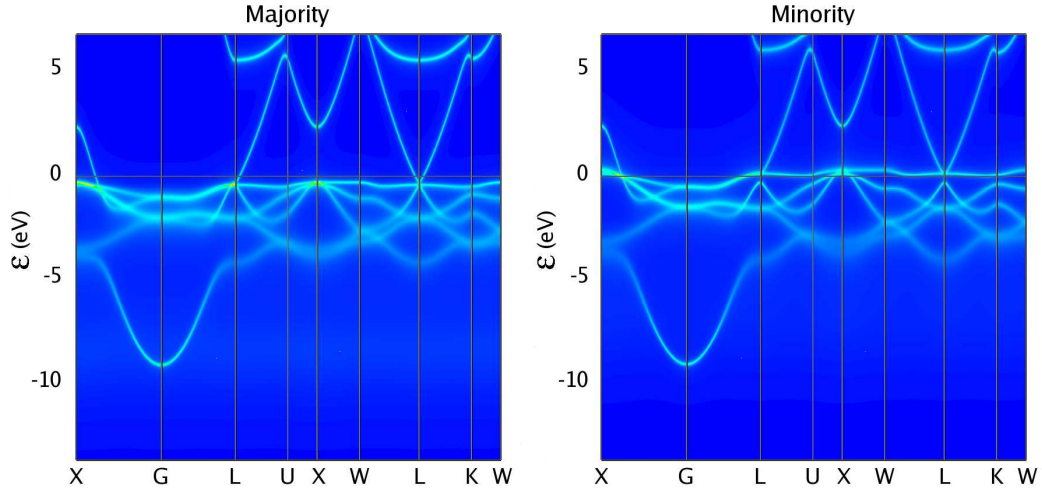
Figure 4.8: Spectral densities of fcc Ni from the LDA+DMFT scheme with MT correlated orbitals at $T = 400$ K.

copper with completely filled d-band basically does not show any correlation effects, while manganese with almost half-filled d-band has the strongest correlation effects in this region [116], as we will see in Chapter 8. The self-energy curves for fcc Co and hcp Co are, as expected, almost identical since these crystal structures differ only in the next nearest neighbor distribution and beyond. The correlation for minority spin electrons - see Figure 4.6(b) - are by far strongest in Ni, which
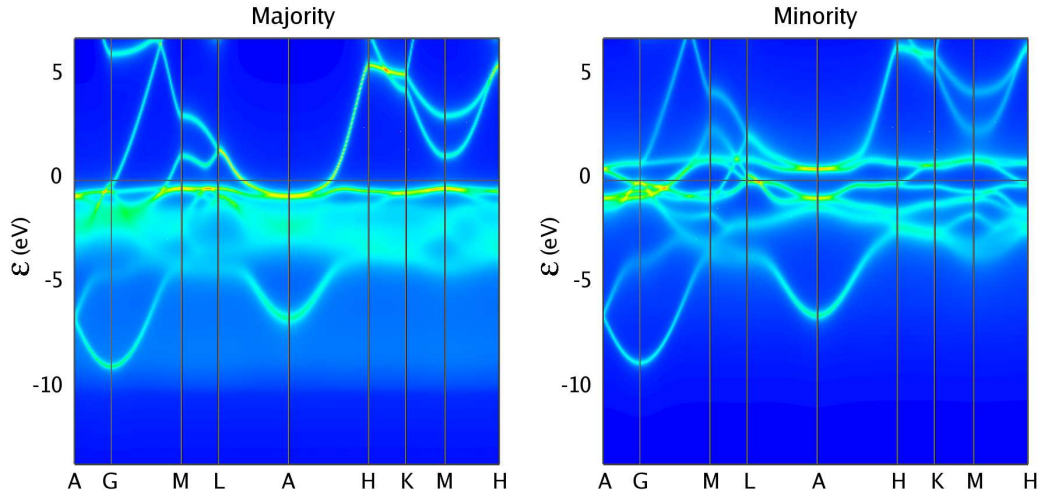

Figure 4.9: Spectral densities of hcp Co from the LDA+DMFT scheme with MT correlated orbitals at $T = 400$ K.

in addition to having the narrowest bands also has the smallest spin polarization. Therefore the difference between majority and minority spin behavior is less profound in Ni compared to Fe and Co, resulting in a pronounced noncoherent feature in both spin channels. If we compare the calculated spin-dependent renormalization factors Z_σ (the spectral weights of the quasiparticle peak, or, in the DMFT, inverse effective mass enhancement factors) for Fe (0.72, 0.71), Co (0.78, 0.83), and Ni (0.82, 0.81) it is clear that the correlation effects in transition metals are not very strong, but still Fe has the largest renormalization.

In Figure 4.7 both the density of states of fcc Ni and hcp Co are presented, while Figures 4.8 and 4.9 show the spectral density for these materials. The density of states of Ni is in a good agreement with previous LDA+DMFT calculations [78]. Note that the SPTF solver places the majority-spin satellite at about -7.5 eV, while in experiment it is observed at -6 eV. Since bcc Fe, fcc Co and fcc Ni have different crystal structure, their band structures naturally look different. However, all the three metals have strong smearing of majority-spin bands between approximately -4 eV and -7 eV dictated by the peak in the imaginary part of the self-energy (see Figure 4.6), and show a satellite at about -7.5 eV.

The LDA+DMFT values of the spin magnetic moments are substantially equal to the LDA values (e.g. for bcc Fe we have $\mu = 2.23\mu_B$ per atom from the DMFT calculation which should be compared to $\mu = 2.22\mu_B$ per atom from LSDA, and for hcp Co we obtain $\mu = 1.54\mu_B$ per atom from the DMFT calculation which should be compared to $\mu = 1.57\mu_B$ from LSDA). The effect of the correlations on spin and orbital moments is an interesting problem. Concerning Fe, Co and Ni it has been recently investigated [103] by means of a different LDA+DMFT implementation that employs the same SPTF solver used here. The results agree with experiments, provided that an adequate choice of the double counting is used.

4.3 DMFT and three-body scattering approach

In the previous Sections we have described the correlation effects in the itinerant ferromagnets in a general form. Here we consider hcp Co as benchmark for a direct comparison between theoretical spectral densities and experimental data from angular resolved photoemission. An important premise to this comparison is that the photoemission spectrum is supposed to reproduce the spectral functions only in first approximation. For a perfect quantitative agreement it is necessary to consider additional details, e.g. the transition matrix elements between initial and final states of the electrons, or the correct potential barrier at the surface.

At the left side of Figure 4.10 we report the LDA+DMFT spectral densities for both majority (top) and minority (bottom) spins along the direction $\Gamma - A$ in the first Brillouin zone. This high-symmetry direction can be explored by changing the angle of the incident light on the sample. The experimental data, corresponding to
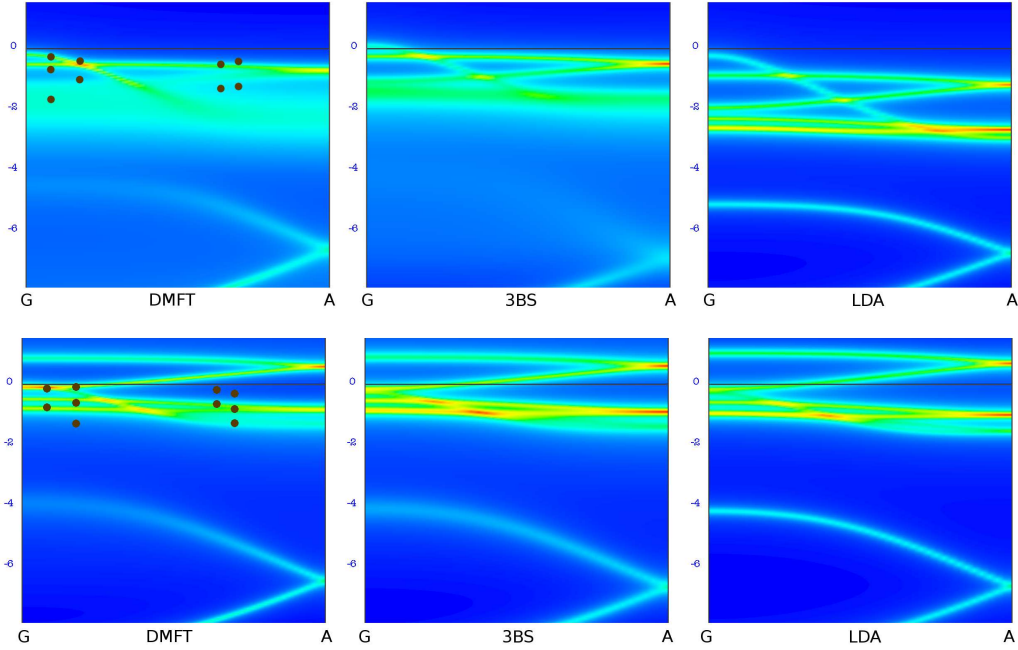
Figure 4.10: Spectral functions of the electrons with majority spin (top) and minority spin (bottom) in hcp Co. On the left the LDA+DMFT results are compared with the experimental data from photoemission, represented by brown dots. For comparison the spectral functions from 3-body scattering (middle) from Ref. [117] and standard LDA (right) are reported.

the position of the peaks in the photoemission spectra[3], are visualized using large brown dots. In addition to the LDA+DMFT data, also the spectral functions obtained in DFT-LDA[4] (right) and in three-body scattering approach (middle) [117] are shown. The 3-body scattering theory is another method for treating dynamical correlation effects in real materials, and a comparison with DMFT is an interesting topic. For a clear presentation of the theoretical formalism of 3-body scattering we redirect the reader to Refs. [113, 118, 119].

Let us focus on the spectral densities for majority spin. Two main points can be emphasized. First of all, by looking at the whole Brillouin zone, we can say that the LDA+DMFT spectral functions reproduce the experimental data better than standard LDA. While the latter one seem to be right in the region close to Γ, its deficiencies are evident in the region close to A. Here the shrinking of the $3d$ band due to correlations becomes necessary to describe the photoemission process. The other point to emphasize is the similarity between the results obtained in LDA+DMFT and 3-body scattering. Both methods are based on the LDA+U

---

[3]More precisely they are obtained through fitting of various measurements.

[4]In this case it would be better to speak of band structure, since the spectral functions reduce to a series of Dirac delta
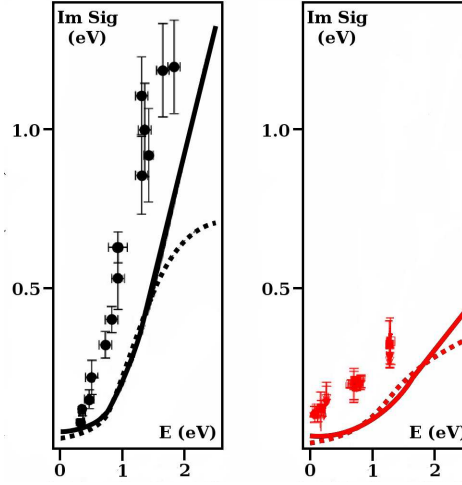
Figure 4.11: Imaginary part of the self-energy for majority (right) and minority (left) spins. The points correspond to the experimental data, extracted from the width of the photoemission peaks. The dotted lines are the LDA+DMFT self-energies, averaged over the correlated orbitals. The solid lines are data from 3-body scattering for analogous U and J. The experimental data comprehend more contributions, in addition to the electronic one, e.g. the scattering with defects can be estimated to correspond to a rigid shift of about $50 \div 100$ meV.

Hamiltonian, defined for the same $U = 2.3$ eV and $J = 0.9$ eV. Besides that, we must consider that their implementations are based on different DFT codes, with different LDA basis sets and different subsets of correlated orbitals. In addition the U-matrix used in 3-body scattering is the density-density approximation (see Chapter 8) of the full U-matrix in equation (3.36). The only noticeable difference is a small rigid shift of the $3d$ band: this is due to the fact that the 3-body scattering implementation used for this calculation is not a conserving approximation. Consequently the Fermi level cannot be determined with high precision. At the bottom of Figure 4.10 we can look at the spectral densities for minority spin. As we have emphasized in the previous Section, the correlation effects are weaker than for majority spin, and so the correlated spectral functions are not very different from the LDA ones. In fact all the three theories show good agreement with experimental data. Notice that some surface states are visible, e.g. at the two experimental points at low energy and close to A.

Finally the quasiparticles life-times can be extracted from the width of the peaks of the photoemission spectrum, and an "experimental self-energy" can be compared to the theoretical one (Figure 4.11). The general agreement is good, especially considering that the comparison can be only qualitative, since the experiment takes into account various contributions, in addition to the electronic one. In particular we could estimate the scattering with defects to give a rigid shift of about $50 \div 100$ meV.

Chapter 5

Correlation effects on surfaces of itinerant-electron ferromagnets

We have already mentioned that one of the main motivations for the development of our LDA+DMFT code has been the study of crystal surfaces. In the community of the strongly correlated materials the simulations are usually limited to the bulk systems with a few atoms per unit cell, which requires an easier implementation (in the development phase) and a smaller numerical effort (in the computational phase). Nevertheless the correlation effects at the surface become more important than in the bulk, since the electrons acquire more atomic-like character. In this Chapter we apply our LDA+DMFT scheme to the study of the surfaces of the itinerant-electron ferromagnets: bcc Fe (001), fcc Co (111), hcp Co (0001) and and fcc Ni (111). Our analysis and comparison with the correspondent bulk results represent a systematic way to check how the correlation effects depend on the dimensionality of the problem. In the last Section of the Chapter a detailed comparison with recent experimental data is presented for the surface (110) of Fe.

The present Chapter is based on the following publications:

1. A. Grechnev, I. Di Marco, M. I. Katsnelson, A. I. Lichtenstein, J. Wills, and O. Eriksson "Theory of bulk and surface quasiparticle spectra for Fe, Co, and Ni", *Phys. Rev. B* **76**, 035107 (2007)

2. J. Sánchez-Barriga, J. Fink, V. Boni, I. Di Marco, J. Braun, J. Minár, A. Varykhalov, O. Rader, H. A. Dürr, V. Bellini, F. Manghi, H. Ebert, A. I. Lichtenstein, M. I. Katsnelson, O. Eriksson and W. Eberhardt "About the correlation effects in the spin-dependent electronic structure of Fe", *in preparation for Phys. Rev. Lett.*

5.1   Ni (111)

The first results to be presented concern the surface (111) of fcc Ni. We have modelled it with slabs having a different number of close-packed atomic layers. Such slabs form a superlattice with a 30 Å thick layer of vacuum separating them, with each slab having two (111) surfaces. The most of the simulations have been made for five-layer slabs. In order to check the dependence of the results on the slab thickness, data for three-layer slabs are also presented in some figures. As it turns out, the surface self-energies of three-layer and five-layer slabs practically coincide. That makes consideration of slabs thicker than five layers unnecessary[1]. The computational details of the LDA part of the LDA+DMFT scheme are similar to the bulk ones, specified in Chapter 4. The $4s$, $4p$ and $3d$ states have been considered as the valence electrons, and two tail energies κ have been used. The two-dimensional Brillouin zone has been sampled with 121 **k**-points.

In Figure 5.1 we show the imaginary part of the self-energy for the atoms in the Ni slabs. Data for each layer of the three-layer and five-layer slabs are compared with the bulk fcc Ni. As expected, the self-energy of an atom at the surface is quite different from the self-energies for the rest of the atoms in the slab. Conversely the self-energy for the central atoms are quite similar to the bulk curves presented

---

[1]Some simulations have been made also with slabs of seven and nine layers, showing that five layers are enough to simulate Fe, Co and Ni, at least at the level of quasiparticle spectra.

(a) Majority spin
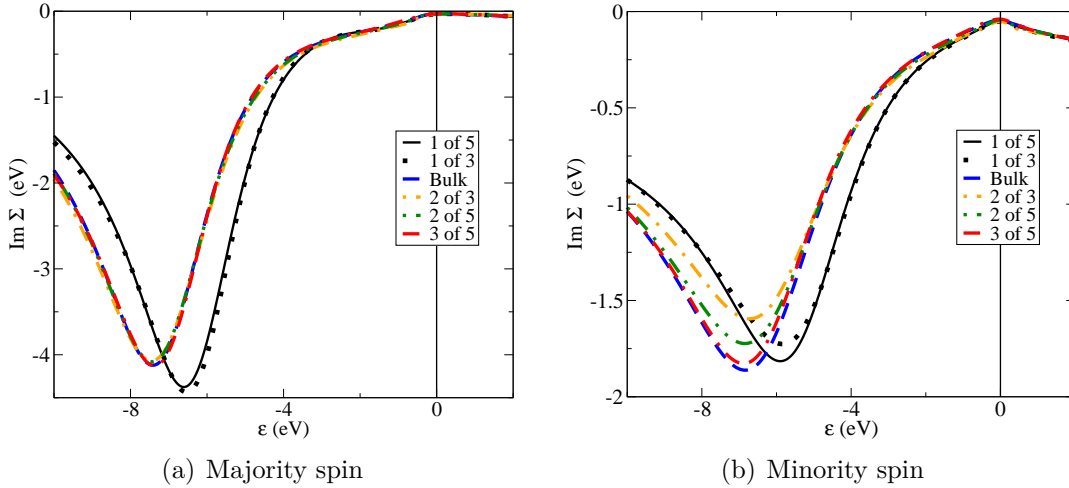
(b) Minority spin

Figure 5.1: Imaginary part of the self-energy $\mathrm{Im}\,\Sigma(\epsilon + i\delta)$ for Ni five-layer (111) slab and three-layer (111) slab. Both majority and minority spin are reported, for the MT correlated subspace, and $T = 400$ K. In the legend "1 of 5" indicates the surface atom of the five-layer slab, "2 of 5" the sub-surface atom and "3 of 5" the quasi-bulk atom. Similarly "1 of 3" indicates the surface atom of the three-layer slab and "2 of 3" the quasi-bulk atom.

Figure 5.2: At the surface (red atoms) the coordination number, i.e. the number of nearest neighbors, is reduced with respect to the bulk (blue atoms). The black lines represent the bonds with the nearest neighbors between the visualized atoms.
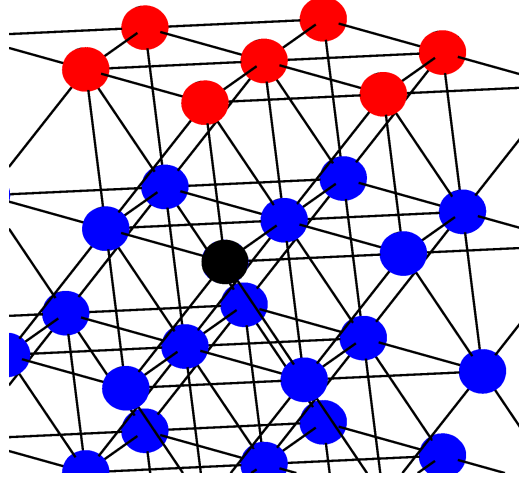
in Section 4.2. The most noticeable difference between surface and bulk values is that the positions of the peaks are shifted and that the correlation effects for majority spin electrons seem to be enhanced at the surface compared to bulk. The reasons for the difference between bulk and surface behavior is rather obvious: due to the reduced coordination number of the surface atoms (see Figure 5.2) the bands become narrower, which makes correlation effects more important. In addition, the screening of the electron-electron interaction is less effective for the surface atoms, and this increases the value of the Hubbard U. When comparing self-energies for spin up and spin down states one may note that there is a shift to higher energies of the main peak of the curves for the surface atoms for both spin channels. The magnitude of the peak is enhanced for the spin up states, but not for spin down.

Although the basic mechanisms are easily identified for why correlation effects are stronger at the surface, our calculations provide a quantitative measure of this effect. They show that, as long as the correlation effects are concerned, the sub-surface layer ("2 of 5") already behaves quite bulk-like. In other words, the DMFT self-energy of an atom depends only on its local coordination number, and not on its actual position in the slab. This is a rather important result deserving experimental attention. Photoemission experiments (preferably spin polarized) of monolayers of Fe, Co or Ni on substrates like MgO, where there are no d-states of the substrate in the energy region with dominating valence band d-character, would be an excellent way to probe the effects of correlation effects in reduced dimensions.
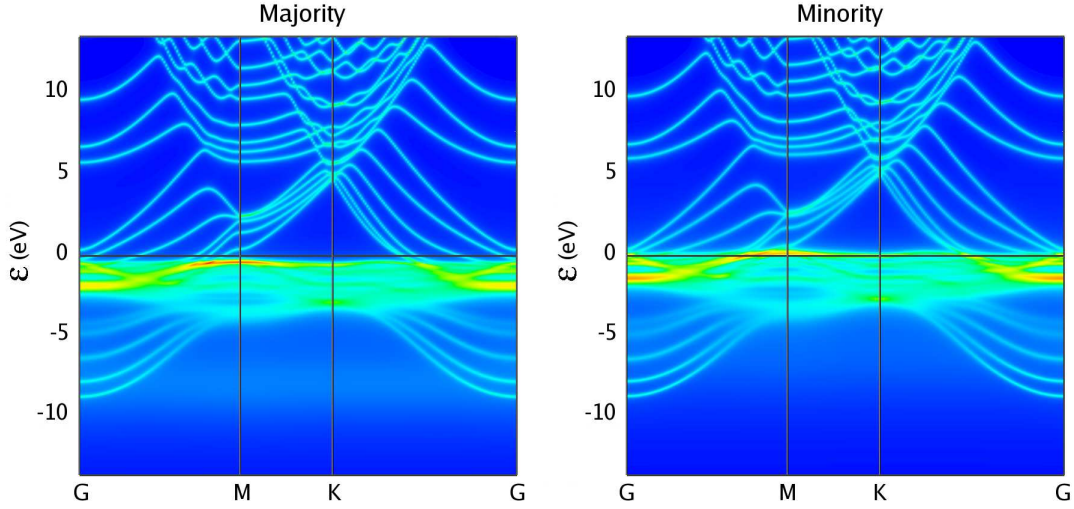
Figure 5.3: Spectral densities of Ni (111) surface modeled by the five-layer slab (from LDA+DMFT with MT correlated orbitals at $T = 400$ K).

Finally the spectral density of the Ni five-layer slab is presented in Figure 5.3 along high-symmetry directions of the two-dimensional Brillouin zone. We can clearly observe that for well-defined quasiparticles, each band of the bulk Ni splits into five bands for the five-layer slab. Some of the bands are surface states, while the rest joins into the bulk continuum when the number of atomic layers go to infinity. In Figure 5.3, it is already possible to observe the surface states (isolated bands) and the hint of the bulk continuum formation (several bands that are very close to each other). The analysis of the surface states (or also the surface resonances) can be very important for the interpretation of the experimental data from photoemission, especially for low energies of the incident photon.

5.2   Co and Fe

We have studied the surface (001) of Fe by modeling it with a five-layer slab. The entire procedure is analogous to the study of Ni (111), and the same computational settings have been used. For Co two different surfaces have been studied: fcc (111) and hcp (0001). Both the systems are modelled with five-layer slabs, but the supercell for hcp Co (0001) contains a double number of atoms, given that the hcp structure has two atoms in the primitive unit cell.

The qualitative discussion of the results obtained with these simulations is similar to the one made for Ni (111), and then will not be repeated. In Figures 5.4 and 5.5 the spectral functions of Co and Fe surfaces are shown.

The first evident feature is that one can hardly see any dispersion of the major-

(a) fcc Co (111)
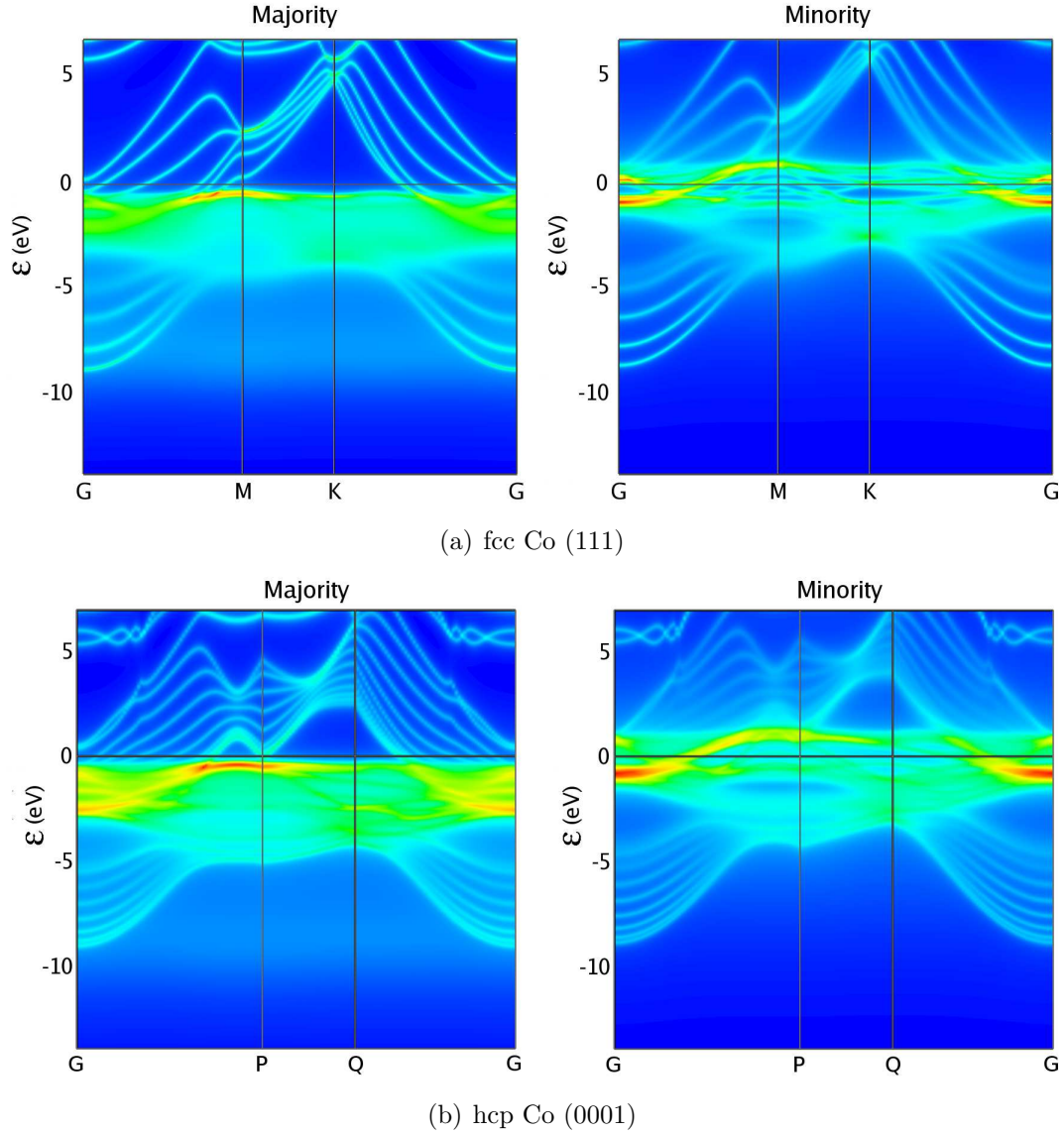
(b) hcp Co (0001)

Figure 5.4: Spectral densities of fcc Co (111) surface and hcp Co (0001) surface, modelled by five-layer slabs (from LDA+DMFT with MT correlated orbitals at $T = 400$ K).

ity spin bands from the Fermi energy down to -5 eV. Furthermore we can notice two main differences with respect to the results for Ni: for majority spin the shift of the peaks and the increase of their depth for the atoms at the surface are stronger, while for the minority spin the correlation effects are decreased (slightly for Co and strongly for Fe). This is again related with the largest spin-polarization for iron and occupation of the d-band closer to the half-filling than for cobalt and nickel. The results is the largest broadening effects for majority spin-state and
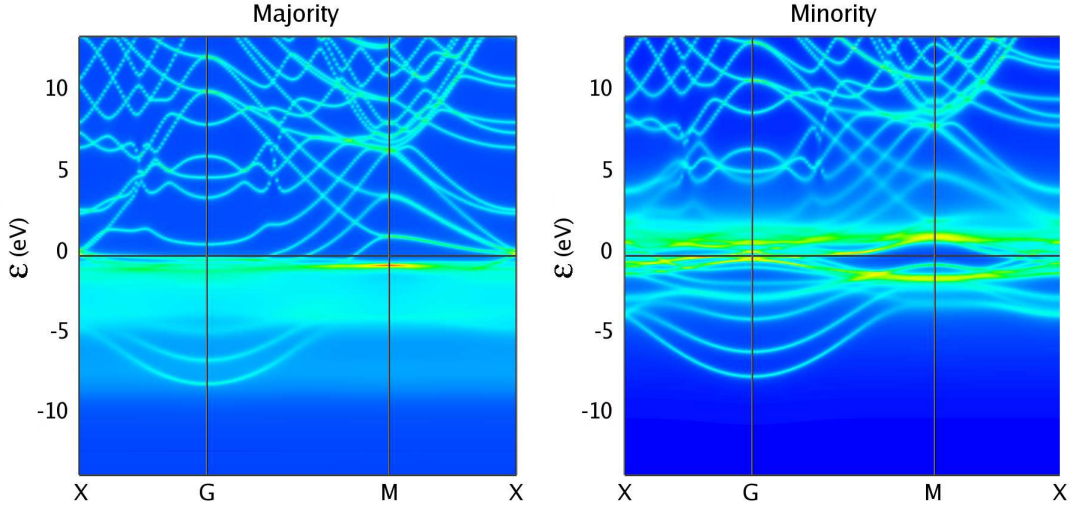
Figure 5.5: Spectral densities of Fe (001) surface modeled by the five-layer slab (from LDA+DMFT with MT correlated orbitals at $T = 400$ K).

strong reduction of correlation effects for minority spin-states in iron. In principle this could be seen in *ad hoc* spin-polarized angular resolved photoemission experiments.

In Figure 5.6 we show the real part of the self energies for the atoms at the Fe surface, and the bulk curves are also shown for comparison. We observe that

(a) Majority spin
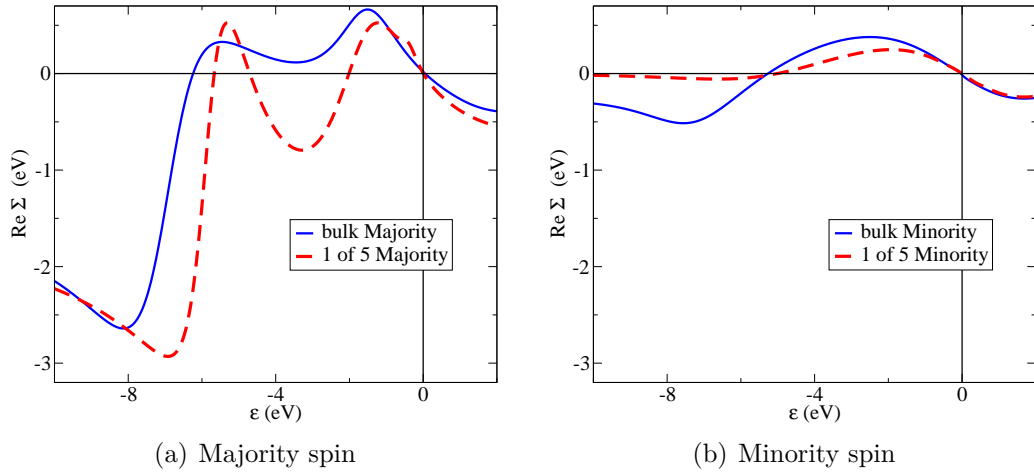
(b) Minority spin

Figure 5.6: Real part of the self-energy $\mathrm{Re}\,\Sigma(\epsilon + i\delta)$ for Fe five-layer (001) slab from LDA+DMFT with MT correlated subspace, and $T = 400$ K. Both majority and minority spins for the surface atom (labelled "1 of 5") are reported, and are compared to the bulk values.
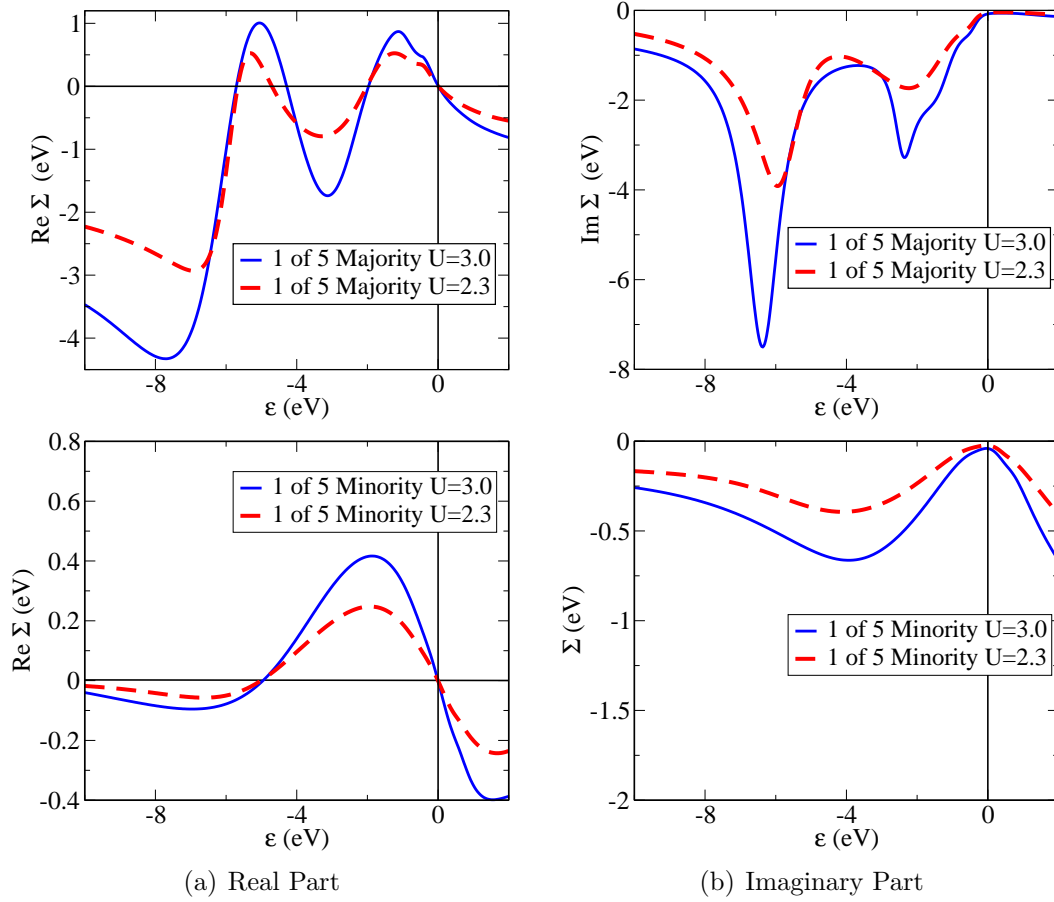
Figure 5.7: Real and imaginary part of the self-energy $\Sigma(\epsilon + i\delta)$ for Fe five-layer (001) slab with different values of U (see main text). Both majority and minority spin are reported, from LDA+DMFT with MT correlated subspace, and $T = 400$ K.

for the surface layer the self-energy of the minority spin states is considerably suppressed, which leads to the fact that the satellite at -7.5 eV is almost totally polarized and possesses majority spin character. This is probably related with increasing of spin-splitting for the iron atom on the surface, which further reduces the minority spin self-energy.

Finally we discuss an important problem related to the evaluation of the Coulomb matrix for the atoms located at the surface. We have mentioned in Section 2.4 how problematic is the choice of a suitable value of the effective interaction U. For the surfaces the difficulties are bigger, due to the fact that all the first-principle and semi-empirical calculations available in literature are referred to bulk materials. However the strength of the interactions of bulk atoms and surface atoms can be very different, due to the presence a different screening. While this thesis has not been dedicated to the problem of the evaluation of U, we have

Figure 5.8: Spectral densities of Fe (001) surface modeled by the five-layer slab and with values of U depending on the position of atom in the slab (from LDA+DMFT with MT correlated orbitals at $T = 400$ K).
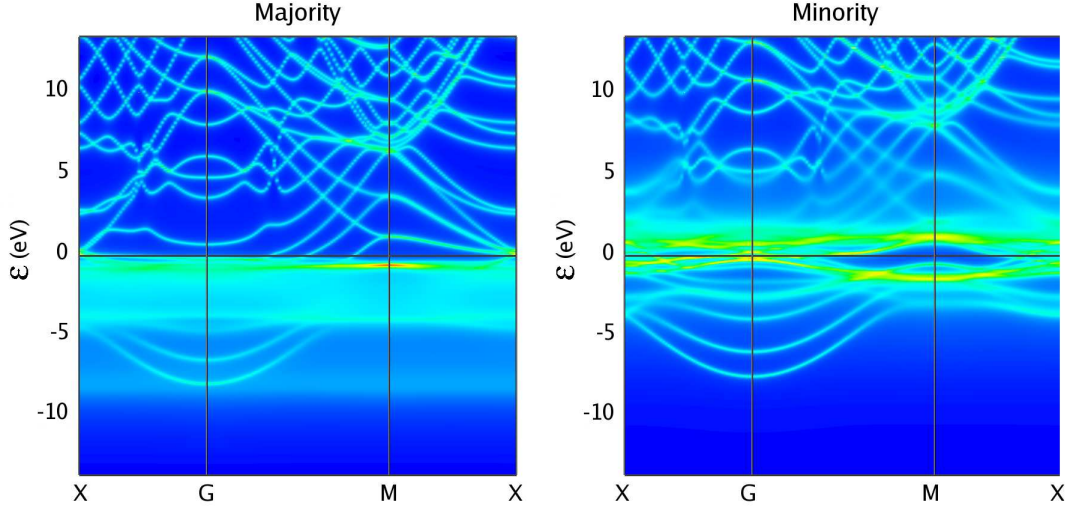
tried to simulate the reduction of the screening by defining different U-matrix for atoms belonging to different layer. We have made LDA+DMFT simulations of a five-layer slab Fe (001) with $U = 2.3$ eV for the inner layers, $U = 2.4$ eV for the intermediate one and $U = 3.0$ eV for the surface one.

In Figure 5.7 the real and imaginary part of the self-energy for the atoms at the surface in these new simulations are reported. In comparison to the previous calculation with the constant U, whose curves are also shown in the picture, we observe a reasonable increase of the majority spin peaks from -2 eV till -4 eV and a small shift of the -7.5 eV satellite. This makes the satellite more pronounced in the density of states. The spectral densities of these last simulations are reported in Figure 5.8. One can see a strong increase of the broadening in the majority channel and an incoherent satellite band at the bottom of the majority $3d$ band.

5.3   Fe (110)

The last Section of this Chapter is dedicated to the direct comparison with experimental data from angular resolved photoemission. The benchmark is the surface (110) of Fe, which has been probed through light with vertical and horizontal polarization for different photon energies. These data are reported respectively in Figures 5.9 and 5.10. In the same pictures, the results from LDA and LDA+DMFT simulations are shown. These calculations have been made with the same computational settings specified above. In addition the spin-orbit coupling has been

Figure 5.9: Comparison between photoemission spectra (black circles) for vertically polarized light and LDA+DMFT spectral functions (segmented red line) for various points of the surface Brillouin zone along the direction ΓN. Majority and minority spins are respectively reported in the upper and lower parts. For comparison the LDA spectral functions (blue line) are also shown.

considered.

The first issue to discuss is the agreement between LDA spectral functions and experimental spectra. For majority spin, and vertical polarization, LDA seems to give good results close to the Γ point (0.06GN in Figure 5.9), but definitely worse results when going towards the N point. However a comparison with the results for horizontal polarization (0.21GN in Figure 5.10) reveals that the peak close to the Fermi level originates from a surface state, and that the real bulk state is at 0.2 eV lower energy. Indeed the latter can be observed also for vertical polarization, but only as a small shoulder of the surface peak, at −0.7 eV. When we consider the LDA+DMFT spectral functions we see that the bulk state is shifted towards the experimental position, consistently with the shrinking of the 3d-band mentioned in Section 4.1. Also in the rest of the Brillouin zone the LDA+DMFT agreement at low energies is much better than standard LDA. Notice that another surface state is visible for vertical polarization at 0.33GN (Figure 5.9), and that some transitions are prohibited because of selections rules (in the spectral functions these effects are not included).
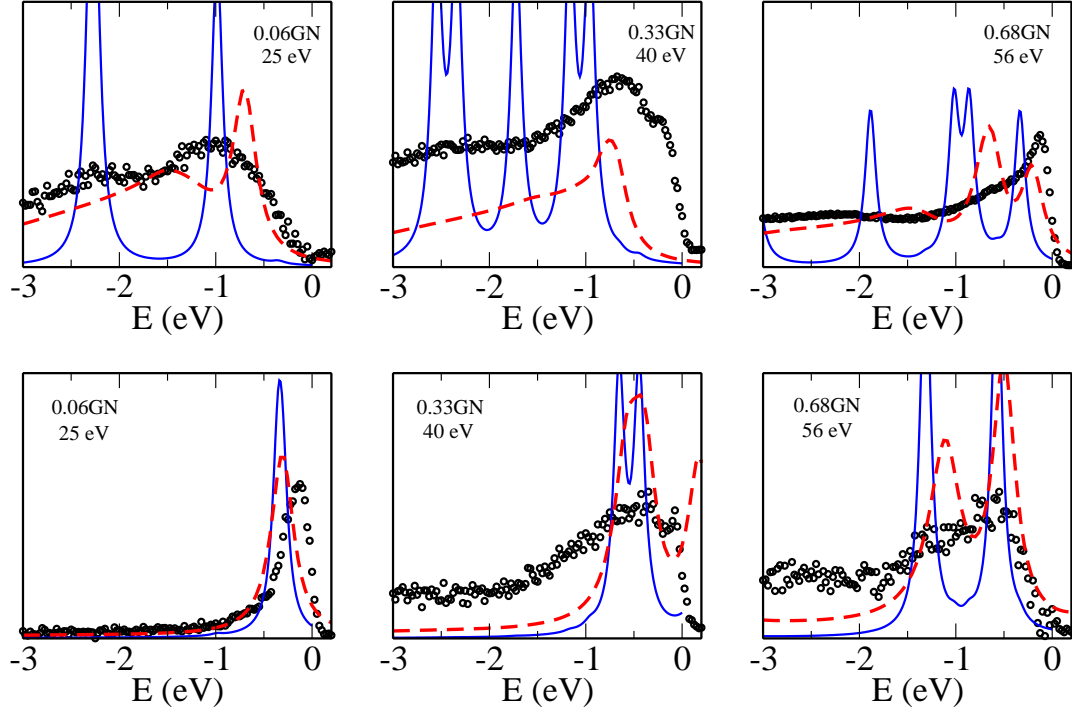
Figure 5.10: Comparison between photoemission spectra (black circles) for horizontally polarized light and LDA+DMFT spectral functions (segmented red line) for various points of the surface Brillouin zone along the direction ΓN. Majority and minority spins are respectively reported in the upper and lower parts. For comparison the LDA spectral functions (blue line) are also shown.

Let us now look at minority spin states. Again the LDA+DMFT results agree with the experimental data better than the standard LDA. While the correlation effects are generally smaller than for majority spin, a big shift is observed close to N for horizontal polarization (picture 0.94GN in Figure 5.10). The LDA peak at -1.6 eV moves of about 0.4 eV towards lower energies. From the same picture we notice a big peak close to the Fermi energy, which we assume to be another surface state. A clarifying visualization is given in Figure 5.11. Here the photoemission data and the bulk spectral function are compared to the spectral function projected on the atom at the surface. All the states can be clearly identified.

For higher energy the situation becomes more complicated. Let us focus again on the majority spin at the picture 0.06GN in Figure 5.9. While the LDA fails close to the Fermi energy, the state at -2.3 eV seems to be well reproduced. When we pass to the LDA+DMFT scheme we see that this state gets shifted towards the Fermi level when the band shrinks. This can suggest that the effective value of the Hubbard U in Fe is smaller than the commonly accepted value of $U = 2.3$ eV. For a value of $U = 1.5$ eV an intermediate situation between our LDA and LDA+DMFT
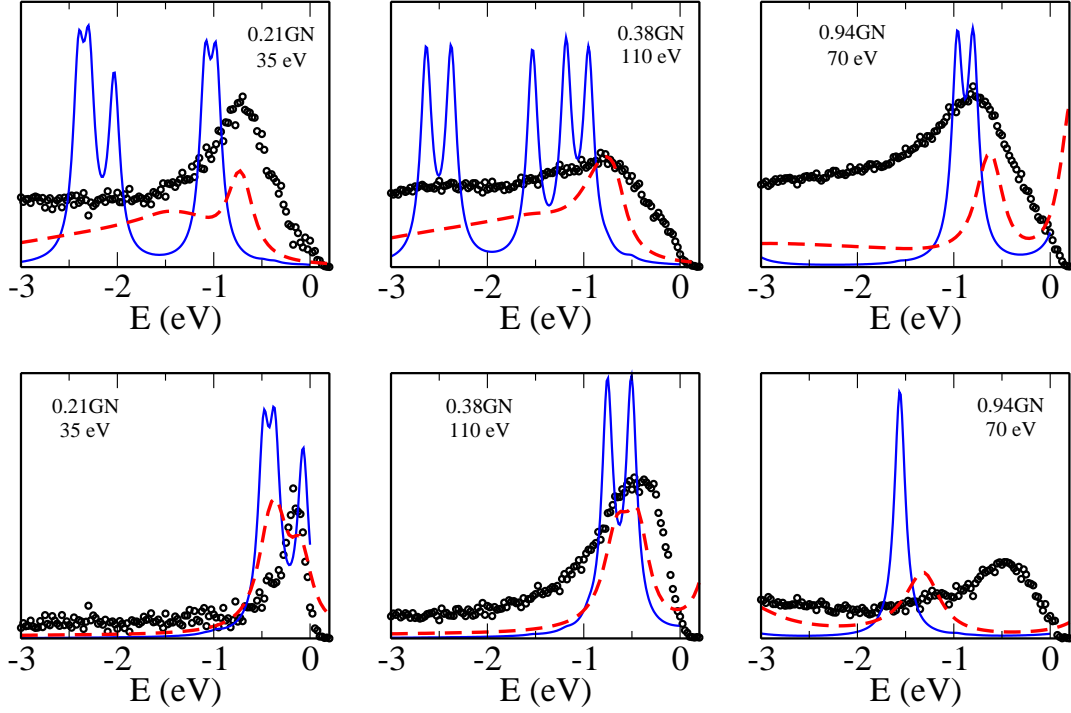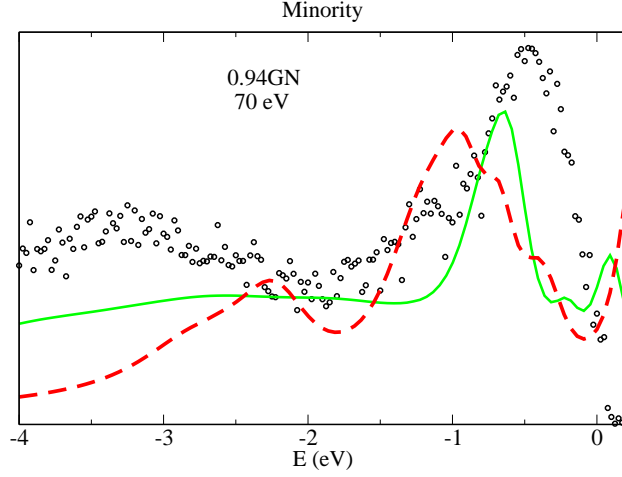
Figure 5.11: Comparison between photoemission spectra (black circles) for horizontally polarized light and LDA+DMFT spectral functions projected onto the surface atom (green line) for the point 0.94GN of the surface Brillouin zone. For comparison the LDA+DMFT spectral functions projected on the quasi-bulk atom (segmented red line) are also shown.

curves can be obtained and the final photoemission spectrum can be justified in terms of broadening of the final state [120]. However this reduction of U would be unphysical, since experimental data and theoretical estimations seem to exclude such low values. A good *a posteriori* justification of our statement is given by the excellent agreement observed in this Section for all the low energy features close to the Fermi energy for both spin channels. In second instance we have to notice that also for a reduced value of U the non-dispersive nature of the peak at -2.3 eV cannot be properly explained. The last problem could be solved if we suppose the existence of a surface resonance. In fact the LDA+DMFT calculations of the five-layer slab above shows a non dispersive state[2] at the energy of -2.8 eV. Nevertheless the most reasonable explanation relies in the strong non-locality of correlation effects in bcc Fe, as follows from recent direct photoemission data on effective mass renormalization in different points of the Brillouin zone [121]. These effects are beyond DMFT, and cannot be reproduced with our approach.

---

[2]This result has been checked up to nine-layer slab.

Chapter 6

Correlation effects in 2D magnetic systems: Fe on W

The control of the magnetic state in artificial materials is one of the fundamental issues of material science in perspective of technological applications. In the last fifteen years ultrathin films have attracted much attention, since they exhibit a rich variety of properties [122]. In these low-dimensional systems the main magnetic properties, e.g. magnetic structure, magnetization direction, magnetic moment, or ordering temperature, can strongly differ from the corresponding bulk quantities. Most importantly they can originate from different physical parameters. First of all the reduced number of nearest neighbors, mentioned in the previous Chapter, leads to electrons with more atomic-like character and larger spin and orbital moments. In addition the hybridization effects with the substrate can have a key role in determining the exchange interactions between the atoms in the film [123]. In this view it is natural that the many-body effects become fundamental for a proper description of the electronic structure.

Here we present the application of the LDA+DMFT scheme to one monolayer of Fe on the substrate (001) of W. After a brief overview of this system, the results of our simulations are presented in detail. Finally an interpretation of our findings is given in terms of mean-field theory of the Hubbard model.

The present Chapter is based on the following publication:

1. A. Kubetzka, I. Di Marco, M. Bode, M. Menzel, K. von Bergmann, S. Heinze, P. Ferriani, M. I. Katsnelson, A. I. Lichtenstein and R. Wiesendanger "Narrowing of the pseudogap at the Fermi level for antiferromagnetic Fe layer on W(001) surface", *in preparation for Nature Materials*

6.1   Fe:W(001)

The magnetism of one monolayer of Fe is the prototypical example of the peculiarities of ultra-thin films. After deposition on substrates Cu (111) and Ag (111), the local magnetic moment, which in the bulk is about $2.1\mu_B$, increases to respectively $2.7\mu_B$ and $3.2\mu_B$, not too far from the atomic value $4\mu_B$ [124]. More fascinating effects happen with a more complex substrate as W. If the Fe monolayer is deposited along the direction (001), the ground-state passes from a ferromagnetic to an antiferromagnetic structure [125]. The same phenomenon is observed for one monolayer of Co, while Ni becomes non-magnetic [122]. On the other hand Cr and Mn, which in their bulk phases are antiferromagnetic, acquire a ferromagnetic ground-state. The situation is still more puzzling in view of the fact that the same monolayers keep the original magnetic phase when the deposition on W is made along the direction (110) [126, 127].

Together with the experimental discovery of the antiferromagnetic structure of Fe on W (001), Kubetzka *et al.* [125] made first-principle calculations to understand the role of the substrate. They found that decreasing the interlayer distance d, starting from a really 2-dimensional unsupported monolayer, drives the system from a ferromagnetic ground-state ($d > 4.5$ a.u.) to an antiferromagnetic ground-state (1.7 a.u. $< d < 4.5$ a.u.) and finally to a non-magnetic ground-state ($d < 1.7$ a.u.). On the basis of these results Ferriani *et al.* [122] proposed that during the transition the antiferromagnetic interlayer exchange interactions Fe-W become dominating against the ferromagnetic intralayer exchange interactions Fe-Fe. Later Sandratskii *et al.* [123] have proved that this hypothesis is not correct. By mapping the system onto an Heisenberg Hamiltonian they have shown that the hybridization with the substrate changes directly the exchange interactions Fe-Fe from ferromagnetic to antiferromagnetic through the modification of the local electronic structure at the surface.

Our interest in this system originates from the attempt of explaining the tunnel spectroscopy data shown in Figure 6.1(a), and measured at $T = 13$K with an Fe coated W tip. We can see that at small energy scale a pseudogap appears in the dI/dU curve. Given that this quantity is proportional to the surface density of states, we expect to obtain an analogous pseudogap from electronic structure calculations, but it was not observed in the Refs. mentioned above.

To understand the physical reasons that lead to the formation of this pseudogap at the Fermi level, we have performed first-principles calculations in the DFT-LDA and LDA+DMFT scheme. We have modeled our system as a symmetric slab of nine atomic layers ordered in the bcc crystal structure with the experimental W lattice constant of 5.98 a.u.. The seven layers at the center of the slab are formed by W atoms, while the last layer on each side consists of Fe atoms. The magnetic phase was assumed to be the c(2x2) antiferromagnetic structure depicted
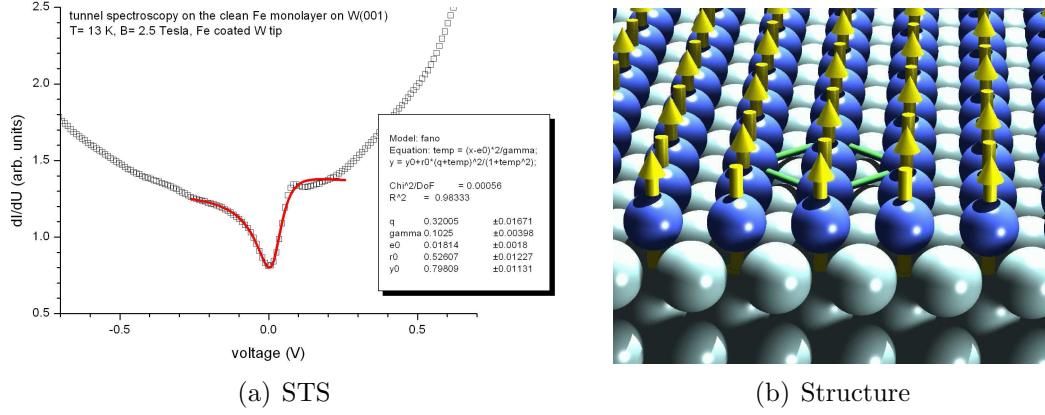
(a) STS

(b) Structure

Figure 6.1: Left: Tunnel spectroscopy data on the clean Fe monolayer on the substrate W(001); the measurements have been done at temperature $T = 13$ K and under the action of a small magnetic field $B = 2.5$ T by means of a Fe coated W tip. Right: ground-state magnetic structure in the c(2x2) arrangement: the magnetic moments form a "checkboard" on the surface. Picture from Ref. [124].

in Figure 6.1(b). The interlayer distance between each of the Fe layers and the closest W layer has been set to 2.57 a.u., corresponding to the equilibrium value for the corresponding magnetic structure [123, 125]. Finally we have completed our super-cell with a layer of vacuum of more than 20Å. In fact we must mention that thicker layers of vacuum were applied for the DFT-LDA simulations, but no effects could be noticed on the main properties. In perspective of the full LDA+DMFT cycle, for which 18 atoms in the unit cell represent a highly expensive task, it has been important to minimize the size of the basis set used to solve the DFT-LDA problem. Hence the 4f and 5p states of W have been treated as core states, and we have found this choice to be good if the radius of the muffin tin spheres is big enough. Then for W we have used a muffin-tin sphere corresponding to the maximum radius allowed in the chosen geometry, i.e. 2.57 a.u., while for Fe a value comparable to the bulk one has been chosen, i.e. 2.16 a.u.. Many different combinations of tail energies have been tried in such a way to minimize the errors due to the numerics of the LDA+DMFT scheme, and the ones due to the finite size of the basis set. Then we have found convenient to use two different tail energies for s, p and d electrons. All the calculations included spin-orbit coupling, since it is important for a proper description of W. Convergency on the **k**-mesh lead to a minimal number of 361 **k**-points used in the two dimensional Brillouin zone. Apart from this minimal number, we have tried configurations with different **k**-meshes up to 1681 **k**-points in the Brillouin zone.

The next-step is the definition of the Hubbard term in the Hamiltonian (2.28). Due to the multiple tail energies of the LDA basis, the MT correlated subset has been used. Unfortunately no theoretical calculations of U and J are available for

this system, so we have just considered values similar to the bulk ones. As for Chapter 5, the possibility of a higher value has been considered due to the reduced number of nearest neighbors. We have tried values of U ranging from 2.3 eV up to 5.0 eV, and we have found 4.0 eV to be the most adequate value, which is physically reasonable. The effect of the screening on the Hund's exchange J is usually negligible, then we have used the atomic value $J = 0.9$ eV. These numbers are consistent with the direct calculation of the Slater integrals (3.39) that we have made through the partial wave integration from Ref. [128].

Finally the LDA+DMFT cycle has been solved for a temperature $T = 400$ K, and using 2048 Matsubara frequencies for the linear mesh and 120 frequencies for the logarithmic mesh.

6.2   Results and discussion

In Figure 6.2(a) we have reported the partial $3d$ density of states for a Fe atom in the monolayer from standard LDA. These results agree with the previous calculations [123] up to the smearing induced by the finite distance $i\delta = 50$ meV from the real axis. In the same Figure we can see the LDA+DMFT simulation for $U = 4$ eV at $T = 400$ K. On this energy scale we observe big changes due to the dynamical correlation effects. For majority spin a big transfer of the spectral weight is observed from the region around -2 eV down to -4 eV, and the peak near the Fermi level shifts towards it. For minority spin both the electron and hole states are shrinked towards the Fermi energy. Moreover in Figure 6.2(b) we can observe the real and the imaginary part of the self-energy that correspond to this simulation.

Interestingly from this picture for a large energy scale we can already observe a first hint of the narrowing of the pseudgap at the Fermi level. A more precise analysis can be done looking at Figure 6.3, which is focused on a smaller energy scale. In the upper part the spin-resolved $3d$ density of states for a Fe atom in the monolayer is reported, for both LDA and LDA+DMFT. We can clearly see how the local Coulomb interactions change the flat LDA curve and lead to the formation of a pseudogap. In comparison with Figure 6.1(a) its size is slightly larger: 0.4 eV versus 0.2 eV. More clearly these features can be noticed in the lower part of Figure 6.3, where the projection of the density of states on the real spherical harmonic $3d_{z^2}$ is shown. It is the component that brings the largest contribution to the scanning tunneling spectroscopy. Now the pseudogap results more evident, and in addition the right asymmetry in the heights of the peaks is reproduced.

Finally we can try to obtain more physical insight by looking at Table 6.1. We first compare our LDA value to the ones from Refs. [125] and [123]: the agreement is good, especially considering that their values include also s and p

(a) Density of States

(b) Self-Energy
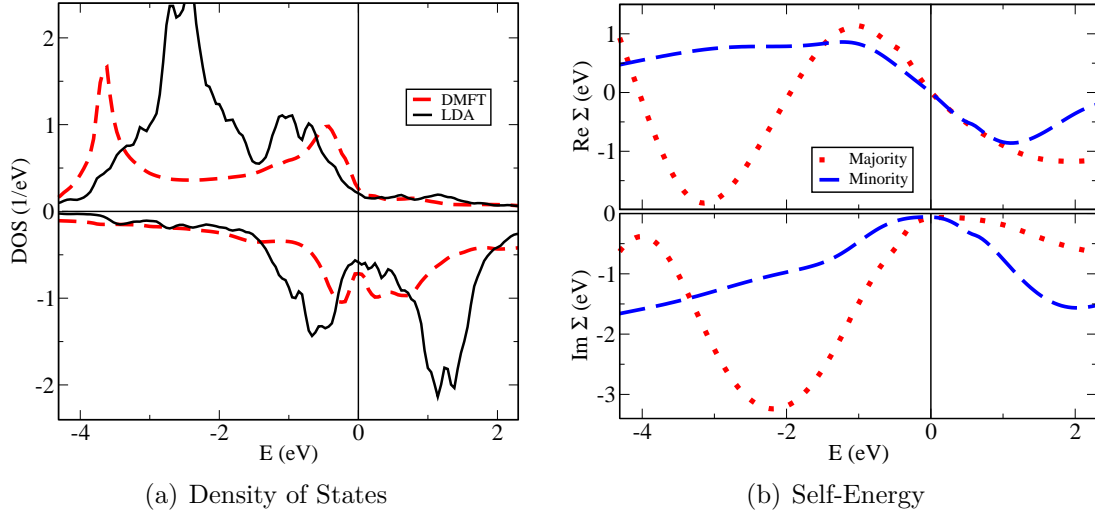
Figure 6.2: Left: $3d$ partial density of states for majority spin (up) and minority spin (down) on a Fe atom in the monolayer; results from standard LDA and from the the LDA+DMFT scheme with MT correlated subset at $T = 400$ K are reported. Right: corresponding real (up) and imaginary (down) part of the self-energy, averaged over the orbital indices as in equation (4.1).

contributions, that the radius of the muffin-tin spheres (for the integration) is not the same, and that different exchange-correlation functionals have been used. In the LDA+DMFT results we observe an increase of the total $3d$ spin moment, but a decrease of the $3d_{z^2}$ component. This is compatible with what observed in the density of states 6.2(a): the pseudogap is already visible in the LDA, but only for a larger energy scale. The strong correlation effects cause a narrowing. Finally notice that the orbital moment gets strongly quenched, probably due to the decrease of the occupation of the minority spin channel, which gives the main contribution.

From the computational point of view the narrowing of the pseudogap is due to the real part of the self energy, that decreases the magnetic moment in the

Table 6.1: First line: $3d$ spin moments for a Fe atom in the monolayer in units of Bohr magneton; notice that the values from Refs. [125] and [123] include also s and p contributions. Second line: $3d_{z^2}$ component of the spin moment. Third line: $3d$ orbital moment.

	Ref. [125]	Ref. [123]	LDA	LDA+DMFT
$3d\quad \mu_s(\mu_B)$	2.67	2.47	2.435	2.492
$3d_{z^2} \mu_s(\mu_B)$	-	-	0.659	0.624
$3d\quad \mu_o(\mu_B)$	-	-	0.186	0.143
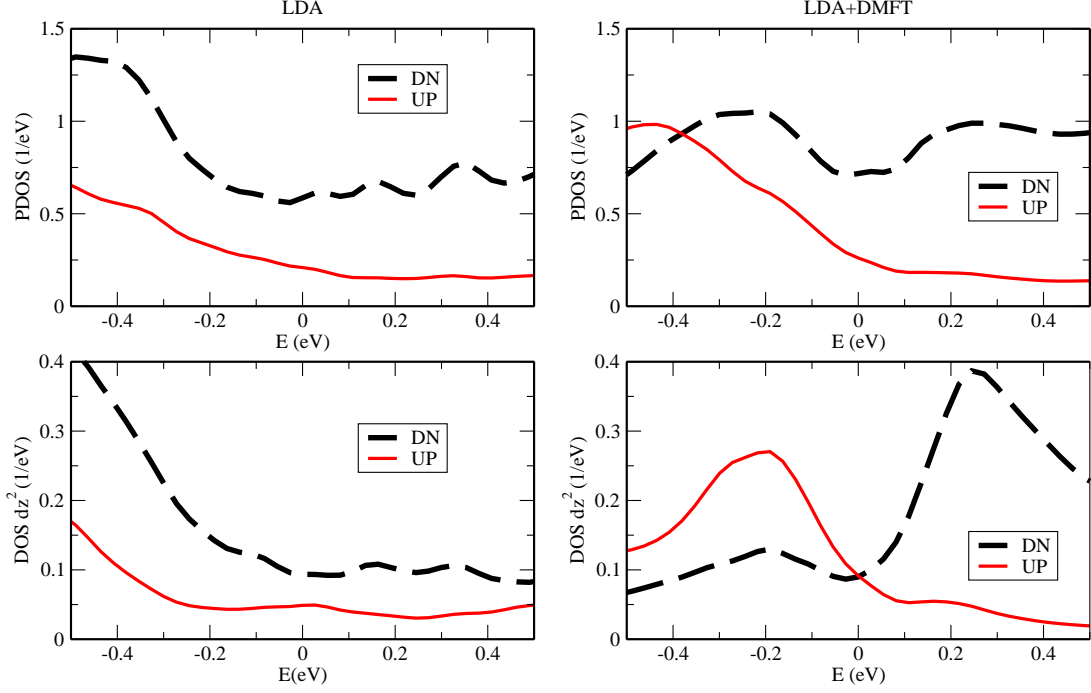
Figure 6.3: Comparison between the spin-resolved density of states for LDA (left) and LDA+DMFT (right) of the $3d$ states for a Fe atom in the monolayer. In the upper part the density of states for all orbital is reported, while in the lower part only the projection on the d_{z^2} orbital is reported.

z direction, bringing the peaks closer to each other. These general features are quite robust, in the sense that they appear for all the tested values of U, and also for different choices of double-counting than equation (3.83). Nevertheless the detailed shape of the pseudogap depend on the chosen parameters.

A more theoretical explanation can be given in terms of the Hubbard model. What we obtain in DMFT is a local self-energy Σ, i.e., a self-energy which depends only on the electron energy E. In paramagnetic case, the main correlation effect for the states near the Fermi energy E_F is the effective mass renormalization by the factor $Z^{-1} = 1 - \partial\Sigma(E)/\partial E|_{E_F}$ which leads to the enhancement of density of states peaks near the Fermi energy or even to a formation of essentially many-electron Kondo peaks like in heavy-fermion systems [70]. In ferromagnets, another interesting correlation effect takes place, that is, a formation of spin-polaronic nonquasiparticle states due to spin-flip virtual processes [30]. In the case of anti-ferromagnetic metals, the formation of an antiferromagnetic gap (or pseudogap) due to magnetic Umklapp processes is essential. In the mean-field approximation we can write down the electron spectrum of an Hubbard model on an antiferro-

magnetic lattice as [129, 130, 131]

$$E_{\pm}\left(\mathbf{k}\right) = \frac{1}{2}\left[t_{\mathbf{k}} + t_{\mathbf{k}+\mathbf{Q}} \pm \sqrt{\left(t_{\mathbf{k}} - t_{\mathbf{k}+\mathbf{Q}}\right)^2 + \Delta^2}\right]$$

where $\mathbf{Q}$ is the antiferromagnetic wave vector, $t_{\mathbf{k}}$ is the bare electron spectrum, and Δ is the antiferromagnetic gap proportional to the sublattice magnetization. In the case of nesting $t_{\mathbf{k}} = -t_{\mathbf{k}+\mathbf{Q}}$ there is a real gap and the system turns out to be an insulator, whereas for a generic spectrum there is just a pseudogap [129, 130]. The latter forms from the region of $\mathbf{k}$-space satisfying the condition $|t_{\mathbf{k}} + t_{\mathbf{k}+\mathbf{Q}}| \leq \Delta$. Correlation effects leads to the bare band flattening, $t_{\mathbf{k}} \to Z t_{\mathbf{k}}$, which makes the pseudogap more narrow. This is exactly the effect which is clearly seen in the DMFT calculations and is observed experimentally.

Analytic consideration of the renormalization of the energy spectrum due to the electron-magnon interaction in antiferromagnets [131] show that in this case the effect should be rather large. In fact the contributions of magnon Umklapp processes to the self-energy contain a logarithmic divergence:

$$Z^{-1} \simeq \ln\left(W/\Delta\right), \tag{6.1}$$

where W is the total bandwidth. To describe this effect quantitatively the $\mathbf{q}$-dependence of the self energy should be taken into account. However, qualitatively it is properly described in the DMFT. It is essential also that the typical energy scale of correlation-induced features in the electronic self-energy is of the order of typical magnon energies [30, 131], i.e. 0.1 eV for our system.

Electron-magnon interaction, as well electron-phonon interaction, leads to "satellites" in the electron spectrum at the energies $E_F \pm \hbar\omega$ where ω is the energy of peaks in bosonic density of states. In the lowest-order approximation the singular contributions to the electron self-energy are symmetric with respect to the Fermi energy E_F; however, the higher-order terms violate this symmetry assuming that both one-boson and two-boson scattering processes are presented in the interaction Hamiltonian [132]. This is exactly the case of electron-magnon interaction in antiferromagnets where the single-magnon (two-magnon) terms correspond to the transverse (longitudinal) spin fluctuations respectively [131]. This can qualitatively explain also the asymmetry that is observed experimentally and in the LDA+DMFT results.

Chapter 7

Correlation effects in the ground-state properties of Ni and γ-Mn

The main interest of the LDA+DMFT community relies on the spectral properties of strongly correlated materials. However, correlation effects are sometimes of crucial importance to describe also cohesive energy, equilibrium lattice constant and bulk modulus, as demonstrated for the cases of plutonium [19, 61], cerium [24, 26] and Ce_2O_3 [133]. All the mentioned studies concern materials with rather localized f-electrons, for which standard one-particle approaches give results that are totally wrong. On the other hand we have shown in the previous Chapters that correlation effects can be important also for materials where the failures of the density-functional theory are milder. The transition metals are a prototypical example, and here we analyze the ground-state properties of fcc Ni and γ-Mn through the LDA+DMFT scheme.

The present Chapter starts with introducing a total energy functional in the LDA+DMFT scheme, in the spirit of the spectral density functional approach [15]. Then the implementation of this functional in our LDA+DMFT code is described, with special emphasis on the problematics related to the numerical precision. The two applications follow: first fcc Ni, which plays the role of "drosophila fly" for the LDA+DMFT method and where the most detailed comparison of the theory with experiment was done [134, 29]. Results of our approach are compared with data from another LDA+DMFT code based on the full-potential KKR [36]. Then, we consider the case of Mn where, among all transition metals, the largest discrepancy between the LDA or GGA predictions for the lattice constant and bulk modulus and the experimental data takes place [135, 136, 137] which is considered to be an indication of the strongest correlation effects among $3d$ metals [138, 116]. We show that the LDA+DMFT method does allow us to solve this problem and to

describe in a very satisfactory way the energetics of Mn.

The present Chapter is based on the following publication:

1. I. Di Marco, J. Minár, S. Chadov, M. I. Katsnelson, H. Ebert, and A. I. Lichtenstein "Correlation effects in the total energy, the bulk modulus, and the lattice constant of a transition metal: Combined local-density approximation and dynamical mean-field theory applied to Ni and Mn", *Phys. Rev. B* **79**, 115111 (2009)

7.1   Total energy functional

In Section 2.5 we have introduced the DMFT as conceptual analogy to the Weiss mean-field theory for a lattice quantum system. The mapping from the Hubbard model onto the effective impurity model can be rigorously justified, in the limit of infinite dimensions, by the scaling of the local and non-local contributions to the effective self-energy of the electrons [73, 5]. However, the DMFT equations can be obtained with many different techniques [14], each one stressing a different physical or mathematical aspect. For calculating the ground-state energy within the LDA+DMFT scheme, it is particularly convenient to adopt the point of view of the spectral density-functional theory of Savrasov and Kotliar [15, 139]. The basic idea is to construct a variational functional that reproduces at the same time the DMFT equations of Section 2.5, and the DFT equations of Section 2.3. The guidelines of the procedure derive from the effective action formalism [75, 15], which is based on the generalization of the concept of Legendre transformation. For example for the standard DFT, the following functional can be introduced:

$$\Omega_{DFT}[V_{KS}(\mathbf{r}), n(\mathbf{r})] = \int d\mathbf{r}\, V_{ext}(\mathbf{r})n(\mathbf{r}) + E_H[n] + E_{xc}[n] +$$

$$- \int d\mathbf{r}\, V_{KS}(\mathbf{r})n(\mathbf{r}) - \mathrm{Tr} \ln \left[i\omega_n + \frac{\hbar^2}{2m}\nabla^2 - V_{KS}(\mathbf{r}) \right]. \quad (7.1)$$

The first three terms are respectively the electrostatic energy due to the external potential, the Hartree energy, and the exchange-correlation energy, as already discussed in Chapter 2. The fourth term contains the Kohn-Sham potential, which has the role of a source field constraining the electron density to have the specified value. Finally the fifth term describes the dynamics of the system, and reminds us of the Luttinger-Ward functional. The trace has to be intended over both the Matsubara frequencies $i\omega_n$ and positions[1] $\mathbf{r}$. If we minimize the functional (7.1) with respect to $n(\mathbf{r})$, we can easily re-obtain the equation (2.20), i.e. the correct

---

[1]In reality any generic representation can be adopted. In fact in the next Section we will write the trace over the orbital degrees of freedom by using the LDA wavefunctions $|\mathbf{k}, \chi\rangle$.

expression of the Kohn-Sham potential in terms of the density. On the other hand, if we minimize the functional 7.1 with respect to $V_{KS}(\mathbf{r})$, we have the condition

$$n(\mathbf{r}) = T \sum_{i\omega_n} \langle \mathbf{r}| \left[i\omega_n + \frac{\hbar^2}{2m}\nabla^2 - V_{KS}(\mathbf{r}) \right]^{-1} |\mathbf{r}\rangle. \qquad (7.2)$$

This expression is equivalent to equation (2.13), where the wavefunctions and their occupations are defined from the Kohn-Sham equation (2.19). In equation (7.2) the occupation of the orbitals (or better the space points $\mathbf{r}$) is set by the sum over the Matsubara frequencies, so it contains already the temperature effects due to the Fermi-Dirac distribution.

Such an approach can be used also for basic DMFT applied to the Hubbard model of equation (1.2), leading to a functional of the local Green's function, which we do not write here. For the LDA+DMFT scheme, we consider the LDA+U Hamiltonian (2.28), and then we need a description based on both the local Green's function and the electron density. The following functional can be constructed:

$$\Omega_{LDA+DMFT}[\Sigma, G, V_{KS}(\mathbf{r}), n(\mathbf{r})] =$$
$$\int d\mathbf{r}\, V_{ext}(\mathbf{r})n(\mathbf{r}) + E_H[n] + E_{xc}[n] + \Phi[G] - \Phi_{DC}[G] +$$
$$- \int d\mathbf{r}\, V_{KS}(\mathbf{r})n(\mathbf{r}) - \text{Tr}\, \Sigma(i\omega_n)G(i\omega_n) +$$
$$- \text{Tr}\ln\left[i\omega_n + \frac{\hbar^2}{2m}\nabla^2 - V_{KS}(\mathbf{r}) - \chi^*\Sigma(i\omega_n)\chi \right]. \quad (7.3)$$

Let us analyze all the terms. In the first line we have the three contributions coming from DFT (see above), plus the contribution from a functional $\Phi[G]$ of the local Green's function. The latter one contains the effects of the interactions, and is defined as the full set of the two-particle irreducible diagrams without external legs. Its meaning, and the meaning of the other term $\Phi_{DC}[G]$ can be understood by applying the stationary condition with respect to the variation of G to equation (7.3). We easily obtain:

$$\Sigma = \frac{\delta\Phi[G]}{\delta G} - \frac{\delta\Phi_{DC}[G]}{\delta G}, \qquad (7.4)$$

i.e. the diagrammatic expression of the self-energy with respect to a generating functional in the sense of the Baym-Kadanoff perturbation theory. The last term of equation (7.4) is the double-counting correction (3.70), coming from those (unknown) diagrams that are already included in the LDA. In the second line of equation (7.3) we have two source terms: Σ, which is coupled to G, and V_{KS}, which is coupled to $n(\mathbf{r})$. As mentioned above, we have a mixed description in terms of the local Green's function G and the electron density $n(\mathbf{r})$. It is important to emphasize that these quantities are independent, in the sense that they cannot be

reconstructed from each other. Finally the term in the last line is equivalent to the last term of equation (7.1) with the addition of the self-energy. Note that with the expression $\chi^*\Sigma\chi$, we intend the local self-energy "upfolded" to the whole solid.

Besides the equation (7.4), we have three other stationary conditions to apply to $\Omega_{LDA+DMFT}$. By minimizing the functional (7.3) with respect to Σ we obtain again the Dyson equation (3.59). By minimizing it with respect to $n(\mathbf{r})$ we obtain the correct form of the Kohn-Sham potential, as above for DFT. The last minimization, with respect to V_{KS}, leads to the following electron density:

$$n(\mathbf{r}) = T \sum_{i\omega_n} \langle \mathbf{r} | \left[i\omega_n + \frac{\hbar^2}{2m}\nabla^2 - V_{KS}(\mathbf{r}) - \chi^*\Sigma(i\omega_n)\chi \right]^{-1} |\mathbf{r}\rangle. \qquad (7.5)$$

We see that the self-energy changes the electron density, but this effect is not considered in our implementation, as illustrated in Section 3.4.

By means of the previous relations, we can eliminate the source terms from the functional, which corresponds to make a Legendre transformation. This gives us the "physical" free energy functional

$$\Gamma_{LDA+DMFT}[G, n(\mathbf{r})] = \Omega_{LDA+DMFT}[\Sigma, G, V_{KS}(\mathbf{r}), n(\mathbf{r})], \qquad (7.6)$$

which in quantum field theory literature is usually referred as *effective action*, together with a factor β. In the zero-temperature limit we can obtain the following explicit expression for the total energy:

$$E = E_{LDA}[\rho(\mathbf{r})] - \sum_{\mathbf{k}\nu}' \varepsilon_{\mathbf{k}\nu} + \text{Tr}[\hat{H}_{LDA}\hat{G}] + \langle \hat{H}_U \rangle, \qquad (7.7)$$

where $\hat{H}_U$ indicates the two-particle term in the LDA+U Hamiltonian (2.28), and the primed sum is over the occupied states. We assume that the temperature effects can be taken into account only via summation over the Matsubara frequencies (included in the trace), and in the DFT part only weak temperature dependence via the Fermi distribution function is taken into account [140]. This corresponds to neglect the temperature dependence of the exchange-correlation potential and it is a standard procedure in electronic structure calculations of real materials. These effects are irrelevant for the cases under consideration where the main temperature dependence is due to spin fluctuations [28].

We notice that the total energy within the LDA+DMFT scheme is not simply the expectation value of the Hubbard term of the Hamiltonian (2.28), but consists of several terms, in analogy to the expressions (2.16) for the usual DFT. The first term $E_{LDA}[\rho(\mathbf{r})]$ contains the usual four different contributions, due to the external potential, the Hartree potential, the exchange-correlation potential and the sum of the Kohn-Sham eigenvalues. However in the spectral density functional theory the Kohn-Sham eigenvalues should be reoccupied with respect to the description

given by the total Green's function. Then we should remove the bare Kohn-Sham eigenvalues sum – second term of equation (7.7) – and substitute it with $\text{Tr}\,[\hat{H}_{LDA}\hat{G}]$ – third term. Moreover notice that $E_{LDA}\,[\rho(\mathbf{r})]$ depends only on the total electron density, so it does not need to be recalculated if the basic DMFT cycle is applied. In the case of the fully self-consistent cycle (see Figure 3.3), the calculation is straightforward, since it uses the same LDA-DFT machinery.

Finally we can evaluate $\langle\hat{H}_U\rangle$ through the so-called Galitskii-Migdal formula [141, 72], an elegant way to rewrite the expectation value of a two-particle operator in terms of a one-particle operator as the Green's function. This formula is based on the fact that for an Hamiltonian $\hat{H} = \hat{H}_0 + \hat{H}_U$, i.e. the same form of the Hamiltonian (2.28), the equation of motion of the Green's function states that

$$\langle\frac{\partial}{\partial\tau}\hat{G}(\tau)\rangle = \langle\hat{H}_0\rangle + 2\langle\hat{H}_U\rangle \tag{7.8}$$

where τ is the imaginary time for the finite temperature formalism (the formulation for real times and $T = 0$ is completely equivalent). Using the Fourier transform with respect to τ, we can move to the energy domain

$$\langle\frac{\partial}{\partial\tau}\hat{G}(\tau)\rangle = \text{Tr}\,[\omega\hat{G}(\omega)]\,. \tag{7.9}$$

Furthermore from the definition of the Green's function

$$[\omega\hat{\mathbf{1}} - \hat{H}_0 - \hat{\Sigma}(\omega)]\hat{G}(\omega) = \hat{\mathbf{1}}\,, \tag{7.10}$$

we can rewrite the expression above in terms of more manageable operators

$$\text{Tr}\,[\omega\hat{G}(\omega)] = \text{Tr}\,[\hat{\Sigma}(\omega)\hat{G}(\omega)] + \text{Tr}\,[\hat{H}_0\hat{G}(\omega)]\,. \tag{7.11}$$

Then the Galitskii-Migdal formula becomes

$$\langle\hat{H}_U\rangle = \frac{1}{2}\,\text{Tr}\,[\hat{\Sigma}\hat{G}]. \tag{7.12}$$

Notice that in our notation the self-energy involved in the calculation of $\langle\hat{H}_U\rangle$ has been already corrected with the double counting contribution through equation (3.83). This implies that no explicit double counting term for the total energy has been added in the functional (7.7), being already included in equation (7.12).

A final remark is needed about the role of the double counting term on the total energy in the LDA+DMFT scheme. Since the functional (7.7) depends on this *ansatz*, some of the previous implementations [25, 133] have a slightly different form than the one presented in this thesis. The reason is that those works address their studies to systems with stronger correlations ($U/W > 1$), and then use the correction (3.74). Conversely we are focused on transition metals which are described in an excellent way by equation (3.83), as it has been illustrated in the previous Chapters and in the cited references.

7.2   Implementation in FP-LMTO

We have implemented the total-energy algorithm presented in the previous Section into our LDA+DMFT code. A technical detail that becomes important in perspective of total-energy calculations is the computation of the number of electrons. In Chapter 3 the explicit expression of the number of particles in terms of the Green's function has been introduced by means of equation (3.68). For clarity we repeat it here:

$$N = T \sum_{i\omega_n} \sum_{\mathbf{k}} \sum_{\chi_1,\chi_2} S(\mathbf{k})_{\chi_2,\chi_1} G(\mathbf{k}, i\omega_n)_{\chi_1,\chi_2} \, .$$

We have also mentioned the problem of considering the long decaying tails of the Green's function (3.59) without increasing too much the number of Matsubara frequencies. While the calculation of the spectral properties is not very sensitive to the number of electrons, or equivalently to the chemical potential, the evaluation of the total-energy for equilibrium atomic volume and bulk modulus requires a high precision. If we intend to evaluate more subtle properties as magneto-crystalline anisotropy the needed precision increases further.

In our implementation we basically follow the elegant procedure used in the LDA+DMFT calculations of Refs. [15, 133] and adapted to our non-orthonormal basis set. The idea is to decompose the calculated Green's function (3.60) as

$$G(\mathbf{k}, i\omega_n)_{\chi_1,\chi_2} = G(\mathbf{k}, i\omega_n)^{num}_{\chi_1,\chi_2} + G(\mathbf{k}, i\omega_n)^{an}_{\chi_1,\chi_2}, \tag{7.13}$$

where $G(\mathbf{k}, i\omega_n)^{an}_{\chi_1,\chi_2}$ is a analytical function that we choose to fit the high-frequency behavior of $G(\mathbf{k}, i\omega_n)_{\chi_1,\chi_2}$:

$$\sum_{i\omega_n}^{(\omega_n > \omega_{max})} \left[G(\mathbf{k}, i\omega_n)_{\chi_1,\chi_2} - G(\mathbf{k}, i\omega_n)^{an}_{\chi_1,\chi_2} \right] = 0. \tag{7.14}$$

On the other hand the numerical part is defined as the difference between the calculated function and the analytical function

$$G(\mathbf{k}, i\omega_n)^{num}_{\chi_1,\chi_2} \equiv G(\mathbf{k}, i\omega_n)_{\chi_1,\chi_2} - G(\mathbf{k}, i\omega_n)^{an}_{\chi_1,\chi_2}, \tag{7.15}$$

and, if $G(\mathbf{k}, i\omega_n)^{an}_{\chi_1,\chi_2}$ has been chosen wisely, is negligible for $\omega_n > \omega_{max}$.

The new problem is to determine G^{an}. Starting from the definition (3.59), we can rewrite the matrix element (3.60) as

$$G(\mathbf{k}, i\omega_n)_{\chi_1,\chi_2} = \left\langle \mathbf{k}, \chi_1 \left| \left[i\omega_n - \hat{A}_{\mathbf{k}}(i\omega_n) \right]^{-1} \right| \mathbf{k}, \chi_2 \right\rangle \tag{7.16}$$

where we have defined the new operator

$$\hat{A}_{\mathbf{k}}(i\omega_n) \equiv \mu \hat{\mathbf{1}} - \hat{h}_{LDA} - \hat{\Sigma}(i\omega_n) \, . \tag{7.17}$$

Now let us consider $\hat{\Sigma}(i\omega_n) = 0$ corresponding to the first iteration of the LDA+DMFT cycle. In this case the operator (7.17) does not depend on the Matsubara frequencies and is Hermitian; consequently it has real eigenvalues $\lambda_m^{\mathbf{k}}$ and the eigenvectors $|X_m^{\mathbf{k}}\rangle$ can be chosen to form an orthonormal set. By expanding $\hat{A}_{\mathbf{k}}(i\omega_n)$ in its spectral representation, the equation (7.13) becomes

$$G(\mathbf{k}, i\omega_n)_{\chi_1,\chi_2} = G(\mathbf{k}, i\omega_n)_{\chi_1,\chi_2}^{num} + \sum_m \frac{\langle \mathbf{k}, \chi_1 | X_m^{\mathbf{k}} \rangle \langle X_m^{\mathbf{k}} | \mathbf{k}, \chi_2 \rangle}{i\omega_n - \lambda_m^{\mathbf{k}}}. \tag{7.18}$$

We have finally reduced the original sum to two terms that we can calculate with high precision. The numerical term is simply calculated as a sum for positive frequencies up to ω_{max}. The sum for negative frequencies is obtained using the symmetry of the Green's function

$$G(\mathbf{k}, -i\omega_n)_{\chi_1,\chi_2} = [G(-\mathbf{k}, i\omega_n)_{\chi_2,\chi_1}]^* \tag{7.19}$$

The analytical term can be summed through standard many-body techniques:

$$\sum_{i\omega_n} \sum_m \frac{\langle \mathbf{k}, \chi_1 | X_m^{\mathbf{k}} \rangle \langle X_m^{\mathbf{k}} | \mathbf{k}, \chi_2 \rangle}{i\omega_n - \lambda_m^{\mathbf{k}}} = \sum_m \frac{\langle \mathbf{k}, \chi_1 | X_m^{\mathbf{k}} \rangle \langle X_m^{\mathbf{k}} | \mathbf{k}, \chi_2 \rangle}{1 + e^{\beta \lambda_m^{\mathbf{k}}}}. \tag{7.20}$$

In comparison with Ref. [133] finding eigenvalues and eigenvectors of $\hat{A}_{\mathbf{k}}$ is slightly more cumbersome here: due to the non-orthonormality of the basis set we have to solve a generalized eigenvalue problem. However using the fact that the overlap matrix is positive definite, through Cholesky decomposition [142] of S the problem can be reduced to a usual eigenvalue problem through a few algebraic operations.

When the DMFT self-energy assumes finite values, the operator $\hat{A}_{\mathbf{k}}(i\omega_n)$ is different at every Matsubara frequency, and then we need to use some approximation. Luckily in many-body theory the analytical properties of the self-energy operator are the same as for the Green's function. Therefore we can assume the following asymptotic behavior for high frequencies [133]:

$$\hat{\Sigma}(i\omega_n) \sim \hat{\Sigma}^{stat} + \frac{\hat{\Sigma}^{asym}}{i\omega}, \tag{7.21}$$

where $\hat{\Sigma}^{stat}$ and $\hat{\Sigma}^{asym}$ are obtained from the real and imaginary part of $\hat{\Sigma}$ at the cut-off value ω_{max}. While a higher ω_{max} will always give a better fit, the real part of the self-energy converges to $\hat{\Sigma}^{stat}$ as $1/\omega^2$, and then we do not need a very high cut-off. Furthermore for our purposes of evaluating the frequency sum in equation (3.68), we can keep only the dominant term $\hat{\Sigma}^{stat}$, and $\hat{\Sigma}^{asym}$ turns to be unimportant. Again the operator (7.17) becomes Hermitian and independent on the Matsubara frequencies, so that the same procedure described above can be applied.

The implementation of this algorithm in the FP-LMTO code has proved to give very good results. The method used for the calculations of the spectral functions of Chapters 4 and 5 is based on similar assumptions, but has much simpler implementation. Instead of considering the asymptotic behavior of every Green's function in equation (3.68), the sum over the intermediate indices χ_1,χ_2 and $\mathbf{k}$ was done, and then the asymptotic behavior of the resulting function was considered. While this approximation can appear too crude, the precision on the number of particles is about 10^{-3} particles for every electron involved in the problem. On the other hand it was computationally very efficient, since the generalized eigenvalue problem was reduced to the determination of a pure number. Moreover we can also explain the reason behind the mysterious term $1/2$, found in some of the previous LDA+DMFT implementations. In all the expressions above the asymptotic behavior of the Green's function can be described in first approximation by considering $\lambda_m^{\mathbf{k}} = 0$. With this assumption the sum over m at the right hand side of equation (7.20) can be trivially removed, leading to the term $1/2$.

After having improved the precision in the determination of the number of particles, we can pass to the implementation of the total energy formula (7.7). As we have already seen the first two terms can be obtained from the density-functional part of the LDA+DMFT scheme. The third term, corresponding to the reoccupation of the Kohn-Sham orbitals, requires again the evaluation of a sum over all the Matsubara frequencies

$$\text{Tr}\,[\hat{H}_{LDA}\hat{G}] = T \sum_{i\omega_n} \sum_{\mathbf{k}} \sum_{\chi_1,\chi_2} H_{LDA}(\mathbf{k})_{\chi_2,\chi_1} G(\mathbf{k},i\omega_n)_{\chi_1,\chi_2}. \tag{7.22}$$

Besides the presence of different matrix elements, equation (7.22) is completely analogous to equation (3.68), therefore the sum can be done by applying the same procedure used above. Finally we have to evaluate the Galitskii-Migdal contribution $\langle \hat{H}_U \rangle$. Given that in the LDA+DMFT scheme the self-energy is local, the trace in equation (7.12) can be restricted to the correlated orbitals. Furthermore, using the fact that in the SPTF solver we work with quantities in both the frequency and (imaginary) time domains, we can express the trace in terms of the complex Fourier transforms. For this purpose, it is most convenient to separate the static and the dynamic parts of the self-energy. Analogously to equation (7.21), we have

$$\hat{\Sigma}(i\omega_n) = \hat{\Sigma}^{stat} + \hat{\Sigma}(i\omega_n)^{dyn} . \tag{7.23}$$

However now no fitting is necessary: once $\hat{\Sigma}^{stat}$ is determined, $\hat{\Sigma}(i\omega_n)^{dyn}$ contains all the differences with the calculated function $\hat{\Sigma}(i\omega_n)$. We can then write

$$\langle \hat{H}_U \rangle = \frac{1}{2} T \sum_{i\omega_n} \sum_{\xi_1,\xi_2} [\Sigma^{stat}_{\xi_1,\xi_2} + \Sigma(i\omega_n)^{dyn}_{\xi_1,\xi_2}] G(i\omega_n)_{\xi_2,\xi_1}. \tag{7.24}$$

The first term at right hand side can be easily Fourier transformed and reduced in terms of occupations of the local orbitals

$$n_{\xi_1,\xi_2} = G(\tau = 0^-)_{\xi_1,\xi_2};\tag{7.25}$$

the second term requires the evaluation of the Fourier transform of a product, leading to a convolution. In summary we can express equation (7.24) as

$$\langle \hat{H}_U \rangle = \frac{1}{2} \sum_{\xi_1,\xi_2} \left[\Sigma_{\xi_1,\xi_2}^{stat} n_{\xi_2,\xi_1} + \int_0^\beta d\tau\, \Sigma(\tau)_{\xi_1,\xi_2}^{dyn} G(-\tau)_{\xi_2,\xi_1} \right].\tag{7.26}$$

7.3 Comparison with FP-KKR

The same total energy algorithm of the previous Sections was implemented in the FP-KKR code described in Ref. [103], being an extension to the full-potential case of the earlier ASA implementation [36]. This is one of the very few fully self-consistent implementations of the LDA+DMFT scheme, and several successfull studies based on it have been published. Among them we mention the study of the orbital polarizations of the transition metals [103], the photoemission spectrum of fcc Ni within the one-step model [29], and the magnetism of Co-Pt solid-state systems through coherent potential approximation (CPA) [143].

Comparing the results of FP-KKR and FP-LMTO calculations we can analyze two important points. First of all we can check the role of the full self-consistent cycle on the ground-state properties. In second place we can address the question about sensitivity of the LDA+DMFT description to the band structure method used. This is nontrivial since different methods use different basis sets which are truncated in any real calculations. An important premise to this comparison is that the correlated orbitals used in both codes must be reasonably similar, and that the same solver is used. These requirements are well satisfied, and can be verified in the good agreement between the quasiparticle spectra of Fe, Co, Ni and Mn calculated with the SPTF solver.

A survey of the equations involved in the FP-KKR method is out of the scope of this thesis, and we redirect the reader to Ref. [144] for a comprehensive description. The only difference that must be emphasized is that for FP-KKR in the equation (7.7) the functional $E_{LDA}[\rho(\mathbf{r})]$ is evaluated with the LDA+DMFT electron density. The latter one is determined solving a Dirac equation which comprehends the Kohn-Sham potential and the self-energy.

7.4 fcc Ni

Bulk fcc Ni is a sort of standard test-case for every approach to strongly correlated materials. For this reason it has been chosen as first application for the implemen-

tations presented above. The interest of the DMFT community in Ni started [28] with the explanation of the famous 6 eV satellite observed in photoemission experiments, but missing in all DFT calculations. Afterwards many other studies have been addressed to its spectral properties through LDA+DMFT [78, 77, 29] and also through GW+DMFT [145]. Along with these spectral features, the LDA+DMFT method has been applied to the finite-temperature magnetism [28] of Ni, showing the existence of local moments (unordered above the Curie temperature), i.e. another clear sign of strong correlation. Nevertheless we should consider that the DFT scheme is not focused on the excitation spectrum, but mainly on the electron density. Given the the LDA+DMFT scheme and the Hamiltonian (2.28) are explicitly build for the correct description of the low-energy excitations, it appears natural that this scheme performs convincingly better than simple density functional theory. Conversely DFT gives a reasonable description of all ground state properties of Ni and the agreement with the experimental data becomes almost perfect if GGA is used [146, 147, 148]. Moreover, in contrast with the other late transition metals, the inclusion of the spin polarization in the calculations for fcc Ni is not strictly necessary, surely due to the small magnetic moment ($\mu \simeq 0.6$) acquired [147] at the equilibrium structure. Finally, a recent accurate study of the orbital and spin polarization of the late transition metals [103] emphasized that the DMFT corrections to the DFT-LDA values for Ni are really minor, while still improving the description of the material.

With reference to the previous arguments, it appears necessary to clarify the reasons behind our interest in the energetics of fcc Ni, where the correlation effects are expected to have a moderate role. First of all it is important to complete the picture outlined above: excitation spectrum, magnetism, photoemission spectrum, surfaces, orbital polarization and now ground state properties. This study can help in understanding how correlated fcc Ni is [5] and which deficiencies of the DFT-LDA technique are due to a single-particle approximation of the exchange-correlation potential and which ones are due to the intrinsic meaning of the Kohn-Sham quasiparticles as fictitious excitations. In second place Ni represents a good test-case to prove the ability of the LDA+DMFT scheme to catch moderate correlation effects in a real material. In fact we know that the LDA+DMFT scheme relies mainly on two different approximations: finite number of nearest neighbors (due to the locality of the self-energy) and non-exact solver. Therefore it is interesting to check how dominant are the errors connected to these approximations for effects that are expected to be rather small. Furthermore a third important question concerns the role of the full self-consistency in the DMFT cycle. Previous studies [133] for Ce_2O_3 and γ-Ce have shown, quite surprisingly, small differences between the ground state properties for the basic and fully self-consistent DMFT cycles. Given that these systems involve valence electrons much more localized than the ones of Ni, in our case we expect negligible differences, at least in the
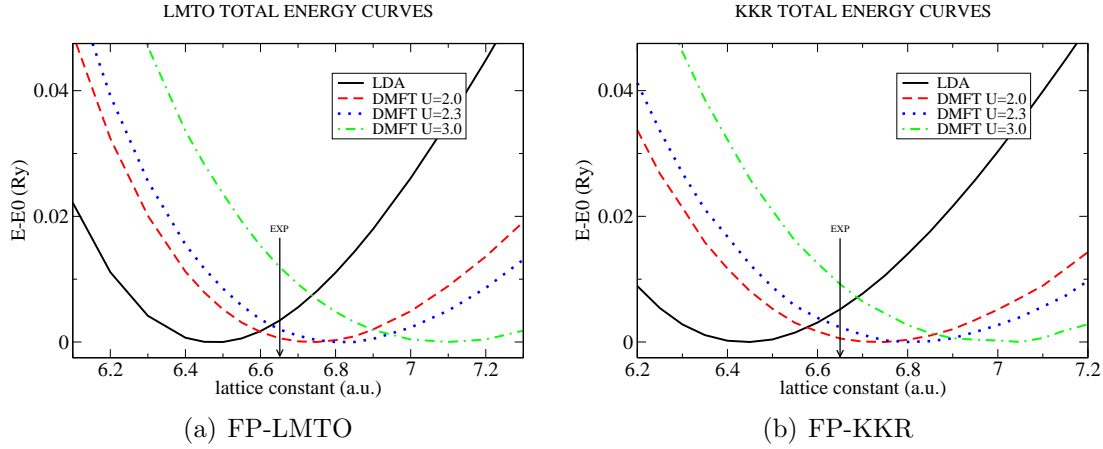
Figure 7.1: Energy vs lattice constant curves for fcc Ni in DFT-LDA and in the LDA+DMFT scheme based on the FP-LMTO (left) and FP-KKR method (right). The zero of the energy of each curve is set to its own minimum value E_0 and three chosen values of U are presented ($T = 400$ K). The experimental value of the lattice constant is indicated by the arrow.

range of "acceptable" Hubbard U. Finally, a last question investigated for fcc Ni concerns the compatibility between different implementations: can different codes with different choices of the correlated orbitals give comparable results?

To investigate all the various points outlined in the previous paragraph, we performed LDA+DMFT simulations of fcc Ni for various lattice constants starting from $a = 6.2$ a.u. and up to $a = 7.4$ a.u.. We treated $3d$, $4s$ and $4p$ electrons as valence electrons. For the FP-LMTO simulations, the description of the valence electrons in the interstitial space between the muffin tin spheres requires LMT-Orbitals with different tail energies, whose number depends on the degree of localization-delocalization of the electrons: three tails were used for $4s$ and $4p$ electrons, only two tails for $3d$ electrons. The subset MT of correlated orbitals has been used. Convergence on the total energy with respect to the **k**-mesh lead to a minimum number of 4913 **k**-points used in the three dimensional Brillouin zone. A simulation has been considered converged if the energy difference for two consecutive iterations has been at least smaller than 0.1 meV. As far as possible same settings were used for the FP-KKR simulations and also the set of correlated orbitals have been chosen to be as similar as possible to the MT correlated subset. In addition KKR total energies are very sensitive to the angular momentum expansion used for calculation. To get accurate results we performed LDA numerical tests up to $l_{max} = 6$. We found that in the case of Ni and Mn converged results require at least angular momentum expansion up to $l_{max} = 3$. This cut-off was used for the more computationally demanding LDA+DMFT calculations.

The local problem was studied for different values of U in the range between 2 and 3 eV, considered acceptable from the results of constrained LDA calculations

Table 7.1: Computed values of the equilibrium atomic volume V_0 and the bulk modulus B for the the standard LDA-DFT method and for the LDA+DMFT scheme. Different strengths of the local Coulomb repulsion U (in eV) have been studied, at $T = 400$K. The values taken from Ref. [147] are obtained by means of an ASA-LMTO code.

		LDA	$U = 2.0$	$U = 2.3$	$U = 3.0$	GGA	EXP
	FP-LMTO	67.88	76.20	79.19	89.48		
V_0(a.u.^{3})	KKR	66.86	76.28	79.02	85.53		73.52
	Ref. [147]	67.71				76.54	
	FP-LMTO	260	163	142	84		
B(GPa)	KKR	280	171	150	132		186
	Ref. [147]	270				186	

[69, 149] and previous LDA+DMFT simulations (see Section 4.2). The temperature was set as $T = 400$ K and 2048 Matsubara frequencies were used. As for the DFT part, convergence in the LDA+DMFT total energy was considered acceptable when the changes for subsequent iterations were smaller than 0.1 meV. In Figure 7.1(a), we can see the total energy curves as functions of the lattice constant for the FP-LMTO implementation. The curves have been shifted with respect to their minima, so it is easier to compare them. As observed in previous calculations [147], in DFT-LDA the equilibrium value of the lattice constant is slightly (3%) underestimated with respect to the experimental one. Looking at the curves for the LDA+DMFT simulations, we immediately notice that the results are strongly dependent on the value of the Hubbard U. Furthermore the best result seems to be obtained for $U = 2$ eV, i.e. for a value smaller than the widely accepted $U = 3$ eV. On the other hand the curve for $U = 3$ eV seems to comprehend too strong correlation effects. The explanation of these results is in the perturbative nature of the SPTF solver, which tends to overestimate correlation effects in fcc Ni. This was noticed since the first implementation [78], when comparison between LDA+DMFT results with SPTF solver and numerically exact quantum Monte-Carlo solver showed the best agreement for $U = 2$ eV. Further in the already mentioned calculation of the orbital polarization of Ni, it is shown that SPTF with $U = 3$ eV gives too strong correction of the orbital moment [103].

On the other hand we could be tempted to think that this behavior is increased by the lack of full self-consistency in the LDA+DMFT cycle. This doubt is removed by looking at the results for KKR, reported in Figure 7.1(b). In fact we can barely notice any difference with respect to the energy curves of the FP-LMTO. It is important to emphasize how similar the presented results are, since the arbitrariness of the LDA+U Hamiltonian (2.28), due to the arbitrary choice of the

correlated orbitals, is often considered as a limit of orbital-dependent methods.

Table 7.1, where the equilibrium atomic volume V_0 and the bulk modulus B are given, allows a more quantitative comparison of the two implementations and with previous DFT-LDA studies of fcc Ni [147]. These values of V_0 and B have been computed with polynomial fitting of the energy versus atomic volume curve around the minimum. In addition also fitting through Birch-Murnaghan equation of state [150, 151] was done, leading to almost identical results and confirming the stability of our data.

As for the total energy curves, the best results are obtained for $U = 2$ eV, and we can see that the inclusion of local correlation effects into the LDA results corrects both the equilibrium atomic volume and the bulk modulus in the right way. While this fact has enough interest by its own, we should notice that to have more precise results on the quantitative point of view, a more strict relation between solver, correlated orbitals and values of U is needed. Naturally it would be interesting to repeat those calculations with the numerically exact quantum Monte-Carlo solver to check if better agreement with the experiment can be obtained. Another interesting property can be deducted from the Table 7.1: while the equilibrium atomic volumes are independent on the full self-consistency, the bulk modulus looks to be more strongly influenced. As expected this discrepancy is proportional to the strength of U. The simulation for the strongest value tried, i.e. $U = 3$ eV, shows the tendency of the FP-LMTO to underestimate the value of the bulk modulus of fcc Ni.

7.5 γ-Mn

Mn is definitely one of the most interesting and complex materials among pure transition metals. According to Hund's rule, free atom possesses a large magnetic moment of $5\mu_B$, and the stabilization of such large magnetic moments, e.g. in Heusler alloys, would represent a great technological advance, suitable for many applications.

Experimentally Mn exists in four different phases. The low-temperature low-pressure phase is the α-phase [152]. It has a complex cubic structure with 58 atoms per unit cell and non-collinear antiferromagnetic order. The local moment depends strongly on the atomic site, varying between $3\mu_B$ and 0, and disappears above the Neél temperature $T_N = 95$ K. At $T = 1073$ K there is a transition to the β-phase [153], a cubic structure with 20 atoms per unit cell and small magnetic moment. Between $T = 1368$ K and $T = 1406$ K a high-temperature γ-phase with fcc structure appears. Interestingly this phase can be stabilized until room temperature through the addition of a small amount of impurities [154] or as layer-by-layer deposition on $Cu_3Au(100)$ [155, 116]. Below the Neél temperature, about $T_N = 540$ K the γ-phase acquires an anti-ferromagnetic ground-state, which

is accompanied by tetragonal distortion into the fct structure [155, 156]. From $T = 1406$ K up to the melting temperature $T_M = 1517$ K there is a δ-phase, whose structure is bcc and order is antiferromagnetic. Finally high-pressure studies have revealed a transition to an hcp ϵ-phase [157] at 165 GPa.

Such a rich phase diagram corresponds to an equivalently rich history of theoretical studies (for an extended review we redirect the reader to the Ref. [137]). Obviously these studies have been mainly focused on the two "simplest" phases, γ and δ, while the increase of the computational power achieved in the last ten years made the first *ab-initio* calculations of α and β phases appear [158, 159, 160].

Our main interest concerns the ground-state properties of γ-Mn and the role of correlation effects. The description of the electronic properties given by density-functional theory is undoubtedly wrong for non spin-polarized LDA, but it becomes more reasonable if spin-polarization is introduced [161, 135]. As for Fe, however, LSDA does not predict the correct crystal structure, but the ground-state of Mn results to be hcp [162]. Furthermore these strong magneto-volume effects are reflected into an anomalously low value of the bulk modulus [135]. This can be considered as a first hint to strong correlation effects. Like for the other transition metals, the agreement of the calculated ground-state properties with the experimental data improves drastically if spin-polarized GGA is used as exchange-correlation potential [136, 137], but the discrepancies are still the strongest of the $3d$ series. Furthermore, as already pointed out by Zein [138], the anomalous properties of Mn do not seem to depend so strongly on the magnetic phase. In fact extrapolation of experimental data for Mn-Cu alloys to zero content of Cu shows [163] equilibrium atomic volume and bulk modulus comparable (in a range of 10%) to pure γ-Mn, while doping by Cu suppresses antiferromagnetism in γ-Mn. The situation becomes still worse if spectral properties are considered. The only LDA+DMFT study available on γ-Mn has shown [116] that inclusion of local Coulomb interactions is necessary for a proper description of the excitations. Following this work, γ-Mn seems to behave more as a strongly correlated metal at the metallic side of Mott metal-insulator transition, than as a moderately correlated metal with some deficiencies in the spectrum, as Ni: Hubbard bands are formed for high energies and a quasiparticle resonance appears around the Fermi level. To clarify the role of correlations and the connection between correlations and magnetism in γ-Mn we have carried out systematic LDA+DMFT simulations. We have adopted a simple fcc crystal structure in a layered antiferromagnetic phase AFM1, since previous simulations showed clearly this to be the equilibrium structure [164, 136, 137]. As already deduced in the early eighties [156], the frustration of the AFM1 fcc structure should imply a slight (6%) distortion of the lattice, but this effect has not been considered here, since its role is not so important in comparison to local Coulomb interactions. The relation between correlation effects, frustration and lattice distortion will be the subject of future investigations. The

lattice constants have been ranged from $a = 6.0$ a.u. and up to $a = 7.5$ a.u.. All the other computational details have been set as the ones used for Ni.

The choice of the Hubbard U for Mn is not trivial at all, since this element was not studied as much as Ni. In the previous LDA+DMFT study [116] it was varied between 3 eV and 5 eV through semi-empirical considerations. However, recent progress has been made on the implementation of procedures to determine the parameters describing the local Coulomb interactions *ab initio*. New results for the $3d$ transition metals have been obtained using the "canonical" constrained local density approximation [165] and the "new" constrained random-phase approximation [65, 166] and they locate U in the range $2 - 4$ eV for the whole series, reaching maximum values for the half-filled systems. Given that one of these simulation used a basis set very similar to ours (MT correlated subset) [166], for γ-Mn we adopted $U = 2.6$ eV and $U = 3.0$ eV. The corresponding Hund's exchange was chosen as, respectively, $J = 0.8$ eV and $J = 0.9$ eV.

In Figure 7.2 the total energy curves as functions of the lattice constant for the FP-LMTO implementation are given. As for Ni, the curves have been shifted with respect to their minima to obtain a better visualization. From Figure 7.2, we immediately notice two interesting features in the LDA+DMFT total energy curves. First of all we can notice that, by increasing the value of U from zero to the accepted effective value, the minima of the total energy curves of the LDA+DMFT simulations gradually tend to the experimental lattice constant. Furthermore the dependency of the results from the strength of U, which have been already observed for Ni, looks still bigger and we consider it as good indication for strong correlations. This impression is emphasized by another interesting feature noticeable from Figure 7.2: the total energy curves do not appear to have a perfect parabolic shape as for usual LDA or GGA simulations, or also for the LDA+DMFT simulations of Ni depicted in Figure 7.1. Instead they show a small kink for lattice constants around 6.6 a.u.. To make it more visible, in the inset of Figure 7.2 the calculated data for $U = 2.6$ eV are compared with a standard fitting through Birch-Murnaghan equation of state. This kink is a clear sign of the strongly correlated character of $γ$ Mn and reminds the one found in LDA+DMFT total energy curves of $δ$-plutonium [19]. In the latter case, there is more than just kink, there is a second minimum of the total energy which was associated with the volume of monoclinic $α$ phase. For Mn, there is no phase transitions with large volume jumps, like for Pu, but, instead, anomalies of the bulk modulus in Mn-based alloys are observed [163]. It is important therefore to analyze the origin of this kink. In Figure 7.3 magnetic moments and Galitskii-Migdal contributions to the total energy functional are shown. We can see that the value of the lattice constant corresponding to our kink is a bit higher than the critical value for which the non-zero magnetic moment appears. At the onset of the magnetism, the competition with the local Coulomb interactions brings a saturation of the Galitskii-Migdal
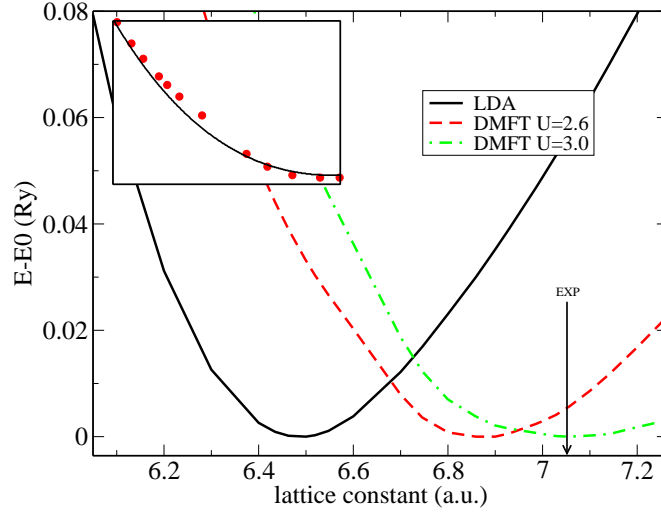
Figure 7.2: Energy versus lattice constant curves for γ-Mn in the DFT-LDA scheme and in the LDA+DMFT scheme based on the FP-LMTO method. The zero of the energy of each curve is set to its own minimum value E_0 and two chosen values of U are presented ($T = 400$ K). The lattice constant that corresponds to the experimental atomic volume is indicated by the arrow. In the inset we can observe the total energy for LDA+DMFT simulation at $U = 2.6$ eV (big points) as function of the atomic volume compared to the standard Birch-Murnaghan equation of state (solid line).
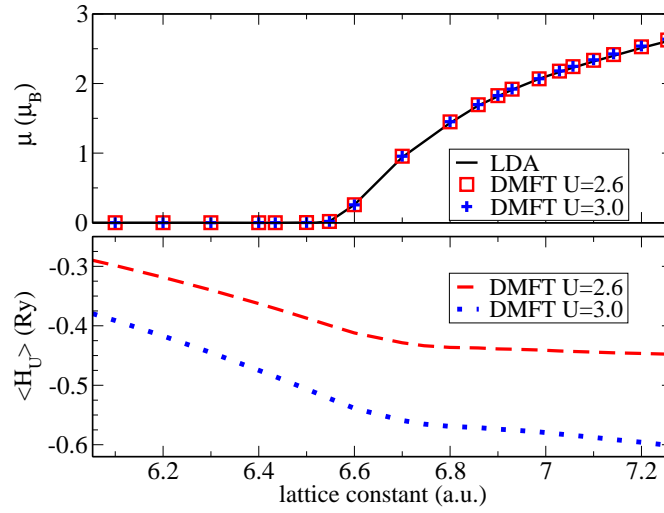
Figure 7.3: Local magnetic moment μ and Galitskii-Migdal contribution to the total energy $< \hat{H}_U >$ as function of the lattice constant for γ-Mn. While it is not observable from the picture the magnetic moment of the LDA+DMFT simulation is increased with respect to its bare LDA value. For $U = 2.6$ eV the increase in the magnetic moment is about $0.02\,\mu_B$, while for $U = 3.0$ eV it is about $0.03\,\mu_B$. Interestingly no magnetic moment is created if the starting Kohn-Sham densities is non-magnetic.

Table 7.2: Computed values of the equilibrium atomic volume V_0, the bulk modulus B and magnetic moment μ of γ-Mn for LDA-DFT and for LDA+DMFT. Different strengths of the local Coulomb repulsion U (in eV) have been studied, at $T = 400K$. The values taken from Ref. [136] are obtained by means of a USPP-PAW (ultrasoft pseudopotential projector augmented plane-wave) code, and using the Murnaghan equation of state [150, 151]. The experimental values for the atomic volume and the magnetic moment come from Refs. [154, 167], and are obtained as extrapolation to room temperature of high temperature data. The values of the bulk modulus are more uncertain and come from Refs. [168, 135].

		LDA	$U = 2.6$	$U = 3.0$	GGA	EXP
$V_0(\text{a.u.}^3)$	FP-LMTO	69.18	81.17	88.61		$87.30 \div 87.60$
	Ref. [136]	68.36			82.32	
$B(\text{GPa})$	FP-LMTO	313	213	88		$90 \div 130$
	Ref. [136]	310			95	
$\mu(\mu_B)$	FP-LMTO	0.00	1.74	2.30		2.30
	Ref. [136]	0.00			2.40	

energy, which otherwise would be expected to decrease with the atomic volume (as for example we observe for Ni). Instead of decreasing the correlation energy, the system responds with an increase of the magnetic moment with respect to the bare LDA value. This change is so small that it can be barely noticed in the upper plot of Figure 7.3. For $U = 2.6$ eV the increase of the magnetic moment is about $0.02\,\mu_B$, while for $U = 3.0$ eV it is about $0.03\,\mu_B$.

Given that the FP-LMTO is numerically less expensive than FP-KKR, we have made extensive calculations for γ-Mn only using the former method. A few simulations have been made with the FP-KKR method and the same qualitative features reported in Figures 7.2 and 7.3 have been observed, stating again that for the description of the ground state properties of $3d$ transition metals the inclusion of local correlation effects on the electron density $n(\mathbf{r})$ is not strictly necessary.

A more clear picture of the physical properties of γ-Mn can be obtained from the Table 7.2, where equilibrium atomic volume V_0, bulk modulus B and magnetic moment μ for our simulations have been compared to the experimental values and to the results reported in Ref. [136].

Consistently with previous calculations, the LDA fails for γ-Mn and the differences with the experimental data are much stronger than for the other transition metals, e.g. Ni presented above. The atomic volume is underestimated and the bulk modulus is heavily overestimated. Moreover for γ-Mn the change of the exchange-correlation potential from LDA to GGA does not solve all the problems, and still there is an important difference between theory and experiments. Does the LDA+DMFT scheme give a better description? The simulation for the weak-

est U seems to underestimate the local Coulomb interaction. The corrections of equilibrium atomic volume, bulk modulus and magnetic moment are good, but they are too small to reproduce the experimental data. On the other hand the simulation for the strongest U is in perfect agreement with the reported values. Nevertheless we must notice that the quantitative difference of the bulk modulus between the two LDA+DMFT simulations is surprisingly big. From the comparison with FP-KKR data, and also looking to the results for Ni, we see that our value is slightly underestimated because of the use of the basic DMFT cycle, but we can exclude that this effect comprehend the whole variation of B. We identify this sensitivity of B to U as another sign of strong correlations.

The reliability of the solver used in the presented calculations has been checked carefully. In fact the SPTF solver (Section 3.6) is a perturbative approach to the Anderson impurity model, and its application is restricted to systems where the Hubbard U is not bigger than the bandwidth. In this sense γ-Mn is a system at the border of applicability range, so that a deep investigation of the behavior of SPTF has been necessary. Given that the localization of the $3d$ electrons depends on the atomic volumes, we could expect our approximations to fail for big lattice constants. We surely exclude this problem since we verified that this happens only far away from the range of atomic volumes we were interested in. Another problem we could exclude was the fact that our approximations could simply collapse for all the atomic volumes driven by the strength of U. In fact we have studied intermediate values of U between $U = 2.6$ eV and $U = 3.0$ eV and all the physical properties have shown a regular behavior, including the bulk modulus B.

While we focused our analysis mainly on the anti-ferromagnetic phase, we tried to get more insight into the role of magnetism in γ-Mn through LDA+DMFT simulations of the non-magnetic phase. The results are quite interesting: the energy versus lattice constant curve (not shown here) has a regular parabolic shape with an equilibrium atomic volume $V_0 = 85.91$ a.u.^{3}, intermediate to the equilibrium atomic volume of the LDA+DMFT simulation for the antiferromagnetic phase. Obviously this is a consequence of the constrained zero magnetic moment, and no quenching of the Galitskii-Migdal energy can appear. The increasing strength of the correlation energy is observable also in a huge drop of the bulk modulus with respect to its bare LDA value: $B = 57$ GPa, perfectly consistent with the already mentioned experimental data for γ-MnCu alloys [163], after extrapolation to zero content of Cu at room temperature. As before we have checked whether the SPTF solver is applicable or not to our system. We have found that our approximations lose validity for atomic volumes larger than 100 a.u.^{3}: the localization effects are heavily overestimated and the crystal tends to collapse into an atomistic system. This threshold is well above the equilibrium values, so that we can consider our results as reliable. The role of the solver in the description of the magnetic fluctuations in non-magnetic Mn is the main subject of the next Chapter.

Chapter 8

γ-Mn at the border between weak and strong correlations

In Section 7.5 we have briefly discussed the dependence of the ground-state properties of γ-Mn on the equilibrium magnetic structure. In principle the initial magnetic ground-state should not have a main role in the LDA+DMFT scheme, provided that the single impurity effective model is solved exactly. However for a series of different reasons[1] sometimes it can be more convenient to employ approximate solvers, as the SPTF presented in Section 3.6. SPTF is a perturbative solver, which restricts its use to relatively weakly, or moderately, correlated systems. Not surprisingly, SPTF performs well when starting from a spin-polarized solution, since the spin-splitting contains already the main part of the exchange and correlation effects. Conversely, the direct application of SPTF to a non-magnetic phase can create stability problems since we are trying, in such case, to attribute strong, and essentially mean-field, effect of formation of local magnetic moment to dynamical fluctuations around non-spin-polarized case. As a way to weaken such a limitation we propose a combination of SPTF with the disordered local moment (DLM) approach [169, 170]. As already shown for the case of actinides [171] the inclusion of the fluctuations of randomly oriented local moments can improve drastically the description of energetics in the paramagnetic phase. One can hope therefore that it allows us to extend the range of applicability of SPTF.

In the present Chapter the proposed DLM+SPTF method is applied to the spectral properties of γ-Mn, and a comparison is presented with numerically exact QMC solver. The results appear to be strongly dependent on the formation of local moments, which is driven by the Hund's exchange. For realistic values of the Coulomb interaction γ-Mn is shown to be a material right at the border between weak and strong correlations.

---

[1]We will come back to this point at the end of Section 8.1.

The present Chapter is based on the following publication:

1. I. Di Marco, J. Minár, J. Braun, M. I. Katsnelson, H. Ebert, A. I. Lichtenstein, O. Eriksson, "γ-Mn at the border between weak and strong correlations", *submitted to Eur. Phys. Lett.*

8.1   Quantum Monte-Carlo solver

To analyze the different regimes of correlations in paramagnetic γ-Mn we have implemented the numerically exact QMC solver in our LDA+DMFT code. In general the QMC solvers can be divided into two big families: the Hirsch-Fye [172, 14] and the continuous-time [94, 95] QMC methods. Our implementation is based on the first algorithm, which we are going to refer simply as QMC in the rest of the Chapter.

The purpose of QMC is to calculate the local Green's function associated to the effective impurity model of Hamiltonian (2.38). The basic procedure consists in evaluating the average in equation (2.47) by means of the impurity action (2.46). The transformation of the quantum-mechanical problem into a numerical problem requires a few well-defined steps, which are going to be presented for a one-orbital model. Consequently we keep the notation as simple as possible, and we remind that generalization to multi-orbital case is straightforward, implying only additional matrix indices [173].

For sake of illustration, it is useful to associate an Hamiltonian K to the bath Green's function $\mathcal{G}_0(\tau)$, and to consider an interaction term with the following form:

$$H_{int} = U\left(n_\uparrow - \frac{1}{2}\right)\left(n_\downarrow - \frac{1}{2}\right). \tag{8.1}$$

Our first aim is the evaluation of the partition function Z, which has an important role in QMC. We proceed with the discretization of the imaginary time interval $\big[0, \beta\big]$ in L slices of length $\Delta\tau$, so that we can write

$$Z = \operatorname{Tr} e^{-\beta H} = \operatorname{Tr} \prod_{l=1}^{L} e^{-\Delta\tau H}. \tag{8.2}$$

Now we need to deal with the two non commuting parts in the Hamiltonian: K and H_{int}. In quantum mechanics the exponential in equation (8.2) can be rewritten by means of the Campbell Baker Hausdorff formula [174]:

$$e^{-\Delta\tau(K+H_{int})} = e^{-\Delta\tau K}e^{-\Delta\tau H_{int}}e^{-\frac{1}{2}\Delta\tau^2[K,H_{int}]} + O(\Delta\tau^3). \tag{8.3}$$

With this trick we can obtain the Trotter-Suzuki decomposition:

$$Z \simeq \operatorname{Tr} \prod_{l=1}^{L} e^{-\Delta\tau K}e^{-\Delta\tau H_{int}}. \tag{8.4}$$

Table 8.1: The Hubbard-Stratonovich transformation can be verified by checking directly all possible combinations of the allowed occupation numbers.

$n_\uparrow$	$n_\downarrow$	$e^{-\Delta\tau U[n_\uparrow n_\downarrow - (n_\uparrow + n_\downarrow)/2]}$	$\frac{1}{2}\sum_{s_l=\pm 1} e^{\alpha s_l(n_\uparrow - n_\downarrow)}$
0	0	1	1
1	0	$e^{-\Delta\tau U/2}$	$\cosh\alpha$
0	1	$e^{-\Delta\tau U/2}$	$\cosh\alpha$
1	1	1	1

The equation (8.4) already represents an achievement, since we can treat K and H_{int} separately. However, we still do not know how to deal with the complicated two-particle term. For every time point $\tau_l = l\Delta\tau$, where $l = 1, 2, \ldots, L$, it is convenient to introduce a field of fluctuating spins s_l which can be used to reproduce the effects of the interactions. Following Hirsch [92, 93, 115] we look for a constant α for which the following relation must hold:

$$e^{-\Delta\tau U[n_\uparrow n_\downarrow - (n_\uparrow + n_\downarrow)/2]} = \frac{1}{2}\sum_{s_l=\pm 1} e^{\alpha s_l(n_\uparrow - n_\downarrow)}. \qquad (8.5)$$

Given that we are considering the system at a given time τ_l, only four possible combinations of occupation numbers are allowed. Then we can directly write down all the elements of equation (8.5), e.g., in Table 8.1, and verify that such an α exists:

$$\alpha = \cosh^{-1} e^{-\Delta\tau U/2}. \qquad (8.6)$$

This is the famous Hubbard-Stratonovich transformation, and is the hearth of the Hirsch-Fye algorithm. Through equation (8.5), the interacting system is reduced to a non-interacting system in a potential depending on the given configuration of the auxiliary spins s_l. Explicitly the potential reads

$$V_l(\{s\}) = \alpha s_l. \qquad (8.7)$$

The potential depends on the time slice and reproduces exactly all the effects of the interactions, as schematized in Figure 8.1.

We want to use the Hubbard-Stratonovich transformation (8.5) for the evaluation of the relevant physical quantities. With a bit of algebra we can show that the partition function can be rewritten as:

$$Z = \mathrm{Tr}_{\{s\}} \left[\det O^\uparrow(\{s\}) \det O^\downarrow(\{s\}) \right], \qquad (8.8)$$
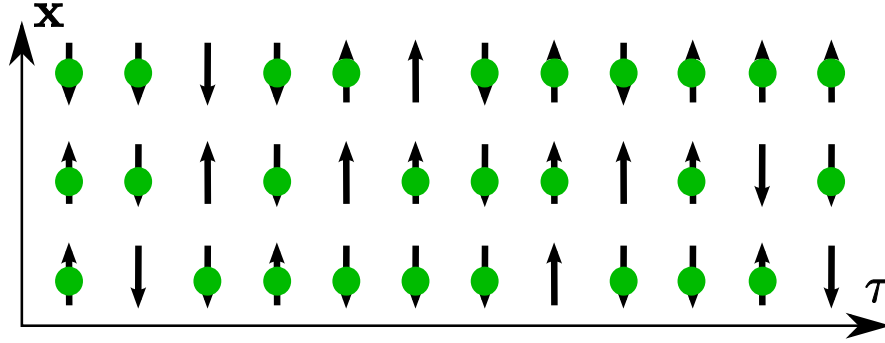
Figure 8.1: In the Hubbard-Stratonovich transformation (8.5) an auxiliary field of so-called "Ising spins" (black arrows) is introduced to compute the main observables of the system. The studied electrons (green dots) move in a fluctuating potential depending on the time slice, and on the spatial degrees of freedom (for multi-orbital and multi-site models).

where the trace is over all the possible configurations of the fluctuating fields. The symbol O^σ indicates a matrix $L \times L$ with the following structure:

$$O_{l,l'} = \begin{cases} 1 & l' = l \\ -e^{-\Delta\tau K}e^{V_{l-1}}(1 - 2\delta_{l,1}) & l' = l - 1 \\ 0 & \text{otherwise} \end{cases} . \qquad (8.9)$$

The matrix O^σ enters also in the computation of the Green's function through the key-relation:

$$G^\sigma(\{s\}) = \left[O^\sigma(\{s\})\right]^{-1}. \qquad (8.10)$$

Finally the physical observable G^σ_{phys} is recovered with the same procedure used for Z, i.e., sampling over all possible configurations of the auxiliary fields. However the sum involves a huge number of 2^L addends, making the operation for a many time slices computationally impossible. A solution to this problem is the use of the Monte-Carlo method for evaluating multi-dimensional sums or integrals [5]. For our model we can use the Boltzmann distribution coming from equation (8.8) as probability distribution for the weight of a given configuration. Then we can proceed to the Monte-Carlo sampling.

Without presenting all the equations for the evaluation of the Boltzmann weights and the update of the Green's function[2], the computational procedure can be schematized in following way:

1 starting from a given arbitrary configuration $\{s\}$, the Green's function is calculated from equation (8.10)

---

[2]The reader can look at one of the Refs. [174, 5, 173] for a more complete survey of the multi-orbital equations.

2 a single spin is flipped at time τ_l, and the probability weight of the new configuration $\{s'\}$ is calculated

3 the ratio of the probability weights of new and old configurations is evaluated, and determines whether the new configuration must be accepted or not

4 if the new configuration is accepted the Green's function is updated

5 the procedure from steps 2-5 is repeated for a certain number of times, usually referred as Monte-Carlo "sweeps".

Two types of errors are associated to this procedure [175]: the Trotter error due to the time discretization, and the statistical error due to the finite number of Monte-Carlo sweeps employed in the calculation of the sums. Both these errors are controllable, then the Hirsch-Fye QMC solver can be considered as numerically exact. Unfortunately the computational effort required for real systems is huge, and scales cubically with the inverse of the temperature and quartically with the number of orbitals.

An important limitation of the QMC algorithm is that it is extremely difficult to work with elements of the Hamiltonian that cannot be written as a product of two number operators. Therefore we cannot use the full four-index U-matrix of equation (3.36), but we need to consider the so-called density-density approximation [176]. Usually it is convenient to rewrite two new matrices separately for U and J, and with only two indices:

$$U_{\xi_1,\xi_2} = U_{\xi_1,\xi_2,\xi_1,\xi_2} \qquad\qquad J_{\xi_1,\xi_2} = U_{\xi_1,\xi_2,\xi_2,\xi_1}. \qquad (8.11)$$

However, in this construction we neglect some important contributions from the local Coulomb repulsion, e.g., the spin-flip and the pair hopping terms [5]. Furthermore the property of rotational invariance of the LDA+U Hamiltonian is violated. In fact the system changes significantly if the quantization axis of the atomic orbitals is rotated, which is completely unphysical. This last problem can be solved adopting a different parametrization of the matrices. It is possible to show [177] that for degenerate orbitals and real valued functions the following matrices

$$U_{\xi_1,\xi_2} \equiv \begin{cases} U & \xi_1 = \xi_2 \\ U - 2J & \xi_1 \neq \xi_2 \end{cases} \qquad\qquad J_{\xi_1,\xi_2} \equiv \begin{cases} 0 & \xi_1 = \xi_2 \\ J & \xi_1 \neq \xi_2 \end{cases} \qquad (8.12)$$

possess the correct properties of symmetry. We still neglect many contributions, but for all the elements of the new matrices we can give an intuitive physical representation, like in Figure 8.2.

Finally we must mention the last drawback of the QMC method. Due to the Trotter and statistical errors the final Green's function has bad analytical properties. As a result, it is difficult to perform the analytical continuation from the
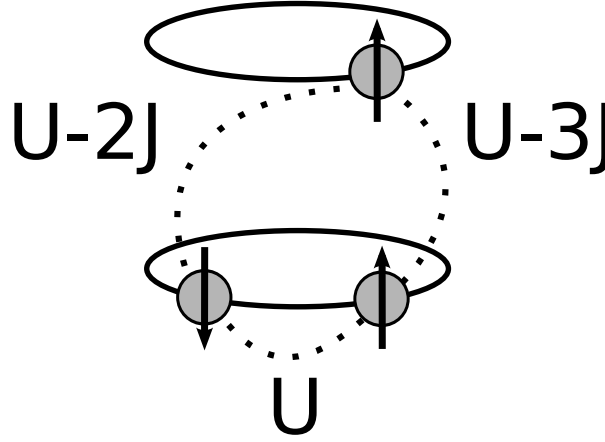
Figure 8.2: In the density-density parametrization of Ref. [177] the U-matrix has three different contributions with a transparent physical meaning: the intraorbital Coulomb repulsion U, the interorbital Coulomb repulsion between different spins $U - 2J$, and the interorbital Coulomb repulsion between the same spins $U - 3J$.

Matsubara axis to the axis of real energies, which is needed to evaluate the physical observables (see Appendix A). In such a situation the Padé approximant method cannot be applied any more, but as an alternative we can employ the maximum entropy method [178, 174]. The latter is a well-defined statistical procedure, and in principle leads to the most probable spectral function. However, in practice, much care is needed since numerical errors that are difficult to discover can be introduced.

Now we can come back to the point stressed at the beginning of this Chapter. Besides its many advantages, QMC presents some important inconveniences: huge computational effort, truncated U-matrix and "problematic" analytical continuation. For these reasons we can find it more convenient to use other solvers for such cases that do not require full generality and high accuracy.

8.2   Disordered local moments

The DLM approach has been introduced in the field of electronic structure calculation to deal with paramagnetic ground-state of crystals. In DFT-LDA the bulk magnetization of a material is proportional to the local magnetic moment, which is invariant in all the crystal cells. Then the only way to obtain zero bulk magnetization is to have zero exchange splitting between the bands associated to different spins. In a single-particle formalism this corresponds to allowing only Stoner-like excitations, neglecting the most important spin fluctuations [179]. All these mechanisms are taken into account in the LDA+DMFT scheme, resulting into changes

of both electronic structure and magnetic properties, as shown successfully for Fe and Ni [28]. DLM is a simpler approach, but, as stressed above, can be useful as starting point for the unperturbed Green's function of the LDA+DMFT scheme.

In the theory of DLM electrons moves in a lattice of atomic sites, but each site is dominated by electrons in a given spin direction [180, 181]. The situation at a given site influences the movement of all the electrons, which tend to align to the dominating spin when passing for that site. In this way the itinerant electrons form self-maintaining "local moments" which are analogous - but physically different - to the localized spins of the Heisenberg model. Now we can make the key-assumption of a time-scale separation between the fast electronic motion, i.e. the "hopping" terms, and the slow motion which is associated to orientational fluctuation of the moments. Being $\hat{\mathbf{e}}_i$ the orientations of the moments at the sites i, we can describe the properties of the system through the generalized grand-canonical potential $\Omega(\{\hat{\mathbf{e}}_i\})$. The term generalized is employed, since Ω is not associated to the thermal equilibrium, but to the constrained orientation of the moments. In DLM a mean-field approximation of the true unknown potential is constructed as expansion around a single-site spin Hamiltonian [181]:

$$\Omega_0(\{\hat{\mathbf{e}}_i\}) = -\sum_i \mathbf{h}_i \hat{\mathbf{e}}_i. \tag{8.13}$$

The parameters $\mathbf{h}_i$, which play a role analogous to a Weiss field, have to be determined. To this aim we introduce an approximate free-energy $\tilde{F}$ that is related to the real free energy F through the Feynman-Peierls inequality

$$F < F_0 + \langle \Omega - \Omega_0 \rangle_0 \equiv \tilde{F}, \tag{8.14}$$

where the average is defined with respect to Ω_0. The minimization of $\tilde{F}$ leads to the parameters $\mathbf{h}_i$. When the grand-canonical potential (8.13) has been determined, we can associate to it a set of probabilities $P_i(\hat{\mathbf{e}}_i)$ of finding the moments oriented towards $\hat{\mathbf{e}}_i$. Explicit calculations can now be made through standard methods used for compositionally disordered alloy, as the Coherent Potential Approximation (CPA) [182, 183, 180]. The DLM equations can be applied to complicated magnetic structures, but they are particularly simple for the paramagnetic phase. Easily the problem can be reduced to a binary alloy, where the half of the sites are occupied by "up" moments and the other half by "down" moments.

The DLM method presented here has been implemented in the FP-KKR code mentioned in Chapter 7, since the CPA equations become straightforward in multiple scattering theory. On the other hand it is very difficult to implement QMC in LDA+DMFT codes based on FP-KKR: the Green's function needs to be analytically continued in the complex plane during the cycle, but this cannot be done because of the bad analytical properties descending from the numerical errors. Then in the next Section we are going to present our study of γ-Mn with

a twofold approach: QMC simulations with FP-LMTO and DLM+SPTF simulations with FP-KKR. The LDA+DMFT simulations with (only) the SPTF solver have been made using both the codes, leading to an excellent agreement which is consistent with the previous findings for the ground-state properties of Ni and Mn (see Section 7.5).

Finally, for a more direct comparison between theory and experiment, photoemission spectra have been produced within the so-called one-step model [184, 185], which has been recently implemented in FP-KKR [29]. The main idea is to describe the excitation process, the movement of the electron towards the surface, and the final escape from the surface, as a single quantum-mechanically coherent process, which is comprehensive of all the multiple scattering events.

8.3   Weak and strong correlations in γ-Mn

To allow comparison with previous LDA+DMFT results and experimental data, we assumed a face centered tetragonal structure with lattice constant $a = 7.143$ a.u. and a tetragonal distortion corresponding to $c/a = 0.93$. We have included $4s$, $4p$ and $3d$ in the valence electrons; all the other states were considered as core states. In the FP-LMTO basis functions with three tail energies κ were used, while in FP-KKR scattering matrix elements up to $l_{max} = 3$ were included. No significant differences could be found in comparing the LDA results.

In the LDA+DMFT simulation, the local Hubbard interaction was applied to the $3d$ electrons. The Coulomb and exchange parameters U and J were varied among a wide range of reasonable values. We have studied configurations corresponding to different parameters through QMC at temperature ranging from $T \simeq 2000$ K down to $T \simeq 500$ K. Convergence in the number of time-slices has been checked, and for high U or low temperature a number of $L = 128$ time slices has been used. The number of Monte-Carlo sweeps has been set to 500000, and convergency has been checked up to 10^7.

In Figure 8.3 we show the density of states of the $3d$ electrons obtained through maximum-entropy method. In the bottom of the figure we have used an exchange parameter $J = 0.9$ eV, and the results reproduce quite reasonably the three-peak structure of Ref. [116]. By turning on the Coulomb repulsion U, two splitted Hubbard bands form and a quasiparticle Kondo-like resonance appears close to the Fermi level. In comparison to the cited results, our central peak results almost completely smeared out because of the high temperature, but still its foot-print can be seen in the spectrum. In the top of Figure 8.3 we have reported the density of states for the same simulations, but with a slightly different exchange $J = 0.75$ eV. Strong differences can be observed: the system can form Hubbard bands only for a very strong U, and the energy separation between them is smaller than the bare U. While for high J the electrons are observed to redistribute equally among all
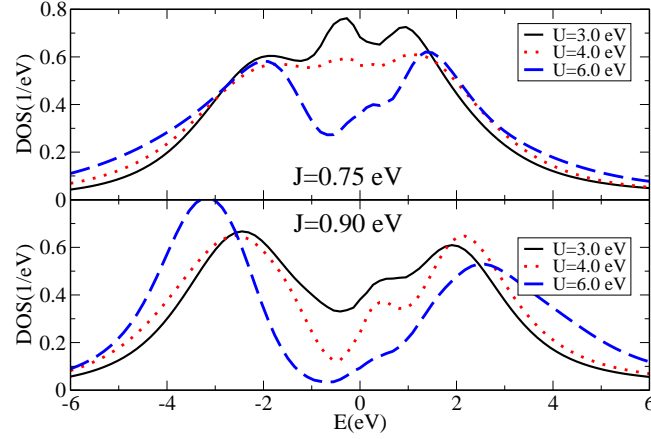
Figure 8.3: Density of states of the $3d$ electrons of γ-Mn from QMC in the LDA+DMFT scheme for $T = 2000$ K. In the top plot results for $J = 0.75$ eV and U changing from 3 eV to 6 eV are shown. In the bottom plot results for $J = 0.9$ eV and same U as above are shown. Notice the big impact of small variations of J on the final spectrum.

the orbitals in a way to minimize the QMC double occupation, for small J this does not happen and the occupations of the $3d$ orbitals stay closer to the original LDA values.

A simple physical picture can be formulated in terms of the matrix elements of equation (8.12), or equivalently of Figure 8.2. For high J there is a strong difference between the intraorbital matrix elements U and the interorbital matrix
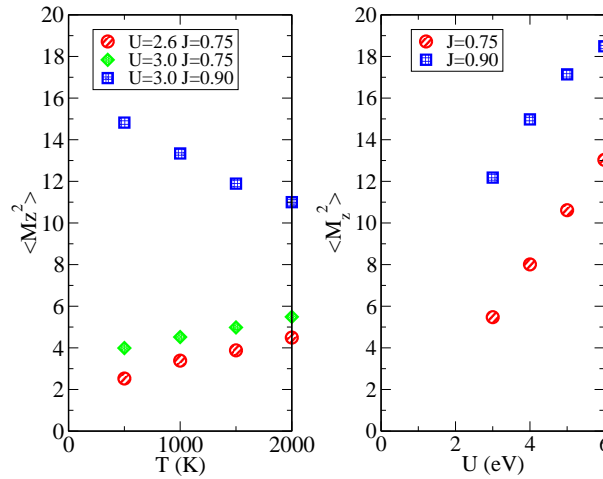

Figure 8.4: Left side: variation of the squared local magnetic moment as function of the temperature. Right side: variation of the squared local moment in function of U at $T = 2000$ K

elements $U-2J$ or $U-3J$. Then the system can redistribute the electrons equally among all the orbitals, compensating the loss of kinetic energy with the strong gain of Coulomb energy. For low J this picture does not hold: now the electrons feel the presence of the other electrons irrespectively to the orbital order. Then the kinetic energy tends to preserve the LDA occupations. The problem is that the transition between these two regimes happens close to the real physical value of J. Semi-empirical estimate and constrained LDA calculations give the exchange parameter coincident with its atomic value $J = 0.9$ eV. On the other hand recent calculations through constrained random-phase approximation [186] suggests that some screening can be present.

More information about the different physical situations can be obtained by looking at the square of the local moment $\langle M_z^2 \rangle$, which in QMC is associated to the local spin correlation function[3]. This moment depends strongly on the temperature, as we can see at the left hand side of Figure 8.4 for four pairs of parameters U and J.

For high temperature, i.e., for T bigger than U, we expect the system to show a contribution to the effective Curie constant of about 0.5 for each orbital, which corresponds to local spins decoupled from each other [187]. In fact this is the tendency we observe in our calculations, not shown in the pictures. For low temperature, i.e., in the interval between 2000 K and 500 K, the physics of manganese is strongly dependent on J. For low J the spin fluctuations are decreased because of the presence of strong orbital fluctuations [188], which become important when the temperature becomes lower. The electrons tend to behave as a Pauli paramagnet, and the local moment decreases together with the temperature. Conversely for high J the electrons tend to localize in each band independently, resulting in the suppression of the orbital fluctuations. As a result a strong fluctuating local moment can form. These different tendencies have been previously studied in the two-orbital Hubbard model [188], and it is interesting to see how they can be found in a real material with five (almost) degenerate orbitals and realistic hybridization. Note that the experimental local magnetic moment is about 2.3 Bohr magnetons, suggesting a situation in between the two different regimes. On the right side of Figure 8.4 we can see also the trend of the local moments for various values of U.

In Figure 8.5 the comparison of all the significant density of states of our work is reported. In the upper panel we can see the bare LDA results and in the middle the LDA+DMFT results with QMC for $U = 3$ eV and $J = 0.75$ eV or $J = 0.9$ eV. At the bottom we see the density of states obtained in DLM and in DLM+SPTF. While DLM describes the fluctuations in a very simple way, still a sort of three peak structure is observed. However the width of the $3d$ band is too big, since it descends from the single particle LDA density of states. In DLM+SPTF we can properly describe the shrinking of the $3d$ band, as already observed for Fe,

---

[3]Note that $\langle M_z \rangle = 0$, since we are dealing with the paramagnetic phase.
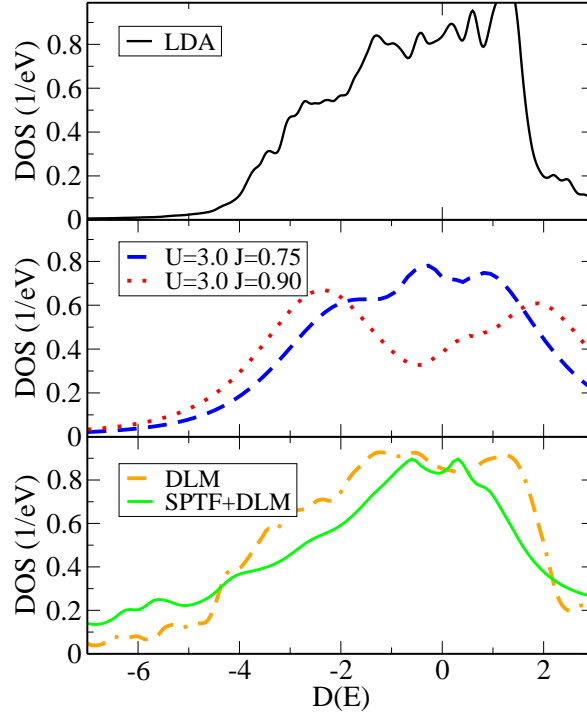
Figure 8.5: Comparison of the significant density of states of the $3d$ electrons presented in the paper. Top: DFT-LDA density of states. Middle: QMC density of states for $U = 3.0$ eV and different values of J. Bottom: DLM and DLM+SPTF density of states for $U = 3.0$ eV and $J = 0.8$ eV.

Co and Ni in Chapter 4. In comparison with QMC we observe that the peak at around -2 eV is less pronounced. This depends on the perturbative nature of SPTF, which tends to shift the correlation effects related to the formation of non-coherent satellites. For example the famous - 6 eV satellite of Ni is positioned at about - 8 eV. For Mn part of the spectral weight is transferred to the region between -4 and -6 eV. While DLM+SPTF can reproduce very well the density of states far from the localization, the appearance of the Mott Hubbard pseudogap observed in the simulation for high J cannot be reproduced in this approach.

On the basis of these considerations, we can look at the photoemission spectrum reported in Figure 8.6 together with the experimental data of Ref. [116], referred to the surface (100) in normal emission. This corresponds to the high-symmetry direction $\Gamma - X$ in the Brillouin zone. Let us discuss first the bare DLM approach. In comparison with the experimental data, or with the LDA+DMFT calculations with the QMC solver [116], the "Hubbard band" feature is shifted to larger energy and the "quasiparticle peak" near the Fermi energy turns out to be too broad. The use of the DLM+SPTF approach improves essentially description of the states near the Fermi energy but smeared completely the "Hubbard band".
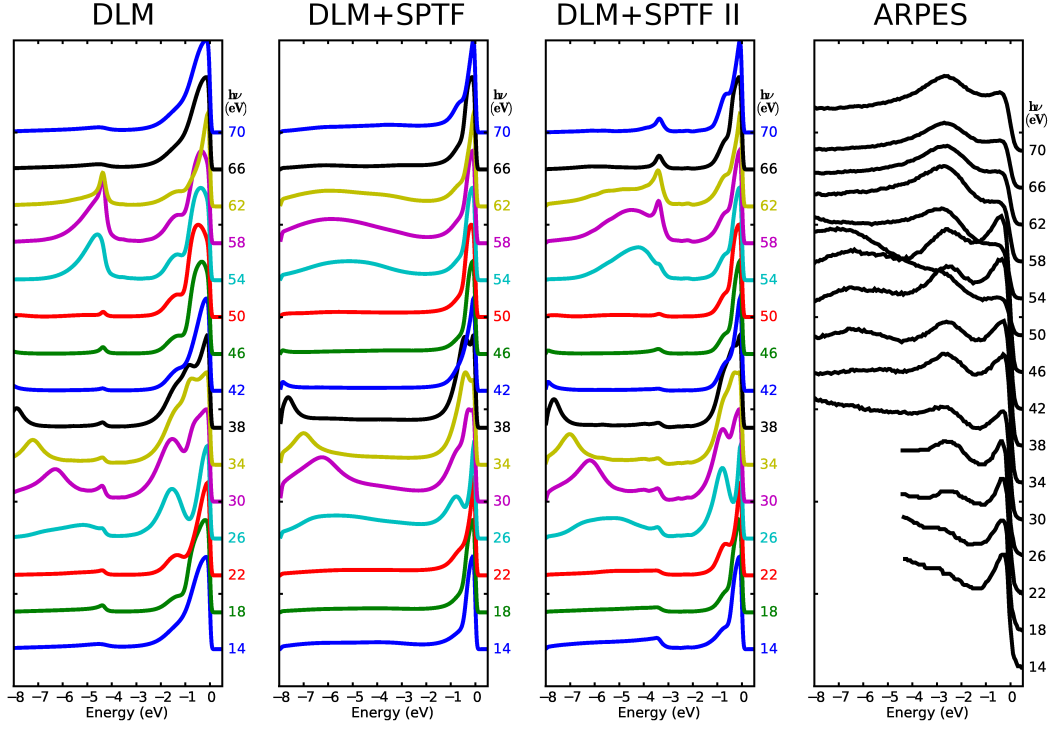
Figure 8.6: Photoemission spectrum within the one-step model for DLM, DLM+SPTF and experimental data of Ref. [116], referred to the surface (100) in normal emission. The data of the column labelled DLM+SPTF II correspond to the removal of the imaginary part of the self-energy. The numbers close to each spectrum indicate the energy of the incident photon.

Probably, this is due to overestimation of the imaginary part of self-energy for larger excitation energies. Indeed, if one takes into account only real part of the self energy (DLM+SPTF II) the description of the spectra can be drastically improved. This reminds a situation with the GW calculations where neglecting the electron state damping sometimes essentially improves the results [189].

Real manganese is strongly correlated metal, with the Hubbard bands [116]. In such cases, instead of the cumbersome and computationally expensive QMC calculations, the DLM+SPTF approach can be used to describe adequately the energy spectrum close enough to the Fermi energy, but not in the whole energy range. For moderately correlated systems, which were modelled here by variation of J, the DLM+SPTF approach turns out to be adequate for the whole spectrum. Neglecting imaginary part of the self energy can provide better description of the photoemission data.

Chapter 9

Limit of very strong correlations: Hubbard I approximation

In the previous Chapters we have explored a range of systems ordered for increasing strength of correlation effects. In the last material analyzed, i.e. γ-Mn, we could observe clear signs of strong correlations, as the formation of Hubbard bands, but the local Coulomb repulsions could not yet drive a transition from the metallic to the insulating phase. In this Chapter we address our analysis to materials with partially filled f-electron shells: the electrons in narrow bands are extremely localized, leading to the formation of multiplet structures in the excitation spectrum. The resulting physical picture is closer to the atomic limit than to a system of itinerant electrons, and an adequate theoretical method must be applied. Here we focus on the Hubbard I approximation [6, 18], which can be considered as an "ancestor" of the LDA+DMFT scheme [18]. In fact the lattice problem is mapped onto an atomic problem, and latter is then solved through the exact diagonalization. Naturally the atomic problem is different than the effective impurity model, due to the absence of hybridization between localized and itinerant electrons. In any case the Hubbard I approximation is very successfull if applied to a proper class of materials. Here we present the calculation of the spectral properties of intermediate-valence compounds, followed by a comparison with experimental photoemission spectra.

The present Chapter is based on the following publication:

1. P. Thunström, I. Di Marco, A. Grechnev, S. Lebègue, M. I. Katsnelson, A. Svane, and O. Eriksson "Multiplet effects in electronic structure of intermediate valence compounds", *Phys. Rev. B* **79**, 165104 (2009)

9.1   Intermediate-valence compounds

The partially filled f-electron states in pure $4f$- and $5f$-metals usually form either localized atomic-like shells, e.g. rare earth elements [190], or delocalized valence band states, e.g. light actinides [191]. However, their compounds often lie in between these two extremes, with the f-electrons forming very narrow bands with strong Coulomb correlations. These narrow bands show both a valence-like and atomic-like behavior: for example their electrons contribute to the chemical binding but also give rise to a multiplet structure in the excitation spectrum. Furthermore, a Kondo-like resonance often occurs in the meV energy scale around the Fermi level [192]. The complex competition between itinerant and localized electronic behavior results into materials with very interesting physical properties, such as intermediate valence (IV) systems [193, 194, 195] which have ground states where the f-manifold rapidly fluctuates between a f^n and f^{n+1} configuration.

Intermediate-valence systems are sometimes metallic down to very low temperatures with ground states which can be described as paramagnetic Fermi liquids [196, 197]. Here we consider three intermediate-valence systems, $YbInCu_4$, YbB_{12}, and SmB_6 which all break this rule as the temperature is lowered. At ambient pressure $YbInCu_4$ undergoes a first-order isostructural electronic phase transition at $T_c \approx 40$ K, which causes the electrical resistivity and the effective magnetic moment to drop by an order of magnitude [198]. YbB_{12} and SmB_6 on the other hand are classical examples of narrow-gap semiconductors which form a gap of 10 meV as the temperature is lowered [192]. From theoretical point of view, they are considered as excitonic insulators [199, 200] or Kondo insulators [192].

$YbInCu_4$, YbB_{12}, and SmB_6 have been thoroughly studied by for example photoemission [201, 202, 203, 204, 205, 206], resonant inelastic X-ray scattering [207, 203, 208], electrical transport [209, 210], neutron scattering [211, 212, 213, 214], Mössbauer [215, 216, 217], and optical [218, 219, 220] measurements.

Although the anomalous properties of these materials have been known for decades [221, 222, 223, 224, 198] the underlying mechanism and relation to the intermediate-valence ground state is still under discussion [225, 226, 200, 227, 228, 229, 214, 208]. Much of the effort has been centered around the description of the electronic structure in the meV energy scale close to the Fermi level. The electronic structure on the eV scale, describing the rich multiplet structures seen in photoemission experiments, has received substantially less attention although a full description of the problem. This large scale electronic structure has so far only been addressed using LDA [230] [231] [232] or LDA+U [233] [234]. It is worth noting that in Ref. [233] an atomic multiplet spectrum was positioned on top of the LDA+U density of states, in order to simulate the experimental multiplet structures. The poor agreement between the density of states from a regular LDA or LDA+U calculation and the observed photoemission spectrum of these

materials highlights the need to include a more accurate description of the strong electron-electron correlations in the electronic structure calculations, especially if any post-processing procedure interprets the Kohn-Sham quasi-particles as real electronic excitation.

Our interest is focused on the electronic structure on the eV scale, and on the accurate description of the multiplet structure. All the signals of strong electron-electron interactions in $YbInCu_4$, YbB_{12}, and SmB_6 suggest that an accurate description of their electronic structure can be obtained through the LDA+DMFT method. In this context the solution of the effective impurity model within the Hubbard-I approximation [6, 18] seems to be a convenient choice. In fact this method has shown to give an adequate description of localized f-electron systems such as various Lanthanide and Actinide compounds [235, 236, 237, 128]. These calculations were performed using a LMTO method in ASA, which is unfortunately not reliable for materials with open crystal structure like $YbInCu_4$, YbB_{12}, and SmB_6.

9.2 Hubbard I approximation

The Hubbard-I approximation (HIA) combines the many-body effects necessary to describe localized atomic-like states, in our case the $4f$-states of Yb and Sm, with the wide bands formed by delocalized valence electron states. It can be expressed in a reduced LDA+DMFT scheme where the local self-energy is obtained from an atomic calculation instead of a self-consistent DMFT cycle [15, 5].

The atomic model used in HIA is built around an Hamiltonian that describes only the correlated states of a single ion at a given site $\mathbf{R}$:

$$\hat{H}^{at} = \hat{H}^{at}_{0\mathbf{R}} + \frac{1}{2} \sum_{\xi_1,\xi_2,\xi_3,\xi_4} U_{\xi_1,\xi_2,\xi_3,\xi_4} \hat{c}^\dagger_{\mathbf{R},\xi_1} \hat{c}^\dagger_{\mathbf{R},\xi_2} \hat{c}_{\mathbf{R},\xi_4} \hat{c}_{\mathbf{R},\xi_3} - \mu_{at} \sum_{\xi_1} \hat{c}^\dagger_{R,\xi_1} \hat{c}_{R,\xi_1}. \quad (9.1)$$

Again, the indices ξ label the correlated orbitals, and $\hat{c}^\dagger_\xi$ and $\hat{c}_\xi$ are the corresponding creation and annihilation operators.

$\hat{H}^{at}_{0\mathbf{R}}$ contains the single particle LDA Hamiltonian, calculated without spin-orbit coupling, projected onto the correlated states. The spin-orbit coupling is instead added explicitly as a second term,

$$\hat{H}^{at}_{0\mathbf{R}} = \sum_{\xi_1,\xi_2} \langle \mathbf{R}\xi_1 | \hat{H}_{KS} + \tilde{\xi}\mathbf{l} \cdot \mathbf{s} | \mathbf{R}\xi_2 \rangle \, \hat{c}^\dagger_{\mathbf{R},\xi_1} \hat{c}_{\mathbf{R},\xi_2} \quad (9.2)$$

where $\hat{H}_{KS}$ is the LDA Hamiltonian, $\tilde{\xi}$ is the spin-orbit constant[1], $\mathbf{l}_i$ and $\mathbf{s}_i$ are the orbital moment and spin operators. The projection onto the correlated orbitals

---

[1]Do not confuse the index ξ for the correlated orbitals with the spin-orbit constant $\tilde{\xi}$.

removes all off-diagonal "hopping" terms to states orthogonal to the correlated orbitals at site $\mathbf{R}$ but keeps the crystal field effects. The site index $\mathbf{R}$ is from here on implicit.

The last term in equation (9.1) contains the chemical potential μ_{at} which is used to embed the atom in the solid. Here the chemical potential is also used to cancel the energy contribution from the double counting of the one-body terms of the Coulomb interaction. How to obtain an accurate double counting correction in an LDA+HIA scheme is still an open question, so in the present model we treat the chemical potential as an adjustable parameter[2].

The atomic Hamiltonian is diagonalized in the complete space of all Slater determinants of a given f^n configuration. In addition to the f^n configurations found in the mixed ground state also the neighboring $f^{n\pm1}$ configurations must be included in the calculation to account for possible excitations. From the eigenvalues, E_ν, and eigenvectors, $|\nu\rangle$, one can construct a local one-particle Green's function

$$G^{at}(\omega)_{\xi_1\xi_2} = \frac{1}{Z}\sum_{\mu\nu} \frac{\langle\mu|\hat{c}_{\xi_1}|\nu\rangle\langle\nu|\hat{c}_{\xi_2}^\dagger|\mu\rangle}{\omega + E_\mu - E_\nu} \left(e^{-\beta E_\mu} + e^{-\beta E_\nu}\right), \qquad (9.3)$$

where $\beta = 1/k_B T$ and T is temperature. On the other hand we can also define the unperturbed Green's function associated to the Hamiltonian (9.2):

$$G_0^{at}(\omega)_{\xi_1\xi_2} = \langle\xi_1|[\omega - \hat{H}_0^{at}]^{-1}|\xi_2\rangle \qquad (9.4)$$

The atomic self-energy $\Sigma^{at}(\omega)$ is then obtained in terms of inverse Dyson equation, i.e., from

$$\Sigma^{at}(\omega) = \left[G_0^{at}(\omega)\right]^{-1} - \left[G^{at}(\omega)\right]^{-1}. \qquad (9.5)$$

Now we are able to understand the connection between the LDA+HIA and the LDA+DMFT scheme. It is straightforward to identify the atomic Hamiltonian (9.1) as the impurity of equation (2.38), and consequently the self-energy $\Sigma_{imp}(\omega)$ with $\Sigma^{at}(\omega)$. Then we effectively reduce the DMFT cycle to a "one shot" procedure, which can be done directly for real energies, without need of working on the Matsubara axis[3]. In this way we can also clarify the limits of applicability of the HIA. If we compare the unperturbed atomic Green's function (9.4) with the unperturbed Green's function (2.42) of the effective impurity model, we see that the main difference concerns the absence of the function $\Delta(\omega)$, which embeds the hybridization effects between the local problem and the electronic bath. In fact the HIA can also be obtained from the functional expansion of the full Green's

---

[2]Look at Ref. [133] for an example of alternative choice.

[3]As we have verified during the development, the result does not change when working on the Matsubara axis. In fact the self-energy in HIA has very good analytical properties, which makes it easier to do numerical analytical continuation through Padé approximation.

function of the Anderson model in terms of $\Delta(\omega)$, by keeping only the zero-th order term [238].

From the previous argument we can understand that the HIA is suitable only for localized systems with little hybridization with the other valence electrons. While in the HIA we obtain correct atomic limit and non-interacting limit, we do not always have satisfactory results in between. Probably the most famous failure of the HIA is that, at half-filling, it predicts Hubbard bands and insulating character for every value of U.

9.3 Results

The construction of the LDA+U Hamiltonian, and consequently of the atomic Hamiltonian, for f-electrons requires the Slater integrals F^0, F^2, F^4, and F^6. In the previous Chapters the Slater integrals were determined in terms of U and J, as illustrated in Section 3.3. Here we have determined the values of these parameters, except for F^0, from *ab initio* calculations [239], and the results can be found in Table 9.1. The physically relevant value of the first Slater integral F^0, which corresponds to the Hubbard U, is reduced from the bare value due to the screening of non-f-electrons, and is set to be 8 eV for all the compounds in the present study. In Table 9.1 we can find also the spin-orbit coupling parameter $\tilde{\xi}$, which is needed to set up the Hamiltonian (9.2). Finally all the calculations were performed for $T = 630$ K.

9.3.1 YbInCu$_4$

To begin our study of the intermediate valence compounds we consider YbInCu$_4$. It has the MnSnCu$_4$ type crystal structure derived from space group #216 ($F\bar{4}3m$) with lattice parameter $a = 13.52$ a.u., and In in Wyckoff position 4a, Yb in 4c, and Cu in 16e, with parameter $x = 0.625$. The ground state configuration of Yb

Table 9.1: The values of the parameters used for the U-matrix (3.36), obtained *ab initio* from radial integration of the f-partial waves of a self-consistent LDA calculation. F^0 is set to be 8 eV for all the compounds in the present study.

	F^2 (eV)	F^4 (eV)	F^6 (eV)	$\tilde{\xi}$ (eV)
YbInCu$_4$	15.66	9.75	6.99	0.3888
YbB$_{12}$	15.83	9.86	7.08	0.3925
SmB$_6$	12.40	7.70	5.52	0.1635

in YbInCu$_4$ is a mixture of f^{13} and f^{14}, which gives rise to an X-ray photoelectron spectroscopy (XPS) spectrum that contains both f^{14} to f^{13} and f^{13} to f^{12} transitions.

The partial density of states from the LDA+HIA calculation is shown in the upper panel of Figure 9.1, together with an experimental photoemission spectrum from Ref. [203]. The agreement is excellent, and all the major peaks observed in the experiment are reproduced by the present theory. The double peak structure between -2 eV and 0 eV corresponds to f^{14} to f^{13} transitions where the final states $^2F_{5/2}$ and $^2F_{7/2}$ are separated in energy by 1.3 eV due to the spin-orbit interaction. Hybridization effects causes the latter peak to broaden and shift by 0.2 eV to higher binding energies compared to the bare atomic levels. At higher binding energies, between -12 eV to -5 eV, the structures are caused by f^{13} to f^{12} transitions.

Three distinct peaks are observed in the experimental spectrum between -6 eV and -9 eV, which are related to final states of ^{3}H, ^{3}F and ^{1}G character. However, due to the large spin-orbit coupling these peaks are split and shifted by up to 2 eV into the complex six-peak structure seen in the experimental and theoretical spectrum. Since the spin-orbit coupling does not conserve the L and S quantum numbers the spectroscopical notation in Figure 9.1 becomes only approximate except for the J quantum number. Between -12 eV and -10 eV three peaks are seen in the calculated spectrum, which can be associated with the ^{1}D, ^{1}I and ^{3}P final states. These peaks are shifted and in the latter case also split by the spin-orbit coupling. Only the first two peaks are clearly visible in the experiment, while the ^{3}P appears as the shoulder around -11.5 eV. The experimental peak positions occur at slightly lower (0.3 eV) binding energies compared to the calculation.

The lower panel of Figure 9.1 shows the f-partial density of states for YbInCu$_4$ in the LDA, where the f-manifold is treated as one-electron band states. This leads to a concentration of all the f-electron spectral weight in a narrow peak at the Fermi level, which is in sharp contrast to the experimental spectrum that shows the f-spectral weight distributed over a 12 eV range.

9.3.2   YbB$_{12}$

The next intermediate valence compound in our study is YbB$_{12}$. It has the UB$_{12}$ type crystal structure given by space group #225 ($Fm\bar{3}m$) with Yb in Wyckoff position 4a and B in 48i with parameter $y = 0.166$, and lattice constant $a = 14.11$ a.u.. The ground state configuration of Yb is a mixture of f^{13} and f^{14}, similar to that found in YbInCu$_4$, which gives rise to striking similarities in their partial densities of states. The calculation reproduces all the main features in the XPS spectrum, as shown in Figure 9.2, but similar to YbInCu$_4$ the peaks between -13 eV and -9.5 eV are found to be located at approximately 0.4 eV too large binding energy. Compared to the YbInCu$_4$ case, the experiment clearly resolves
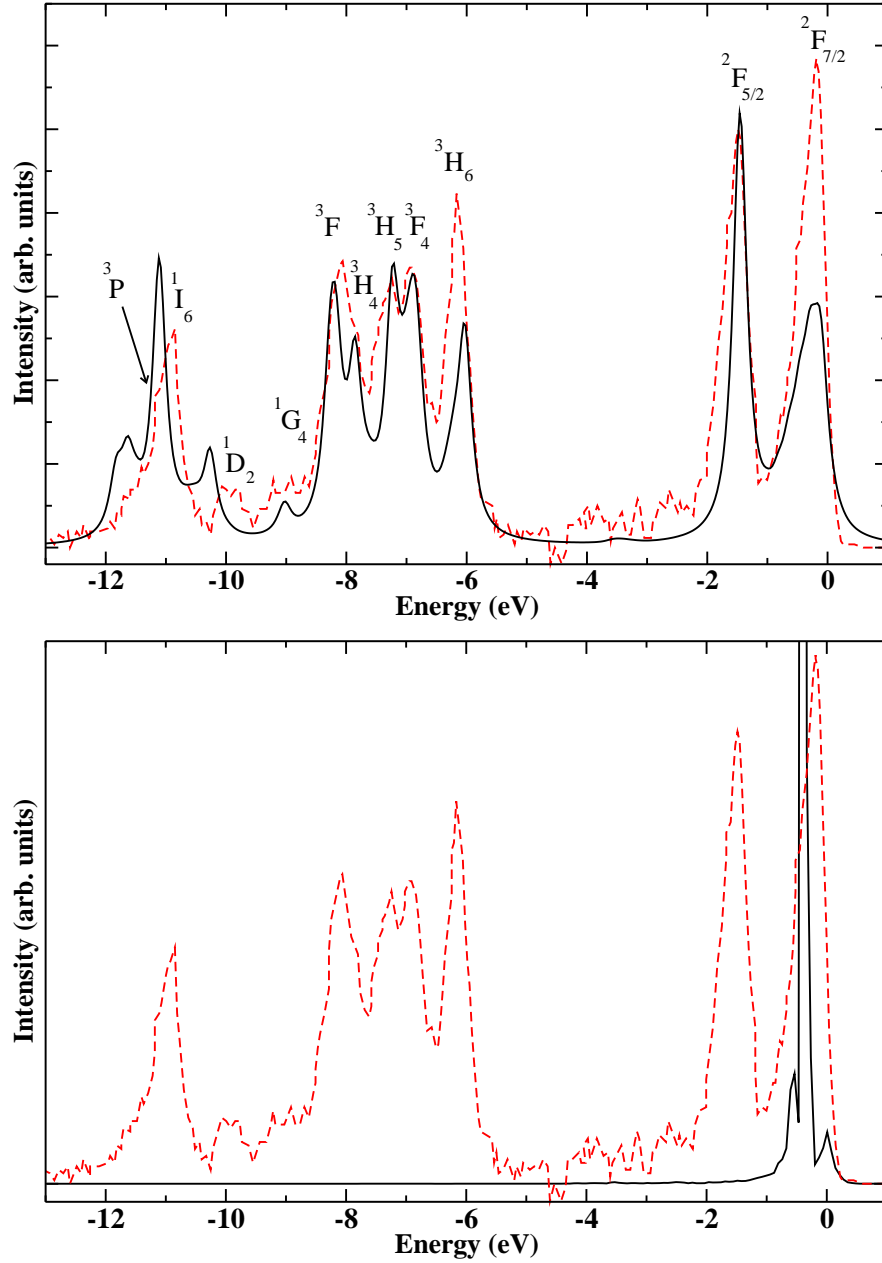
Figure 9.1: Partial density of states from LDA+HIA (full black line) and experimental photoemission spectrum from Ref. [203] (dashed red line) of the Yb f-electron states in YbInCu$_4$ (upper panel). The f-projected density of states from the LDA calculation (full black line) with the measured photoemission spectrum (lower panel).

all the spin-orbit induced splittings including the split-off peak at -9 eV.

9.3.3 SmB_6

SmB_6 has the CaB_6 type crystal structure given by space group #211 ($Pn\bar{3}m$) and lattice parameter a = 7.81 a.u.. Sm occupies Wyckoff position 1a, and B occupies position 6f with parameter $x = 0.2$. The ground state configuration of Sm in SmB_6 is a mixture of f^5 and f^6; therefore the observed XPS spectrum corresponds to excitations from f^6 to f^5 and f^5 to f^4.

Figure 9.3 shows the partial density of states for the Sm $4f$-orbitals in SmB_6 obtained from LDA+HIA. A photoemission spectrum from Ref. [204] is included for comparison. The overall agreement is quite good. The peaks between -5 eV and 0 eV corresponds to excitations from f^6 to f^5 with final states ^6P, ^6F, and ^6H. The ^6F and ^6H peaks at 0 eV and -1.1 eV compare fairly well to the features in the experimental XPS spectrum, considering that the photoemission spectroscopy only shows the occupied part of the spectrum. The structure around -4 eV may be identified with the ^6P final state. It is located at approximately 0.4 eV too large binding energy in the calculation compared to the experimental shoulder. The structures between -12 eV and -5 eV are associated with the excitations from f^5 to f^4 with final states ^5D, ^5G, ^5F, and ^5I. The central ^5G and ^5F peaks are positioned at 9.7 eV and 8.9 eV which agrees fairly well with the position of the lower of the two peaks observed in experiment. The ^5D is hardly visibly in the experiment, while the ^5I peak may be identified with the experimental peak at -7.5 eV (shifted by 0.7 eV). The theoretical curve shows a number of multiplet-like features in the unoccupied states, which in the lack of experimental observations, can be viewed as a prediction.

Figure 9.2: Upper panel: partial density of states from LDA+HIA (full black line) and experimental photoemission spectrum from Ref. [206] (dashed red line) of the Yb f-electron states in YbB$_{12}$. Lower panel: comparison of the partial density of states from LDA+HIA of YbB$_{12}$ (full black line) and YbInCu$_4$ (dashed black line).

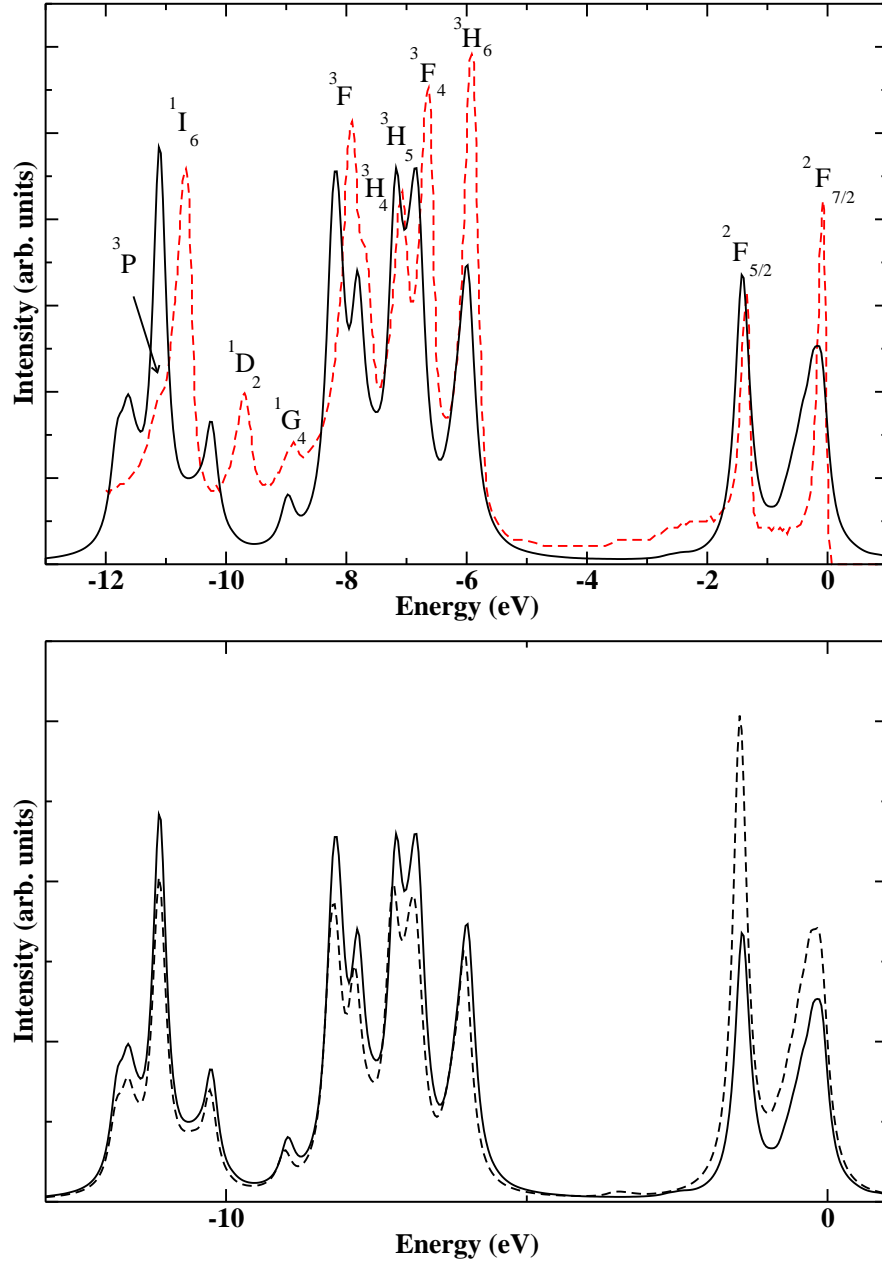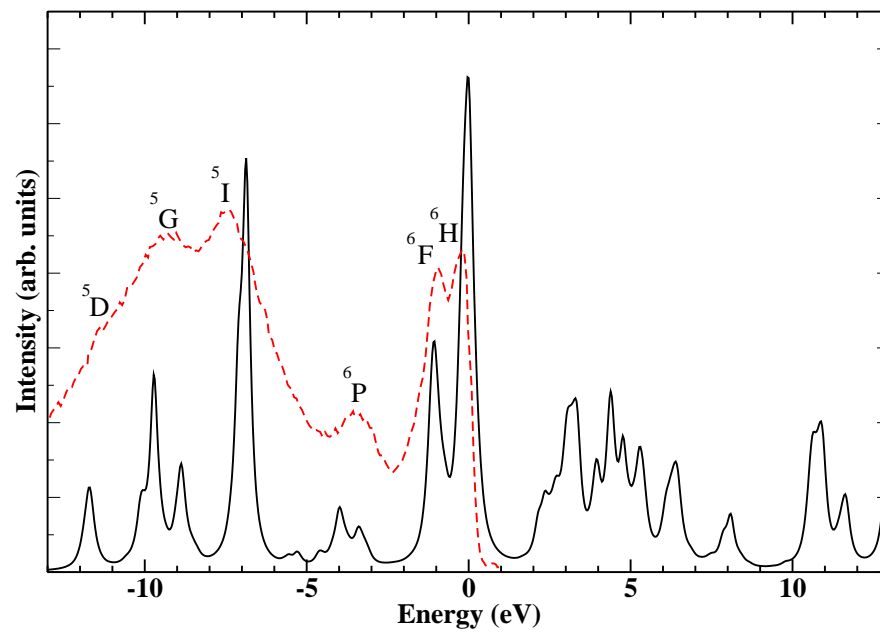**Figure 9.3:** Partial density of states from LDA+HIA (full black line) and experimental photoemission spectrum from Ref. [204] (dashed red line) of the Sm f-electron states in SmB_6.

Appendix A

Green's Functions

The solution of typical problems of quantum physics can be often simplified with the introduction of a powerful mathematical object: the Green's function. Despite its name, the Green's function is an operator that can be associated to any differential operator. As a result linear differential equations can be reduced to integral equations that include also the correspondent boundary conditions. This is why in mathematical analysis the name *resolvent* is usually preferred.

In this Appendix the basic definitions and applications of the many-body theory based on the Green's function are summarized. In the first Section the concept of Green's function is introduced for the description of the response of a system to an external perturbation. In the second Section the emphasis is moved on a particular class: the one-particle Green's function. Finally in the last Section the Matsubara formalism for many-body perturbation theory at finite temperature is presented.

A.1 Response and Green's function

From the physical point of view the general meaning of the Green's function can be illustrated by considering the linear response $s(t)$ of a classical system to an external perturbation $f(t)$, schematized on the left side of Figure A.1. If we assume the classical system to be a black box satisfying the property of linearity and causality, the response can be expressed as

$$s(t) = \int_{-\infty}^{+\infty} dt' G(t, t') f(t').$$ (A.1)

The Green's function G contains the dynamics of the system *independently* on the external perturbation. Once that G has been found, the problem is solved for every function $f(t)$. It is clear that finding G is a quest at least as hard as solving the original equation for a given $f(t)$. Nevertheless the Green's function satisfies some nice properties, which makes it easy to define a controlled perturbation theory.
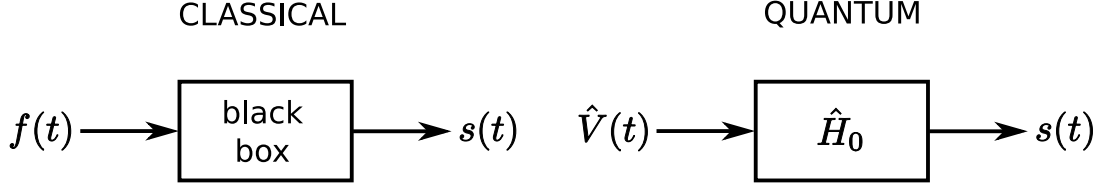
CLASSICAL   QUANTUM

$$f(t) \longrightarrow \boxed{\begin{array}{c}\text{black}\\\text{box}\end{array}} \longrightarrow s(t) \qquad \hat{V}(t) \longrightarrow \boxed{\hat{H}_0} \longrightarrow s(t)$$

Figure A.1: Left: scheme of the response $s(t)$ of an unknown classical system under the action of an external perturbation $f(t)$. Right: scheme of the response $s(t)$ of a quantum system $\hat{H}_0$ under the action of a time-dependent external perturbation $\hat{V}(t)$.

For quantum cases it is not so straightforward to write down an equation similar to (A.1), but more algebra is required. Let us consider a quantum system described by the Hamiltonian $\hat{H}_0$ and object of a perturbation $\hat{V}(t)$ (right hand side of Figure A.1). Analogously to the classical example, we want to study the response of a given observable $\hat{O}$ to the external perturbation. In absence of the perturbation, at a time $t_0 = -\infty$, the expectation value of $\hat{O}$ is $\langle\hat{O}\rangle_0$, where the average is calculated through the statistical operator $\hat{\rho}_0$. For finite times the statistical operator evolves following the quantum Liouville equation

$$i\hbar\frac{\partial\hat{\rho}}{\partial t} = \left[\hat{H}_0 + \hat{V}(t), \hat{\rho}\right]. \tag{A.2}$$

Moreover, if we adopt the Dirac representation, a generic operator $\hat{A}$ rotates in the Hilbert space as

$$\bar{A}(t) \equiv \hat{U}^\dagger(t)\hat{A}\hat{U}(t) \tag{A.3}$$

where the time-evolution operator is

$$\hat{U}(t) = e^{-\frac{i}{\hbar}\hat{H}_0(t-t_0)}. \tag{A.4}$$

Combining the previous equations, and with a little bit of algebra, we can obtain that at first order

$$\hat{\rho}(t) = \hat{\rho}_0 - i\hat{U}(t)\int_{t_0}^t dt'\left[\bar{V}(t'), \hat{\rho}\right]\hat{U}^\dagger(t). \tag{A.5}$$

Now we are ready to determine the expectation value of $\hat{O}$ at the time t:

$$\langle\hat{O}\rangle(t) = \text{Tr}\left\{\hat{\rho}(t)\hat{O}\right\} = \langle\hat{O}\rangle_0 - i\,\text{Tr}\left\{\hat{\rho}_0\int_{t_0}^t dt'\left[\bar{O}(t), \bar{V}(t')\right]\right\}. \tag{A.6}$$

Additionally we define the response of the system as

$$s(t) \equiv \langle\hat{O}\rangle(t) - \langle\hat{O}\rangle_0, \tag{A.7}$$

and we consider the special case of a perturbation coupled to a static operator:

$$\hat{V}(t) \equiv f(t)\hat{V}_0. \tag{A.8}$$

By means of equations (A.6), (A.7) and (A.8) we can obtain

$$s(t) = -i \operatorname{Tr}\left\{\hat{\rho}_0 \int_{t_0}^{t} dt' \left[\bar{O}(t), \bar{V}_0(t')\right]\right\}. \tag{A.9}$$

This expression is equivalent to the classical equation (A.1), if we adopt the following definition:

$$G(t,t') \equiv -i \left\langle \left[\bar{O}(t), \bar{V}_0(t')\right]\right\rangle \Theta(t - t'), \tag{A.10}$$

where we have introduced the step function Θ. The latter one ensures the causality, by setting the Green's function to zero when t' is bigger than t. Because of this property we refer to the operator (A.10) as *retarded* Green's function. Again notice that we have expressed the response of the system through the description of the internal degrees of freedom, which results independent on the strength of the perturbation $f(t)$.

A.2 One-particle Green's functions

In the present thesis much attention is dedicated to the one-particle Green's function or propagator. With respect to the definitions of the previous Section, the one-particle Green's function is obtained by choosing the observable $\hat{O}$ and the perturbation $\hat{V}_0$ to be respectively the annihilation and creation field operators $\hat{\psi}(\mathbf{r}, t)$ and $\hat{\psi}^\dagger(\mathbf{r}, t)$[1]. Notice that, instead of working in a generic Hilbert space, we have adopted the position representation. From now on we assume $\hbar = 1$, as usually found in standard textbooks. With these prescriptions we can write down the following two Green's functions:

$$G^R(\mathbf{r}, t; \mathbf{r}', t') \equiv -i \left\langle [\hat{\psi}(\mathbf{r}, t), \hat{\psi}^\dagger(\mathbf{r}', t')]_\mp \right\rangle \Theta(t - t') \tag{A.11}$$

$$G^A(\mathbf{r}, t; \mathbf{r}', t') \equiv +i \left\langle [\hat{\psi}(\mathbf{r}, t), \hat{\psi}^\dagger(\mathbf{r}', t')]_\mp \right\rangle \Theta(t' - t) \tag{A.12}$$

The first function G^R is the retarded single-particle Green's function. It describes the dynamics of a single particle added to the system, i.e. the probability that the particle created in $\mathbf{r}'$ at t' is destroyed in $\mathbf{r}$ at t. The symbol $[A, B]_\mp$ indicates the commutator for bosons and the anti-commutator for fermions, and it is introduced to ensure the correct symmetries with respect to the exchange of two particles. The second function G^A is the advanced single-particle Green's function, and is analogous to G^R, but for a physical world whose time runs backwards.

---

[1]We wrote them already in the Heisenberg picture, without the bar, for simplifying the notation.

Let us consider a quantum system described by a Hamiltonian $\hat{H}$ that does not depend on the time t, and let us neglect all the other external terms. In such a case the retarded Green's function (A.11) depends only on the difference $t - t'$, so we can consider $t' = 0$ without losing generality. Intuitively it is convenient to consider the Fourier transform

$$G^R(\mathbf{r}, \mathbf{r}'; \omega) \equiv \int_{-\infty}^{+\infty} dt\, e^{i\omega t} G^R(\mathbf{r}, \mathbf{r}'; t). \tag{A.13}$$

It easy to realize that the integral in equation (A.13) is not well-defined, unless the retarded Green's function decays with t. To obtain the correct analytical properties we extend the domain of ω in the complex plane $\mathbb{C}$. Now we can introduce an infinitesimal imaginary part $i\delta$ to ensure the converge of the integral (A.13), and the "physical" Fourier transform is recovered through the limit

$$G^R(\mathbf{r}, \mathbf{r}'; \omega) = \lim_{\delta \to +0} G^R(\mathbf{r}, \mathbf{r}'; \omega + i\delta). \tag{A.14}$$

If we consider a basis $\{|m\rangle\}$ of eigenvectors of $\hat{H}$ and corresponding to the eigenvalues E_m, we can calculate the expectation value in the Green's function on the grand-canonical ensemble. With some algebra we can rewrite the equation (A.13) as

$$G^R(\mathbf{r}, \mathbf{r}'; \omega) = \int_{-\infty}^{+\infty} d\omega' \frac{A(\mathbf{r}, \mathbf{r}'; \omega')}{\omega - \omega'}, \tag{A.15}$$

where we have introduced the spectral density[2]

$$A(\mathbf{r}, \mathbf{r}'; \omega') = \frac{1}{Z} \sum_{n,m} \langle n|\hat{\psi}(\mathbf{r})|m\rangle \langle m|\hat{\psi}^\dagger(\mathbf{r}')|n\rangle \cdot$$
$$\cdot \left(e^{-\beta E_n} \mp e^{-\beta E_m} \right) \delta(\omega' - E_m + E_n). \tag{A.16}$$

In the expressions above Z is the grand-canonical partition function, and all the energies are defined with respect to the chemical potential μ, so that the latter one does not appear explicitly. The equation (A.15) is known as Lehmann representation[3] and has the advantage of isolating the dependence on ω, which appears exclusively in the denominator. As a result the analytical properties of $G^R(\mathbf{r}, \mathbf{r}'; \omega)$ can be studied in the most general way. This fact can be seen by calculating the Fourier transform $G^A(\mathbf{r}, \mathbf{r}'; \omega)$ of the advanced Green's function $G^A(\mathbf{r}, \mathbf{r}'; t)$, which results to have exactly the same expression (A.15). In fact the two Fourier transforms are equivalent, so usually the superscripts are neglected. The only difference

---

[2] If the operators involved in the definition of the Green's function are not hermitian conjugates, we usually speak of spectral function.

[3] In mathematics the name "Hilbert transform" is also used.

relies in the way of considering the limit that ensures the integrability of equation (A.13), i.e.:

$$G^A(\mathbf{r}, \mathbf{r}'; \omega) = \lim_{\delta \to +0} G^A(\mathbf{r}, \mathbf{r}'; \omega - i\delta). \tag{A.17}$$

Then we have only one $G(\mathbf{r}, \mathbf{r}'; \omega)$ that is analytical in the upper and lower half-planes of $\mathbb{C}$ and satisfies equations (A.14) and (A.17). In presence of continuous spectrum along the real-axis we have a so-called branch-cut. The real part of $G(\mathbf{r}, \mathbf{r}'; \omega)$ is continuous across the branch cut, while the imaginary part presents a discontinuity. It can be easily shown that such a discontinuity is proportional to the spectral function:

$$G^R(\mathbf{r}, \mathbf{r}'; \omega) - G^A(\mathbf{r}, \mathbf{r}'; \omega) = -2\pi i A(\mathbf{r}, \mathbf{r}'; \omega) \tag{A.18}$$

In case of discrete spectrum we have a collection of simple poles instead of the branch-cut. In this picture the infinitesimal imaginary part $\pm i\delta$ moves the poles far from the real axis of ω, and a proper contour of integration can be chosen in the complex plane.

Now we can focus on the spectral density, which contains all the information about the single-particle excitations. Given that this thesis is dedicated to crystal structures, we consider systems that are invariant under spatial translations. It is easier to work in $\mathbf{k}$-space, so the field operators at $t = 0$ can be transformed as

$$\hat{\psi}(\mathbf{r}) = \frac{1}{\sqrt{V}} \sum_{\mathbf{k}} e^{i\mathbf{k}\mathbf{r}} \hat{c}_{\mathbf{k}} \qquad \hat{\psi}^\dagger(\mathbf{r}) = \frac{1}{\sqrt{V}} \sum_{\mathbf{k}} e^{-i\mathbf{k}\mathbf{r}} \hat{c}_{\mathbf{k}}^\dagger, \tag{A.19}$$

where V is the volume, and $\hat{c}_{\mathbf{k}}$ and $\hat{c}_{\mathbf{k}}^\dagger$ are respectively the annihilation and creation operators for the electron quasi-momentum $\mathbf{k}$. Using these expressions in Green's functions (A.11) and (A.12), we obtain that

$$G^{R,A}(\mathbf{r}, t; \mathbf{r}', t') = \frac{1}{V} \sum_{\mathbf{k}} e^{i\mathbf{k}(\mathbf{r}-\mathbf{r}')} G^{R,A}(\mathbf{k}; t, t') \tag{A.20}$$

where

$$G^R(\mathbf{k}; t, t') \equiv -i \langle [\hat{c}_{\mathbf{k}}(t), \hat{c}_{\mathbf{k}}^\dagger(t')]_{\mp} \rangle \, \Theta(t - t') \tag{A.21}$$

$$G^A(\mathbf{k}; t, t') \equiv +i \langle [\hat{c}_{\mathbf{k}}(t), \hat{c}_{\mathbf{k}}^\dagger(t')]_{\mp} \rangle \, \Theta(t' - t) \tag{A.22}$$

are the one-particle Green's functions in $\mathbf{k}$-space. All the previous results and definitions have a straightforward generalization to the $\mathbf{k}$-space, since we just made a change of representation. In particular we consider the spectral density for the limit $T \to 0$. In this case the ground-state energy E_0 dominates in the exponentials that are present in the partition function and in the sums. Then we can obtain

$$A(\mathbf{k}, \omega') \simeq \sum_n |\langle n|\hat{c}_{\mathbf{k}}|0\rangle|^2 \delta(\omega' + E_n - E_0) +$$

$$\mp \sum_n |\langle n|\hat{c}_{\mathbf{k}}^\dagger|0\rangle|^2 \delta(\omega' - E_n + E_0). \tag{A.23}$$

The first term corresponds to processes where one particle with momentum $\mathbf{k}$ is added to the ground-state, resulting in a contribution for positive frequencies (with respect to μ). The second term represent processes where one particle with momentum $\mathbf{k}$ is removed from the ground-state, and brings a contribution for negative frequencies. Then we have obtained a description of the single-particle excitations that govern the behavior of the quantum system. Since the Green's function contains this information, it is clear that the most important physical observables can be reconstructed from it.

Finally we should mention that from the spectral density we can recover the well-known density of states as sum over the momentum:

$$D(\omega) = \sum_{\mathbf{k}} A(\mathbf{k}, \omega). \tag{A.24}$$

A.3   Matsubara formalism

The retarded and advanced single-particle Green's functions are particularly important for studying the response of a system to an external probe. However, for the pure scope of exploring the inner dynamics, the temperature Green's function G^T is the most fundamental quantity:

$$G^T(\mathbf{r}, \tau; \mathbf{r}', \tau') \equiv -\left\langle \mathcal{T} \hat{\psi}(\mathbf{r}, \tau) \hat{\psi}^\dagger(\mathbf{r}', \tau') \right\rangle. \tag{A.25}$$

Formally it is defined by introducing the so-called imaginary time τ such as $t = -i\tau$. The Dyson time-ordering superoperator $\mathcal{T}$ acts on a generic set of operators $A_i(\tau_i)$, by ordering them for decreasing times:

$$\mathcal{T}[A_1(\tau_1)A_2(\tau_2)\ldots A_N(\tau_N)] = (\pm 1)^P A_{i_1}(\tau_{i_1})A_{i_2}(\tau_{i_2})\ldots A_{i_N}(\tau_{i_N})$$

where

$$\tau_{i_1} > \tau_{i_2} > \ldots \tau_{i_N}.$$

The factor $(\pm 1)^P$ depends on the number of needed permutations P and preserves the correct symmetry for the exchange of particles. The aim of such a construction is the definition of a quantity with the same spectral properties as before. Once that the imaginary time has been introduced, we can easily show that

$$G^T(\mathbf{r}, \mathbf{r}'; \tau - \beta) = \pm G^T(\mathbf{r}, \mathbf{r}'; \tau) \tag{A.26}$$

if $\tau \in]0, \beta]$. This means that in the interval $]-\beta, +\beta]$ the thermal Green's functions for bosons is periodic in the imaginary-time with a period β. On the other hand for fermions the Green's function is anti-periodic with a period β. Consequently we can restrict the domain of our function to $]-\beta, +\beta]$, and make an expansion in Fourier series:

$$G^T(\mathbf{r}, \mathbf{r}'; \tau) = \frac{1}{\beta} \sum_{\omega_n} e^{-i\omega_n \tau} G^T(\mathbf{r}, \mathbf{r}'; i\omega_n). \tag{A.27}$$

The frequencies ω_n are named Matsubara frequencies and depend on the character of the periodicity:

$$\omega_n = \frac{2n\pi}{\beta} \qquad\qquad\qquad \text{bosons} \qquad\qquad (A.28)$$

$$\omega_n = \frac{2n\pi}{\beta} + \frac{\pi}{\beta} \qquad\qquad\qquad \text{fermions} \qquad\qquad (A.29)$$

In this framework an expression for the inverse Fourier transform is given by the Fourier coefficients in the equation (A.27), that is:

$$G^T(\mathbf{r}, \mathbf{r}'; \omega_n) = \frac{1}{\beta} \int_0^\beta d\tau e^{i\omega_n \tau} G^T(\mathbf{r}, \mathbf{r}'; \tau). \qquad\qquad (A.30)$$

The next step consists in writing down the Lehmann representation of the thermal Green's function:

$$G^T(\mathbf{r}, \mathbf{r}'; i\omega_n) = \int_{-\infty}^{+\infty} d\omega' \frac{A(\mathbf{r}, \mathbf{r}'; \omega')}{i\omega_n - \omega'} \qquad\qquad (A.31)$$

where the spectral density has again the same expression as equation (A.16). Once more then, we can see that the Fourier transform leads to the same spectral density: the only difference is that now the Green's function is evaluated at imaginary frequencies, which implies a totally different analytical structure. However this structure is embedded in the Lehmann representation, and it is possible to show that there is only one Green's function defined in the whole complex plane and corresponding to the Fourier transforms of the advanced, retarded, and thermal Green's functions. Then in the present thesis we use only one symbol to indicate the Green's function, and we drop the superscripts. While this is justified when working with frequency-dependent quantities, we must consider that in time domain these functions are different. Fortunately the type of Green's function can be always understood from the context, or from the corresponding text.

The thermal Green's function is the basis for the Baym-Kadanoff perturbation theory[4]. Let us consider a system of Hamiltonian $\hat{H} = \hat{H}_0 + \hat{V}$, where $\hat{V}$ can be a two-particle interaction term, e.g. the one in equation (2.2). Now we can consider two Green's functions: the one associated to the unperturbed problem, i.e. G_0, which we suppose to know, and the one associated to the full problem, G, which we want to determine. If we take the imaginary-time derivative of both sides of equation (A.25) for the full Green's functions, we obtain the so-called Dyson

---

[4]The perturbation theory can also be formulated directly for real times at zero temperature. In this case we work with the causal Green's function, but some important contributions can be missed. Therefore it is usually preferred to work with the thermal Green's function and then consider the limit for $T \to 0$.

equation:

$$\left[-\frac{\partial}{\partial\tau} - H_0(\mathbf{r},\tau)\right]G(\mathbf{r},\tau;\mathbf{r}',\tau') = \delta(\mathbf{r}-\mathbf{r}')\delta(\tau-\tau') +$$
$$+ \int_{-\infty}^{+\infty} d\tau'' \int d\mathbf{r}'' \Sigma(\mathbf{r},\tau;\mathbf{r}'',\tau'')G(\mathbf{r}'',\tau'';\mathbf{r}',\tau') \quad \text{(A.32)}$$

where we have introduced the self-energy Σ, which contains all the effects of the interactions. In general the self-energy is a complex function, and can be expressed as a functional of the full Green's function G *only*; as a result it possesses the same analytical properties. Here we do not write any explicit expression for Σ, since it is beyond the scope of this short Appendix. Anyway it must be mentioned that the definition of the self-energy is only formal, and the same structure of equation (A.32) tells us that it must comprehend all the possible scattering events generated by the potential. In practical terms one or more classes of processes (or Feynman diagrams) are considered, so that approximate expressions can be obtained.

Finally if we move to the frequency domain and compare the equation (A.32) with the corresponding one for G_0, we can obtain the more elegant form:

$$G^{-1}(\mathbf{r},\mathbf{r}';\omega_n) = G_0^{-1}(\mathbf{r},\mathbf{r}';\omega_n) - \Sigma(\mathbf{r},\mathbf{r}';\omega_n). \quad \text{(A.33)}$$

All the reminders to the Dyson equation found in the present thesis are usually referred to the equation (A.33). From the latter form it is easier to understand how real and imaginary part of Σ act on the unperturbed excitation energies. This issue has been analyzed in detail in Chapter 4 in the context of the discussion of correlation effects in itinerant ferromagnets.

Appendix B

Constrained LDA method

It is useful to give a brief description of one of the main methods to calculate the average Hubbard U, i.e., the constrained LDA method [56, 60, 58, 68].

   Let us consider a multiband Hubbard model, whose Hamiltonian has the form of equation (2.28). For simplicity we limit our discussion to the orbital degrees of freedom, neglecting the spins. The problem is to find the connection between the model Hamiltonian and the *ab initio* DFT-LDA description. The hopping parameters can be easily obtained, for example, in a tight-binding representation of the one-particle Hamiltonian, as in equation (2.31). Conversely the calculation of local Coulomb repulsion U is not as simple as it can appear. Following Herring's definition [240], the average Coulomb repulsion can be expressed as the energy cost of the reaction $2(3d^n) \rightarrow 3d^{n-1} + 3d^{n+1}$. It is obvious that the evaluation of the expectation value of the bare Coulomb potential on the single-particle wave-functions would neglect the screening of the other non-localized electrons, which is shown in Figure B.1(a). The idea of the constrained LDA method is to consider a supercell of the lattice and to decouple the localized orbitals of a given site, by setting their hopping matrix elements towards the other electrons to zero, as schematized in Figure B.1(b). Then for a given number of localized electrons n the total energy of the system can be calculated with DFT-LDA, leading to the energy landscape $E(n)$. The localized electrons cannot move from the chosen atom, but all the other electrons are free to move, so to screen the additional charge. If the total energy of the defined model is evaluated [88, 68] in the Hartree-Fock approximation[1], we recover the definition of average screened Coulomb repulsion of Herring:

$$U = E(n+1) + E(n-1) - 2E(n). \tag{B.1}$$

This expression can be further simplified if one uses the so-called Slater-Janak

---

[1]In addition to the spin, we also neglect the exchange energy and the non sphericity of the Hartree contribution. In fact these details are completely unimportant with respect to our description, while they must be included in practical applications for real materials
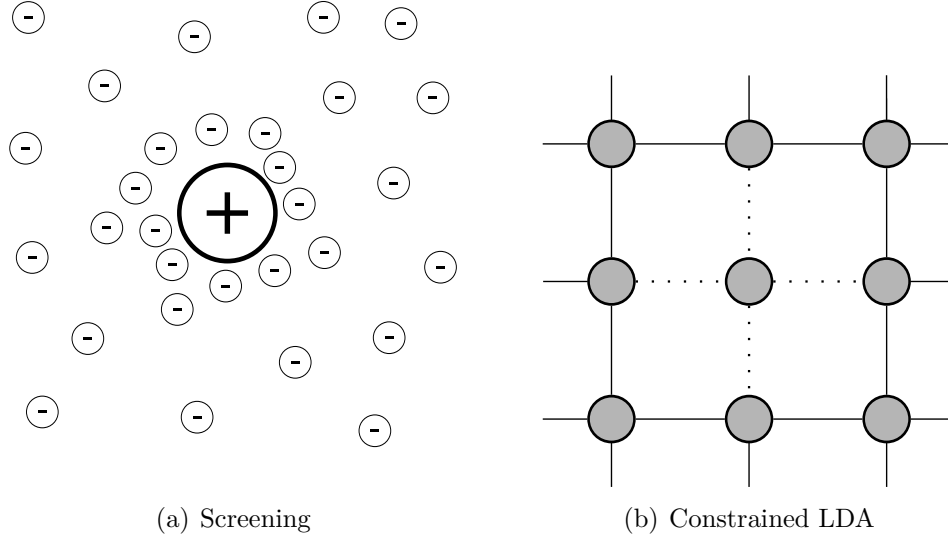
(a) Screening   (b) Constrained LDA

Figure B.1: Left: the electrons in a box rearrange to screen an external positive charge. Right: in constrained LDA the correlated electrons at a given site are decoupled from the rest of the lattice.

theorem [44] that relates the total energies in DFT-LDA directly to the Kohn-Sham eigenvalues:

$$\varepsilon_i = \frac{\partial E}{\partial n_i}. \tag{B.2}$$

Then, knowing approximately the value of n, the average effective Coulomb repulsion between the localized electrons can be related to the shift of the eigenvalues of the correlated orbitals:

$$U = \varepsilon(n + \frac{1}{2}) - \varepsilon(n - \frac{1}{2}). \tag{B.3}$$

This quantity can be calculated with high precision in modern DFT-LDA codes, and the procedure can be easily tested by increasing the size of the supercell until U converges to a well defined value.

The constrained LDA method and the successes of the model Hamiltonians obtained from it emphasize the following point: one obtains good results when manipulating the total energies within some well-defined scheme, but as soon as he starts using the Kohn-Sham energies all the deficiencies of the single-particle approach become evident. This is not surprising, given that these energies are barely Lagrange multipliers arising from the minimization problem.

Summary

The present thesis has been dedicated to the application of different theoretical methods to the electronic structure of strongly correlated systems, and in particular the transition metals and their compounds. These materials possess electrons in narrow bands, which tend to be localized around the atoms, resulting into strong electron-electron Coulomb repulsions. Consequently they cannot be described by means of the state-of-the-art technique for electronic structure calculation, i.e. the density-functional theory in local density approximation (DFT-LDA), but require a method that goes beyond the single-particle approach. In the last decade the dynamical mean-field theory (DMFT) has been introduced and successfully applied to the study of the Hubbard model and other periodic models. Most importantly, in our perspective, it can be combined to the DFT-LDA, and the resulting LDA+DMFT scheme is at the present day the most accurate *ab initio* computational technique for strongly correlated systems.

The work presented in this thesis can be divided into three parts. The first part, which comprehends Chapters 1 and 2, is focused on the basic concepts and ideas related to the study of strongly correlated materials. In Chapter 1 the Hubbard model is introduced for lattice systems with localized electrons, and a brief historical overview of the LDA+DMFT scheme is illustrated. In Chapter 2 the emphasis is moved on the theoretical methods. The DFT-LDA is presented in detail, and a special attention is dedicated to its failures for narrow bands systems. The last two Sections concern the basic equations of the DMFT, and the definitions and justifications of the LDA+DMFT scheme.

The second part of this thesis is centered on the technical details related to our implementation of the LDA+DMFT scheme, and consists uniquely of Chapter 3. First the full-potential linear muffin-tin orbital (FP-LMTO) method, which is the band structure method used in the merging between DMFT and DFT-LDA, is presented. Then follows a description of all the main equations used in the LDA+DMFT cycle, and a discussion of the main problematics related to our computational scheme: the "double counting" issue and the choice of the "solver". The work presented in this part resulted into a code that allows to study efficiently the many-body effects through LDA+DMFT in systems with many atoms per unit cell, and without limitations on the geometry of the problem.

The third and last part of this thesis (Chapters 4-9) concerns the results obtained by means of our developed code. In Chapter 4 we focus on the single-particle excitations of the bulk late transition metals: Fe, Co and Ni. While these systems can be considered as weakly correlated metals, still some important correlations effects are observed such as the shrinking of the $3d$ band and the formation of non-coherent satellites in the photoemission spectrum. A very successful comparison between our results, three-body scattering results and experimental data is presented for Co. In Chapter 5 our study is extended to the surfaces of Fe, Co and Ni, and comparison is made with the corresponding bulk systems, showing an increase of the correlation effects. At the end of the Chapter our calculations are compared to the experimental data from photoemission spectroscopy of Fe (110), and the role of non-local correlation effects (beyond DMFT) is emphasized. The following Chapter 6 concerns the narrowing of the pseudo-gap in the density of states of a mono-layer of Fe on the surface (001) of W. The presented experimental data from Scanning Tunneling Spectroscopy (STS) cannot be explained in terms of DFT-LDA, but are shown to be in reasonable agreement with our LDA+DMFT results. A qualitative interpretation of this phenomenon is provided in terms of a mean-field theory. Then, in Chapter 7, the theoretical framework needed for total energy calculation in the LDA+DMFT scheme is presented, and the implementation of an effective total energy functional is described in details. Results for ferromagnetic Ni and antiferromagnetic γ-Mn are reported, and for the latter a big improvement can be observed with respect to bare DFT-LDA. γ-Mn is also the object of Chapter 8, where the dependence of the LDA+DMFT results on the magnetic phase and on the solver is studied. Moreover the possibility of a combination of the LDA+DMFT scheme and the disordered local moment (DLM) approach is presented, together with an application to the photoemission spectrum within the one-step model. Our simulations show that γ-Mn is a very interesting element, being right at the border between the regimes of strong and weak correlations. Finally Chapter 9 is focused on the limit of very strong correlations: the mixed-valence compounds SmB_6, YbB_{12} and $YbInCu_4$ are studied within the Hubbard I approximation, which can be interpreted as a type of solver in the LDA+DMFT framework. The spectrum clearly shows the formation of multiplets, that cannot be described in one-particle approaches, but are perfectly reproduced in our computational scheme.

Samenvatting

Dit proefschrift beschrijft verschillende theoretische methodes voor de berekening van de elektronen structuur van materialen waarin elektron correlatie een grote rol speelt. Dit zijn met name de overgangsmetalen en hun verbindingen. Deze materialen worden gekenmerkt door nauwe banden, wat duidt op een sterke lokalisatie van de elektronen nabij de atoom kernen, met als gevolg een sterke elektron-elektron repulsie via de Coulomb interactie. Sate-of-the-art technieken, i.e. dichtheids functionaal methoden in de locale dichtheids benadering (DFT-LDA), zijn niet in staat deze interactie goed te beschrijven. Een aanpak voorbij de één-deeltje benadering is nodig. In het afgelopen decennium is de dynamische gemiddelde-veld theorie (DMFT) ontwikkeld en toegepast op het Hubbard model en andere periodieke modellen. Voor dit proefschrift van belang is dat deze methode gecombineerd kan worden met de DFT-LDA methode. De gecombineerde methode (LDA+DMFT) is, op dit moment, de meest nauwkeurige *ab initio* computationele methode voor het berekenen van sterk gecorreleerde systemen.

Het werk in dit proefschrift bestaat uit drie delen. Het eerste deel, dat bestaat uit hoofdstukken 1 en 2, beschrijft de basis begrippen die nodig zijn voor het bestuderen van gecorreleerde materialen. In hoofdstuk 1 wordt het Hubbard model geïntroduceerd voor rooster systemen met gelokaliseerde elektronen. Ook wordt een kort historisch overzicht gegeven van het ontstaan van de LDA+DMFT methode. In hoofdstuk 2 ligt de nadruk op theoretische methodes. Een gedetailleerde beschrijving van DFT-LDA wordt gegeven, en het falen van deze methode voor systemen met nauwe banden wordt onder de loep genomen. De laatste twee paragrafen geven de basis vergelijkingen van DMFT. Tenslotte wordt de LDA+DMFT methode gedefinieerd en besproken.

Het tweede deel van dit proefschrift richt zich op de technische details van onze implementatie van de LDA+DMFT methode, en beslaat hoofdstuk 3. Eerst wordt de volledige-potentiaal muffin-tin orbitaal (FP-LMTO) methode gegeven. Deze methode wordt gebruikt om DMFT en DFT-LDA te kunnen combineren. Vervolgens komen de belangrijkste vergelijkingen uit de LDA+DMFT cyclus en worden de belangrijkste problemen, het "dubbel tellen" en de keuze van de "solver", besproken. Het werk in dit hoofdstuk is geimplementeerd in een programma dat een efficiënte berekening van veel-deeltjes effecten in systemen met een groot aantal

atomen per eenheidscel mogelijk maakt, dit te doen zonder beperkingen op te leggen aan de geometrie van het probleem.

Het derde, en laatste, deel van dit proefschrift (hoofdstukken 4-9) bevat nieuwe resultaten verkregen met het ontwikkelde programma. In hoofdstuk 4 richten we ons op de één-deeltje aangeslagen toestanden van de latere overgangsmetalen: ijzer (Fe), cobalt (Co) en nikkel (Ni). Hoewel deze metalen over het algemeen niet beschouwd worden als sterk gecorreleerde materialen, worden er toch een paar belangrijke correlatie effecten een waargenomen. Bijvoorbeeld het vernauwen van de 3d band en de vorming van niet samenhangende satellieten in het foto emissie spectrum. Een erg succesvolle vergelijking tussen onze resultaten, drie deeltjes verstrooiing en experimentele data wordt gegeven voor kobalt. In hoofdstuk 5 wordt ons onderzoek uitgebreid naar oppervlakken van ijzer, kobalt en nikkel; een vergelijking met de bulk laat zien dat correlatie effecten zijn toegenomen. Het hoofdstuk eindigt met vergelijking van onze berekeningen met het foto emissie spectrum van het ijzer (110) oppervlak. Het belang van de niet locale correlatie effecten (welke dus niet goed beschreven worden door DMFT) wordt benadrukt. Het volgende hoofdstuk, hoofdstuk 6, bespreekt het vernauwen van de pseudo band-gap in de toestandsdichtheid van een monolaag ijzer op een (001) oppervlak van wolfraam (W). Experimentele data, verkregen door middel van scanning tunneling spectroscopy (STS), kan niet verklaard worden door DFT-LDA maar blijkt redelijk overeen te stemmen met onze LDA+DMFT berekeningen. Een kwalitatieve interpretatie van dit fenomeen wordt gegeven door de gemiddeld-veld theorie. Vervolgens, in hoofdstuk 7, wordt het theoretische raamwerk nodig voor het berekenen van de totale energie in een LDA+DMFT methode opgebouwd. Ook de noodzakelijke details voor een implementatie van een effectieve totale energie functionaal worden gegeven. Ferromagnetisch nikkel en antiferromagnetisch γ-Mn worden berekend. Antiferromagnetisch γ-Mn laat een grote verbetering zien ten opzichte van DFT-LDA, en wordt verder bestudeerd in hoofdstuk 8. De afhankelijkheid van de LDA+DMFT resultaten van de magnetische fase en de gebruikte solver wordt onderzocht. Bovendien worden de mogelijkheden om de LDA+DMFT methode te combineren met de ongeordende locale momenten (DLM) benadering, alsook een toepassing op het foto emissie spectrum binnen het one-step model, uitgewerkt. De berekeningen laten zien dat γ-Mn een interessante positie in neemt op de grens tussen sterke en zwakke correlatie. Hoofdstuk 9 tenslotte onderzoekt de limiet van erg sterke correlaties. De gemengde valentie materialen SmB_6, YbB_{12} en $YbInCu_4$ worden onderzocht vanuit de Hubbard I benadering, die beschouwd kan worden als een specifieke solver in onze LDA+DMFT methode. Het spectrum laat duidelijk de vorming van multiplets zien. Deze multiplets kunnen niet beschreven worden in een één-deeltjes benadering, maar worden foutloos beschreven door onze aanpak.

Publications

This thesis is based on the following scientific articles:

1. J. Sánchez-Barriga, J. Fink, V. Boni, I. Di Marco, J. Braun, J. Minár, A. Varykhalov, O. Rader, H. A. Dürr, V. Bellini, F. Manghi, H. Ebert, A. I. Lichtenstein, M. I. Katsnelson, O. Eriksson and W. Eberhardt "Quantitative determination of spin-dependent quasi-particle life-times and electronic correlations in hcp Co", *in preparation for Phys. Rev. Lett.*

2. J. Sánchez-Barriga, J. Fink, V. Boni, I. Di Marco, J. Braun, J. Minár, A. Varykhalov, O. Rader, H. A. Dürr, V. Bellini, F. Manghi, H. Ebert, A. I. Lichtenstein, M. I. Katsnelson, O. Eriksson and W. Eberhardt "About the correlation effects in the spin-dependent electronic structure of Fe", *in preparation for Phys. Rev. Lett.*

3. A. Kubetzka, I. Di Marco, M. Bode, M. Menzel, K. von Bergmann, S. Heinze, P. Ferriani, M. I. Katsnelson, A. I. Lichtenstein and R. Wiesendanger "Narrowing of the pseudogap at the Fermi level for antiferromagnetic Fe layer on W(001) surface", *in preparation for Nature Materials*

4. I. Di Marco, J. Minár, J. Braun, M. I. Katsnelson, H. Ebert, A. I. Lichtenstein, O. Eriksson, "γ-Mn at the border between weak and strong correlations", *submitted to Eur. Phys. Lett.*

5. P. Thunström, I. Di Marco, A. Grechnev, S. Lebègue, M. I. Katsnelson, A. Svane, and O. Eriksson "Multiplet effects in electronic structure of intermediate valence compounds", *Phys. Rev. B* **79**, 165104 (2009)

6. I. Di Marco, J. Minár, S. Chadov, M. I. Katsnelson, H. Ebert, and A. I. Lichtenstein "Correlation effects in the total energy, the bulk modulus, and the lattice constant of a transition metal: Combined local-density approximation and dynamical mean-field theory applied to Ni and Mn", *Phys. Rev. B* **79**, 115111 (2009)

7. A. Grechnev, I. Di Marco, M. I. Katsnelson, A. I. Lichtenstein, J. Wills, and O. Eriksson "Theory of bulk and surface quasiparticle spectra for Fe, Co, and Ni", *Phys. Rev. B* **76**, 035107 (2007)

Curriculum Vitae

Personal Information

Full name	Igor Di Marco
Born	24 April 1978 in Teramo (Italy)
Citizenship	Italian

Education

1997 – 2003	"Laurea" 110/110 cum laude at the Department of Condensed Matter Physics, Universitá degli Studi di Pavia (Italy)
1992 – 1997	Scientific "Diploma" 60/60 for the Informatics National Program at Scientific Lycaeum A. Einstein, Teramo (Italy)

Work Experience

2008 – present	Visiting Researcher at Uppsala University (Sweden)
2004 – 2008	PhD student in Theory of Condensed Matter, Radboud University Nijmegen (the Netherlands)
2005 – 2007	Teaching assistant for the courses *Modern Classical Dynamics* and *Condensed Matter Theory*, Radboud University Nijmegen (the Netherlands)

Acknowledgments

Finally I have reached the end. The committee has approved my manuscript, and I have done my best to produce a good layout for this thesis. To be honest, I never thought I could make it. When I started, almost five years ago, I had absolutely no idea what *doing research* meant, and I cannot say that my first two years were exceptionally productive. I am the only person to blame: bad research methodology, too many distractions at work and too many parties. Or maybe it is just the tough training needed in science. It is a matter of different points of view. What is important is that after two years I found my path, and I will always be grateful to Alexei, who has been my "spark". Russian education for me. Long sessions of explanations and questions, and a lot of swear words. After having heard so much about my stupidity, I cannot really describe my happiness at his first positive remark. Probably one of the greatest satisfactions of my life.

Obviously all this work would not have been possible without the guidance of my supervisor Misha. Despite all his duties and travelling he always found time to dedicate to my research, and supported me in many scientific collaborations. In particular his close activity with Sasha gave me the opportunity to work with two scientists whose scientific rigor and passion are an example I would like to follow in my future career.

I am really indebted to the research groups which hosted me during the last four years. First of all the group of Hubert, in Munich. The collaboration with Jan has been the most fruitful of my PhD, and his experience in *discussing experiments with experimentalists* has really helped me a lot. Thanks Jan! Then I have to thank all the people of Uppsala, *in primis* Olle with his enthusiasm for new ideas and his deep understanding of everything. Naturally I cannot forget my Swedish officemates: Oscar, who tried to make me insane with δ-Pu, and Patrik "the seer" Thunström, who has been teaching me how to think deeply. Thanks, guys, I have learned a lot from you, and I hope that I will learn still more in the future!

Life is not only made of work, therefore I express my gratitude to all the people I met in Nijmegen during these last few years. All my colleagues Annalisa, Leonya, Astrid, and especially Oksana and Kostya, who gave me the fantastic adventure of attending a Russian wedding and have helped me so much in preparing this thesis. Surely special thanks go to all my housemates Jisk, Elena, Ichiro, Benedicte,

Irene and Marc for their patience in putting up with my madness and persecution manias. Please forgive me if sometimes I have been a little bit too rude and dictatorial.

Finally I would like to give a big hug to Flavio and "magneto" Miguel, i.e. the friends who guided me into the night life of Nijmegen, Amsterdam, Utrecht, Zercé, Stockholm, Paris, and more (when Buenos Aires?). I hope I have learned enough from your lessons in Bascafé. Constant application and perseverance always give rewards in the *work*. And speaking about *work*, how could I forget the indubitable master Diego della Torre?

Last but not least I would like to express my gratitude to all the other people that I met during this, my first experience in a foreign country. Those people are too many to be mentioned here. However I must make an exception for Petra, Nathalie and Anouk. Three muses who have filled my life in Nijmegen with enthusiasm and inspiration, light and pleasant darkness.

Do I forget something? Yes, I do.

Un ringraziamento speciale per i miei genitori e per la mia sorellina. Senza il loro supporto non avrei mai avuto la forza di portare a termine questa avventura. Non posso fare a meno di concludere questo testo con un abbraccio a mio padre ed un bacione alla mamma.

Bibliography

[1] P. HOHENBERG and W. KOHN, *Phys. Rev.* **136**, B864 (1964).

[2] W. KOHN and L. SHAM, *Phys. Rev.* **140**, A1133 (1965).

[3] O. JONES and O. GUNNARSSON, *Rev. Mod. Phys.* **61**, 689 (1989).

[4] A. GEORGES, Strongly Correlated Electron Materials: Dynamical Mean-Field Theory and Electronic Structure, volume 715, pp. 3–74, AIP, 2004.

[5] K. HELD, *Advances in Physics* **56**, 829 (2007).

[6] J. HUBBARD, *Proc. Roy. Soc.* **A 276**, 238 (1963).

[7] J. HUBBARD, *Proc. Roy. Soc.* **A 277**, 237 (1964).

[8] J. HUBBARD, *Proc. Roy. Soc.* **A 281**, 401 (1964).

[9] N. F. MOTT, *Proc. Phys. Soc. A* **62**, 416 (1949).

[10] N. F. MOTT, *Metal-insulator transitions*, Taylor and Francis, London, 1990.

[11] J. P. PERDEW and A. ZUNGER, *Phys. Rev. B* **23**, 5048 (1981).

[12] V. I. ANISIMOV, J. ZAANEN, and O. K. ANDERSEN, *Phys. Rev. B* **44**, 943 (1991).

[13] V. I. ANISIMOV, F. ARYASETIAWAN, and A. I. LICHTENSTEIN, *J. Phys.: Condens. Matter* **9**, 767 (1997).

[14] A. GEORGES, G. KOTLIAR, W. KRAUTH, and M. J. ROZENBERG, *Rev. Mod. Phys.* **68**, 13 (1996).

[15] G. KOTLIAR, S. SAVRASOV, K. HAULE, V. OUDOVENKO, O. PARCOLLET, and C. MARIANETTI, *Rev. Mod. Phys.* **78**, 865 (2006).

[16] P. W. ANDERSON, *Phys. Rev.* **124**, 41 (1961).

[17] V. Anisimov, A. Poteryaev, M. Korotin, A. Anokhin, and G. Kotliar, *J. Phys.: Condens. Matter* **9**, 7359 (1997).

[18] A. I. Lichtenstein and M. I. Katsnelson, *Phys. Rev. B* **57**, 6884 (1998).

[19] S. Y. Savrasov, G. Kotliar, and E. Abrahams, *Nature* **410**, 793 (2001).

[20] L. V. Pourovskii, M. I. Katsnelson, A. I. Lichtenstein, L. Havela, T. Gouder, F. Wastin, A. B. Shick, V. Drchal, and G. H. Lander, *Europhys. Lett.* **74**, 479 (2006).

[21] L. V. Pourovskii, G. Kotliar, M. I. Katsnelson, and A. I. Lichtenstein, *Phys. Rev. B* **75**, 235107 (2007).

[22] J. H. Shim, K. Haule, and G. Kotliar, *Nature* **446**, 513 (2007).

[23] C. A. Marianetti, K. Haule, G. Kotliar, and M. J. Fluss, *Physical Review Letters* **101**, 056403 (2008).

[24] K. Held, A. K. McMahan, and R. T. Scalettar, *Phys. Rev. Lett.* **87**, 276404 (2001).

[25] A. K. McMahan, K. Held, and R. T. Scalettar, *Phys. Rev. B* **67**, 075108 (2003).

[26] B. Amadon, S. Biermann, A. Georges, and F. Aryasetiawan, *Phys. Rev. Lett.* **96**, 066402 (2006).

[27] M. I. Katsnelson and A. I. Lichtenstein, *J. Phys.: Condens. Matter* **11**, 1037 (1999).

[28] A. I. Lichtenstein, M. I. Katsnelson, and G. Kotliar, *Phys. Rev. Lett.* **87**, 067205 (2001).

[29] J. Braun, J. Minár, H. Ebert, M. I. Katsnelson, and A. I. Lichtenstein, *Phys. Rev. Lett.* **97**, 227601 (2006).

[30] M. I. Katsnelson, V. Y. Irkhin, L. Chioncel, A. I. Lichtenstein, and R. A. de Groot, *Rev. Mod. Phys.* **80**, 315 (2008).

[31] L. Chioncel, Y. Sakuraba, E. Arrigoni, M. I. Katsnelson, M. Oogane, Y. Ando, T. Miyazaki, E. Burzo, and A. I. Lichtenstein, *Physical Review Letters* **100**, 086402 (2008).

[32] K. Held, G. Keller, V. Eyert, D. Vollhardt, and V. I. Anisimov, *Phys. Rev. Lett.* **86**, 5345 (2001).

[33] A. Liebsch and A. Lichtenstein, *Phys. Rev. Lett.* **84**, 1591 (2000).

[34] I. A. Nekrasov, Z. V. Pchelkina, G. Keller, T. Pruschke, K. Held, A. Krimmel, D. Vollhardt, and V. I. Anisimov, *Phys. Rev. B* **67** (2003).

[35] J. H. Shim, K. Haule, and G. Kotliar, *Science* **318**, 1615 (2007).

[36] J. Minár, L. Chioncel, A. Perlov, H. Ebert, M. I. Katsnelson, and A. I. Lichtenstein, *Phys. Rev. B* **72**, 045125 (2005).

[37] J. M. Wills, O. Eriksson, M. Alouani, and D. L. Price, Full-Potential LMTO Total Energy and Force Calculations, in *Electronic Structure and Physical Properties of Solids: the Uses of the LMTO method*, edited by H. Dreyssé, volume 535 of *Lecture Notes in Physics*, pp. 148–67, Springer-Verlag, Berlin, 2000.

[38] L. H. Thomas, *Proc. Cambridge Phil. Roy. Soc.* **23**, 542 (1927).

[39] E. Fermi, *Rend. Accad. Naz. Lincei* **6**, 602 (1927).

[40] P. A. M. Dirac, *Proc. Cambridge Phil. Roy. Soc.* **26**, 376 (1930).

[41] W. Kohn, *Highlights in Condensed Matter Theory*, North Holland, Amsterdam, 1985.

[42] M. Levy and J. P. Perdew, *Density Functional Methods in Physics*, p. 11, Plenum, New York, 1985.

[43] E. Lieb, *Density Functional Methods in Physics*, p. 111, Plenum, New York, 1985.

[44] R. M. Martin, *Electronic Structure: Basic Theory and Practical Methods*, Cambridge University Press, Cambridge, 2004.

[45] L. Hedin and B. I. Lundqvist, *J. Phys. C: Solid State Phys.* **4**, 2064 (1971).

[46] S. Vosko, L. Wilk, and M. Nusair, *Can. J. Phys.* **58**, 1200 (1980).

[47] D. M. Ceperley and B. J. Alder, *Phys. Rev. Lett.* **45**, 566 (1981).

[48] G. Ortiz and P. Ballone, *Phys. Rev. B* **50**, 1391 (1994).

[49] Y. Kwon, D. M. Ceperley, and R. M. Martin, *Phys. Rev. B* **58**, 6800 (1998).

[50] P. Gori-Giorgi, F. Sacchetti, and G. B. Bachelet, *Phys. Rev. B* **61**, 7353 (2000).

[51] O. Gunnarsson and B. I. Lundqvist, *Phys. Rev. B* **13**, 4274 (1976).

[52] J. Harris, *Phys. Rev. A* **29**, 1648 (1984).

[53] A. Svane and O. Gunnarsson, *Phys. Rev. Lett.* **65**, 1148 (1990).

[54] W. M. Temmerman, Z. Szotek, and H. Winter, *Phys. Rev. B* **47**, 11533 (1993).

[55] A. Svane, Z. Szotek, W. M. Temmerman, J. Lægsgaard, and H. Winter, *J. Phys.: Condens. Matter* **10**, 5309 (1998).

[56] P. H. Dederichs, S. Blügel, R. Zeller, and H. Akai, *Phys. Rev. Lett.* **53**, 2512 (1984).

[57] M. R. Norman and A. J. Freeman, *Phys. Rev. B* **33**, 8896 (1986).

[58] O. Gunnarsson, O. K. Andersen, O. Jepsen, and J. Zaanen, *Phys. Rev. B* **39**, 1708 (1989).

[59] O. Gunnarsson, J. W. Allen, O. Jepsen, T. Fujiwara, O. K. Andersen, C. G. Olsen, M. B. Maple, J.-S. Kang, L. Z. Liu, J.-H. Park, R. O. Anderson, W. P. Ellis, R. Liu, J. T. Markert, Y. Dalichaouch, Z.-X. Shen, P. A. P. Lindberg, B. O. Wells, D. S. Dessau, A. Borg, I. Lindau, and W. E. Spicer, *Phys. Rev. B* **41**, 4811 (1990).

[60] A. K. McMahan, R. M. Martin, and S. Satpathy, *Phys. Rev. B* **38**, 6650 (1988).

[61] S. Y. Savrasov and G. Kotliar, *Phys. Rev. B* **69**, 245101 (2004).

[62] V. I. Anisimov, D. E. Kondakov, A. V. Kozhevnikov, I. A. Nekrasov, Z. V. Pchelkina, J. W. Allen, S.-K. Mo, H.-D. Kim, P. Metcalf, S. Suga, A. Sekiyama, G. Keller, I. Leonov, X. Ren, and D. Vollhardt, *Phys. Rev. B* **71**, 125119 (2005).

[63] F. Lechermann, A. Georges, A. Poteryaev, S. Biermann, M. Posternak, A. Yamasaki, and O. K. Andersen, *Phys. Rev. B* **74**, 125120 (2006).

[64] O. K. Andersen and T. Saha-Dasgupta, *Phys. Rev. B* **62**, R16219 (2000).

[65] F. Aryasetiawan, M. Imada, A. Georges, G. Kotliar, S. Biermann, and A. I. Lichtenstein, *Phys. Rev. B* **70**, 195104 (2004).

[66] K. G. Wilson, *Rev. Mod. Phys.* **55**, 583 (1983).

[67] O. Gunnarsson, *Phys. Rev. B* **41**, 514 (1990).

[68] V. I. Anisimov and O. Gunnarsson, *Phys. Rev. B* **43**, 7570 (1991).

[69] A. M. Oles and G. Stollhoff, *Phys. Rev. B* **29**, 314 (1984).

[70] A. C. Hewson, *The Kondo Problem to Heavy Fermions*, Cambridge University Press, Cambridge, 1993.

[71] G. D. Mahan, *Many-Particle Physics*, Plenum Press, New York and London, 1993.

[72] A. L. Fetter and J. D. Walecka, *Quantum Theory of Many-Particle Systems*, McGraw-Hill, 1971.

[73] W. Metzner and D. Vollhardt, *Phys. Rev. Lett.* **62**, 324 (1989).

[74] A. Georges and G. Kotliar, *Phys. Rev. B* **45**, 6479 (1992).

[75] R. Fukuda, T. Kotani, Y. Suzuki, and S. Yokojima, *Prog. Theor. Phys.* **92**, 833 (1994).

[76] http://www.rspt.net.

[77] A. Grechnev, I. Di Marco, M. I. Katsnelson, A. I. Lichtenstein, J. Wills, and O. Eriksson, *Phys. Rev. B* **76**, 035107 (2007).

[78] M. I. Katsnelson and A. I. Lichtenstein, *Eur. Phys. J. B* **30**, 9 (2002).

[79] O. K. Andersen and R. V. Kasowski, *Phys. Rev. B* **4**, 1064 (1971).

[80] R. V. Kasowski and O. K. Andersen, *Solid State Commun.* **11**, 799 (1972).

[81] J. Korringa, *Physica* **13**, 392 (1947).

[82] W. Kohn and N. Rostocker, *Phys. Rev.* **94**, 1111 (1954).

[83] J. Kohanoff, *Electronic Structure Calculations for Solids and Molecules*, Cambridge University Press, 2006.

[84] O. K. Andersen, *Phys. Rev. B* **12**, 3060 (1975).

[85] H. L. Skriver, *The LMTO method: muffin-tin orbitals and electronic structure*, Springer, Berlin, 1984.

[86] L. Nordström, J. M. Wills, P. H. Andersson, and P. S. andO. Eriksson, *Phys. Rev. B* **63**, 035103 (2000).

[87] S. Chadov, *Application of Many-Body Perturbation Theory to the Description of Correlated Metals*, PhD thesis, Ludwig-Maximilians Universität München, 2007.

[88] I. V. Solovyev, P. H. Dederichs, and V. I. Anisimov, *Phys. Rev. B* **50**, 16861 (1994).

[89] M. T. Czyżyk and G. A. Sawatzky, *Phys. Rev. B* **49**, 14211 (1994).

[90] A. G. Petukhov, I. I. Mazin, L. Chioncel, and A. I. Lichtenstein, *Phys. Rev. B* **67**, 153106 (2003).

[91] M. Suzuki, S. Miyashita, and A. Kuroda, *Progress of Theoretical Physics* **58**, 1377 (1977).

[92] J. E. Hirsch, R. L. Sugar, D. J. Scalapino, and R. Blankenbecler, *Phys. Rev. B* **26**, 5033 (1982).

[93] J. E. Hirsch and R. M. Fye, *Phys. Rev. Lett.* **56**, 2521 (1986).

[94] A. N. Rubtsov, V. V. Savkin, and A. I. Lichtenstein, *Phys. Rev. B* **72**, 035122 (2005).

[95] P. Werner, A. Comanac, L. de' Medici, M. Troyer, and A. J. Millis, *Physical Review Letters* **97**, 076405 (2006).

[96] L. V. Pourovskii, M. I. Katsnelson, and A. I. Lichtenstein, *Phys. Rev. B* **72**, 115106 (2005).

[97] N. E. Bickers and D. J. Scalapino, *Annals of Physics* **193**, 206 (1989).

[98] M. Fleck, A. I. Liechtenstein, A. M. Oleś, L. Hedin, and V. I. Anisimov, *Phys. Rev. Lett.* **80**, 2393 (1998).

[99] V. Drchal, V. Janis, J. Kudrnovsky, V. S. Oudovenko, X. Dai, K. Haule, and G. Kotliar, *Journal of Physics: Condensed Matter* **17**, 61 (2005).

[100] V. Y. Irkhin and M. I. Katsnelson, *Journal of Physics: Condensed Matter* **2**, 7151 (1990).

[101] V. Y. Irkhin and M. I. Katsnelson, *Zh. Eksp. Teor. Fiz.* **88**, 522 (1985).

[102] V. Y. Irkhin and M. I. Katsnelson, *Sov. Phys. JETP* **61**, 306 (1985).

[103] S. Chadov, J. Minár, M. I. Katsnelson, H. Ebert, D. Ködderitzsch, and A. I. Lichtenstein, *Europhysics Letters* **82**, 37001 (2008).

[104] S. V. Vonsovsky and M. I. Katsnelson, *Quantum Solid State Physics*, Springer, Berlin, 1989.

[105] P. Nozieres, *Theory of Interacting Fermi Systems*, Benjamin, New York, 1964.

[106] A. B. Migdal, *Theory of Finite Fermi Systems and Applications to Atomic Nuclei*, Wiley, New York, 1967.

[107] S. V. Vonsovsky, M. I. Katsnelson, and A. V. Trefilov, *Phys. Metal. Metallography* **76**, 247 (1993), ibid. **76**, 343 (1993).

[108] D. Chandesris, J. Lecante, and Y. Petroff, *Phys. Rev. B* **27**, 2630 (1983).

[109] A. Gutierrez and M. F. Lopez, *Phys. Rev. B* **56**, 1111 (1997).

[110] C. Guillot, Y. Ballu, J. Paigne, J. Lecante, K. P. Jain, P. Thiry, R. Pinchaux, Y. Petroff, and L. M. Falicov, *Phys. Rev. Lett.* **39**, 1632 (1977).

[111] S. Hüfner, S.-H. Yang, B. S. Mun, C. S. Fadley, J. Schäfer, E. Rotenberg, and S. D. Kevan, *Phys. Rev. B* **61**, 12582 (2000).

[112] H. J. Vidberg and J. W. S. Solving, *J. Low Temp. Phys.* **29**, 179 (1977).

[113] S. Monastra, F. Manghi, C. A. Rozzi, C. Arcangeli, E. Wetli, H.-J. Neff, T. Greber, and J. Osterwalder, *Phys. Rev. Lett.* **88**, 236402 (2002).

[114] R. E. Kirby, E. Kisker, F. K. King, and E. L. Garwin, *Solid State Communications* **56**, 425 (1985).

[115] L. Chioncel, *Finite Temperature Electronic Structure: Beyond the Local Density Approximation*, PhD thesis, Radboud Universiteit Nijmegen, 2004, ISBN: 90-9018404-X.

[116] S. Biermann, A. Dallmeyer, C. Carbone, W. Eberhardt, C. Pampuch, O. Rader, M. I. Katsnelson, and A. I. Lichtenstein, *Pis'ma ZhETF* **80**, 714 (2004), [JETP Letters **80**, 614 (2004)].

[117] V. Boni, V. Bellini, and F. Manghi, 3BS Theory of Correlation effects in Co, Private Communication, 2009.

[118] C. Calandra and F. Manghi, *Phys. Rev. B* **50**, 2061 (1994).

[119] F. Manghi, V. Bellini, and C. Arcangeli, *Phys. Rev. B* **56**, 7149 (1997).

[120] J. Sánchez-Barriga, J. Fink, V. Boni, I. Di Marco, J. Braun, J. Minár, A. Varykhalov, O. Rader, H. A. Dürr, V. Bellini, F. Manghi, H. Ebert, A. I. Lichtenstein, M. I. Katsnelson, O. Eriksson, and W. Eberhardt, About the correlation effects in the spin-dependent electronic structure of Fe, Submitted to Phys. Rev. Lett.

[121] J. Schäfer, M. Hoinkis, E. Rotenberg, P. Blaha, and R. Claessen, *Phys. Rev. B* **72**, 155115 (2005).

[122] P. Ferriani, S. Heinze, G. Bihlmayer, and S. Bl′ugel, *Phys. Rev. B* **72**, 024452 (2005).

[123] L. M. Sandratskii, E. Şaşioğlu, and P. Bruno, *Phys. Rev. B* **73**, 014430 (2006).

[124] G. Bihlmayer, P. Ferriani, S. Baud, M. Ležaić, S. Heinze, and S. Blügel, Ultra-Thin Magnetic Films and Magnetic Nanostructures on Surfaces, in *NIC Symposium 2006*, edited by G. Münster, D. Wolf, and M. Kremer, volume 32 of *NIC*, pp. 151–158, Jülich, 2006, John von Neumann Institute for Computing.

[125] A. Kubetzka, P. Ferriani, M. Bode, S. Heinze, G. Bihlmayer, K. von Bergmann, O. Pietzsch, S. Blugel, and R. Wiesendanger, *Phys. Rev. Lett.* **94**, 087204 (2005).

[126] M. Przybylski and U. Gradmann, *Phys. Rev. Lett.* **59**, 1152 (1987).

[127] S. Heinze, M. Bode, A. Kubetzka, O. Pietzsch, X. Nie, S. Blugel, and R. Wiesendanger, *Science* **288**, 1805 (2000).

[128] S. Lebègue, A. Svane, M. I. Katsnelson, A. I. Lichtenstein, and O. Eriksson, *Phys. Rev. B* **74**, 045114 (2006).

[129] W. M. Lomer, *Proc. Phys. Soc.* **80**, 489 (1962).

[130] B. I. Halperin and T. M. Rice, *Solid State Physics*, volume 21, Academic Press Inc., New York, 1968.

[131] V. Y. IRKHIN and M. I. KATSNELSON, *Phys. Rev. B* **62**, 5647 (2000).

[132] V. Y. IRKHIN and M. I. KATSNELSON, *Z. Phys. B* **70**, 371 (1988).

[133] L. V. POUROVSKII, B. AMADON, S. BIERMANN, and A. GEORGES, *Phys. Rev. B* **76**, 235101 (2007).

[134] J. MINÁR, H. EBERT, C. DE NADAÏ, N. B. BROOKES, F. VENTURINI, G. GHIRINGHELLI, L. CHIONCEL, M. I. KATSNELSON, and A. I. LICHTENSTEIN, *Phys. Rev. Lett.* **95**, 166401 (2005).

[135] V. L. MORUZZI and P. M. MARCUS, *Phys. Rev. B* **48**, 7665 (1993), Brief Report.

[136] M. EDER, J. HAFNER, and E. G. MORONI, *Phys. Rev. B* **61**, 11492 (2000).

[137] J. HAFNER and D. SPIŠÁK, *Phys. Rev. B* **72**, 144420 (2005).

[138] N. E. ZEIN, *Phys. Rev. B* **52**, 11813 (1995).

[139] G. KOTLIAR and D. VOLLHARDT, *Physics Today* **57**, 53 (2004).

[140] T. JARLBORG, *Rep. Prog. Phys.* **60**, 1305 (1997).

[141] V. M. GALITSKII and A. B. MIGDAL, *Zh. Eksp. Teor. Fiz.* **34**, 139 (1958), Sov. Phys. JETP **7**, 96 (1958).

[142] W. H. PRESS, B. P. FLANNERY, S. A. TEUKOLSKY, and W. T. VETTERLING, *Numerical Recipes*, Cambridge University Press, Cambridge, England, 1986.

[143] O. SIPR, J. MINAR, S. MANKOVSKY, and H. EBERT, *Phys. Rev. B* **78**, 144403 (2008).

[144] I. DI MARCO, J. MINÁR, S. CHADOV, M. I. KATSNELSON, H. EBERT, and A. I. LICHTENSTEIN, *Physical Review B (Condensed Matter and Materials Physics)* **79**, 115111 (2009).

[145] S. BIERMANN, F. ARYASETIAWAN, and A. GEORGES, *Phys. Rev. Lett.* **90**, 086402 (2003).

[146] G. Y. GUO and H. H. WANG, *Chinese Journal of Physics* **38**, 949 (2000).

[147] M. ČERNÝ, J. POKLUDA, M. ŠOB, M. FRIÁK, and P. ŠANDERA, *Phys. Rev. B* **67**, 035116 (2003).

[148] M. ČENRÝ, *Materials Science and Engineering A* **462**, 432 (2007).

[149] T. BANDYOPADHYAY and D. D. SARMA, *Phys. Rev. B* **39**, 3517 (1989).

[150] F. D. MURNAGHAN, *Proc. Natl. Acad. Sci. USA* **30**, 244 (1944).

[151] F. BIRCH, **57**, 227 (1952).

[152] A. C. LAWSON, A. C. LARSON, M. C. ARONSON, Z. FISK, P. C. CAN-
FIELD, J. D. THOMPSON, R. B. VON DREELE, and S. JOHNSON, *J. Appl. Phys.* **76**, 7049 (1994).

[153] M. O'KEEFE and S. ANDERSON, *Acta Crystallogr., Sect. A: Cryst. Phys., Diffr., Theor. Gen. Crystallogr.* **33**, 914 (1977).

[154] Y. ENDOH and Y. ISHIKAWA, *J. Phys. Soc. Japan* **30**, 1614 (1971).

[155] B. SCHIRMER, B. FELDMANN, A. SOKOLL, Y. GAUTHIER, and M. WUT-
TIG, *Phys. Rev. B* **60**, 5895 (1999).

[156] T. OGUCHI and A. J. FREEMAN, *J. Magn. Magn. Mater.* **46**, L1 (1984).

[157] H. FUJIHISA and K. TAKEMURA, *Phys. Rev. B* **52**, 13257 (1995).

[158] D. HOBBS and J. HAFNER, *J. Phys.: Condens. Matter* **13**, L681 (2001).

[159] D. HOBBS, J. HAFNER, and D. SPIŠÁK, *Phys. Rev. B* **68**, 014407 (2003).

[160] J. HAFNER and D. HOBBS, *Phys. Rev. B* **68**, 014408 (2003).

[161] V. L. MORUZZI, P. M. MARCUS, and J. KÜBLER, *Phys. Rev. B* **39**, 6957 (1989).

[162] T. ASADA and K. TERAKURA, *Phys. Rev. B* **47**, 15992 (1993).

[163] Y. TSUNODA, N. OISHI, and N. KUNITOMI, *J. Phys. Soc. Jpn.* **53**, 359 (1984).

[164] P. KRÜGER, O. ELMOUHSSINE, C. DEMANGEAT, and J. C. PARLEBAS, *Phys. Rev. B* **54**, 6393 (1996).

[165] K. NAKAMURA, R. ARITA, Y. YOSHIMOTO, and S. TSUNEYUKI, *Phys. Rev. B* **74**, 235113 (2006).

[166] F. ARYASETIAWAN, K. KARLSSON, O. JEPSEN, and U. SCHÖNBERGER, *Phys. Rev. B* **74**, 125106 (2006).

[167] R. W. G. WYCKOFF, *Crystal Structure*, volume 19 of *Magnetic Properties of Metals*, Springer, Berlin, 1963.

[168] A. F. GUILLERMET and G. GRIMVALL, *Phys. Rev. B* **40**, 1521 (1989).

[169] B. L. GYORFFY, A. J. PINDOR, J. STAUNTON, G. M. STOCKS, and H. WINTER, *Journal of Physics F: Metal Physics* **15**, 1337 (1985).

[170] J. STAUNTON, B. L. GYORFFY, G. M. STOCKS, and J. WADSWORTH, *Journal of Physics F: Metal Physics* **16**, 1761 (1986).

[171] A. M. N. NIKLASSON, J. M. WILLS, M. I. KATSNELSON, I. A. ABRIKOSOV, O. ERIKSSON, and B. JOHANSSON, *Phys. Rev. B* **67**, 235105 (2003).

[172] M. JARRELL, *Phys. Rev. Lett.* **69**, 168 (1992).

[173] A. TOROPOVA, *Orbital Selective Mott Transition in* 3d *and* 5f *Materials*, PhD thesis, Rutgers State University of New Jersey, 2007.

[174] M. JARRELL, A. MACRIDIN, K. MIKELSONS, D. G. S. P. DOLUWEERA, and J. E. GUBERNATIS, The Dynamical Cluster Approximation with Quantum Monte Carlo Cluster Solvers, volume 1014, pp. 34–106, AIP, 2008.

[175] N. BLÜMER, Numerically exact Green function from Hirsch-Fye quantum Monte Carlo simulations, arXiv: 0712.1290v1, 2007.

[176] J.-P. JULIEN, J.-X. ZHU, and R. C. ALBERS, *Physical Review B (Condensed Matter and Materials Physics)* **77**, 195123 (2008).

[177] R. FRÉSARD and G. KOTLIAR, *Phys. Rev. B* **56**, 12909 (1997).

[178] A. W. SANDVIK, *Phys. Rev. B* **57**, 10287 (1998).

[179] T. MORIYA, *Spin Fluctuations in Itinerant Electron Magnetism*, Number 56 in Springer Series in Solid-State Science, Springer-Verlag, Berlin, Heidelberg, New York and Tokyo, 1985.

[180] I. HUGHES, *A First-Principles Approach to Modelling Magnetism in Strongly-Correlated Electron Systems*, PhD thesis, University of Warwick, 2007.

[181] J. B. STAUNTON, *Psik-highlight* (2007).

[182] P. SOVEN, *Phys. Rev.* **156**, 809 (1967).

[183] P. SOVEN, *Phys. Rev. B* **2**, 4715 (1970).

[184] J. F. L. HOPKINSON, J. B. PENDRY, and D. J. TITTERINGTON, *Comput. Phys. Commun.* **19**, 69 (1980).

[185] J. BRAUN and M. DONATH, *Journal of Physics: Condensed Matter* **16**, S2539 (2004).

[186] T. MIYAKE and F. ARYASETIAWAN, *Physical Review B (Condensed Matter and Materials Physics)* **77**, 085122 (2008).

[187] T. PAIVA, R. T. SCALETTAR, C. HUSCROFT, and A. K. MCMAHAN, *Phys. Rev. B* **63**, 125116 (2001).

[188] A. KOGA, N. KAWAKAMI, T. M. RICE, and M. SIGRIST, *Phys. Rev. B* **72**, 045128 (2005).

[189] M. VAN SCHILFGAARDE, T. KOTANI, and S. FALEEV, *Physical Review Letters* **96**, 226402 (2006).

[190] S. V. VONSOVSKY, *Magnetism*, volume 2, Wiley, New York, 1974.

[191] A. FREEMAN and D. KOELLING, *The Actinides: Electronic Structure and Related Properties*, volume 1, Academic Press, New York, 1974.

[192] P. S. RISEBOROUGH, *Adv. Phys.* **49**, 257 (2000).

[193] R. PARKS, *Valence Instabilities and Related Narrow-Band Phenomena*, Plenum Press, New York, 1977.

[194] E. MÜLLER-HARTMANN, B. RODEN, and D. WOHLLEBEN, editors, *Proceedings of the International Conference on Valence Fluctuations*, New York, 1981, Elsevier, Vols. 47-48.

[195] J. M. LAWRENCE, P. S. RISEBOROUGH, and R. D. PARKS, *Rep. Prog. Phys.* **44**, 1 (1981).

[196] C. M. VARMA, *Rev. Mod. Phys.* **48**, 219 (1976).

[197] P. WACHTER, *Handbook on the Physics and Chemistry of Rare Earth*, volume 19, Elseiver, New York, 1994, pp. 177-382.

[198] I. FELNER and I. NOWIK, *Phys. Rev. B* **33**, 617 (1986).

[199] K. W. H. STEVENS, *Journal of Physics C: Solid State Physics* **9**, 1417 (1976).

[200] V. Y. IRKHIN and M. I. KATSNELSON, *Solid State Commun.* **58**, 881 (1986).

[201] F. Reinert, R. Claessen, G. Nicolay, D. Ehm, S. Hüfner, W. P. Ellis, G.-H. Gweon, J. W. Allen, B. Kindler, and W. Assmus, *Phys. Rev. B* **58**, 12808 (1998).

[202] D. P. Moore, J. J. Joyce, A. J. Arko, J. L. Sarrao, L. Morales, H. Hochst, and Y. D. Chuang, *Phys. Rev. B* **62**, 16492 (2000).

[203] L. Moreschini, C. Dallera, J. J. Joyce, J. L. Sarrao, E. D. Bauer, V. Fritsch, S. Bobev, E. Carpene, S. Huotari, G. Vankó, G. Monaco, P. Lacovig, G. Panaccione, A. Fondacaro, G. Paolicelli, P. Torelli, and M. Grioni, *Physical Review B (Condensed Matter and Materials Physics)* **75**, 035113 (2007).

[204] J. N. Chazalviel, M. Campagna, G. K. Wertheim, and P. H. Schmidt, *Phys. Rev. B* **14**, 4586 (1976).

[205] T. Susaki, Y. Takeda, M. Arita, K. Mamiya, A. Fujimori, K. Shimada, H. Namatame, M. Taniguchi, N. Shimizu, F. Iga, and T. Takabatake, *Phys. Rev. Lett.* **82**, 992 (1999).

[206] A. Shigemoto, S. Imada, A. Sekiyama, A. Yamasaki, A. Irizawa, T. Muro, Y. Saitoh, F. Iga, T. Takabatake, and S. Suga, *J. Electron Spectrosc. Relat. Phenom.* **144-147**, 671 (2005).

[207] C. Dallera, M. Grioni, A. Shukla, G. Vankó, J. L. Sarrao, J. P. Rueff, and D. L. Cox, *Phys. Rev. Lett.* **88**, 196403 (2002).

[208] H. Yamaoka, N. Tsujii, K. Yamamoto, A. M. Vlaicu, H. Oohashi, H. Yoshikawa, T. Tochio, Y. Ito, A. Chainani, and S. Shin, *Physical Review B (Condensed Matter and Materials Physics)* **78**, 045127 (2008).

[209] A. Menth, E. Buehler, and T. H. Geballe, *Phys. Rev. Lett.* **22**, 295 (1969).

[210] F. Iga, N. Shimizu, and T. Takabatake, *J. Magn. Magn. Mater.* **177-181**, 337 (1998).

[211] A. Severing, E. Gratz, B. Rainford, and K. Yoshimura, *Physica B* **163**, 409 (1990).

[212] J. M. Lawrence, S. M. Shapiro, J. L. Sarrao, and Z. Fisk, *Phys. Rev. B* **55**, 14467 (1997).

[213] P. A. Alekseev, V. N. Lazukov, J. M. Mignot, and I. P. Sadikov, *Physica B* **281-282**, 34 (2000).

[214] K. S. Nemkovski, J.-M. Mignot, P. A. Alekseev, A. S. Ivanov, E. V. Nefeodova, A. V. Rybina, L.-P. Regnault, F. Iga, and T. Takabatake, *Physical Review Letters* **99**, 137204 (2007).

[215] I. Felner, I. Nowik, D. Vaknin, U. Potzel, J. Moser, G. M. Kalvius, G. Wortmann, G. Schmiester, G. Hilscher, E. Gratz, C. Schmitzer, N. Pillmayr, K. G. Prasad, H. de Waard, and H. Pinto, *Phys. Rev. B* **35**, 6956 (1987).

[216] R. L. Cohen, M. Eibschütz, and K. W. West, *Phys. Rev. Lett.* **24**, 383 (1970).

[217] A. Yaouanc, P. D. de Réotier, P. Bonville, G. Lebras, P. C. M. Gubbens, A. M. Mulders, and S. Kunii, *Europhysics Letters* **47**, 247 (1999).

[218] H. Okamura, T. Michizawa, T. Nanba, and T. Ebihara, *Physical Review B (Condensed Matter and Materials Physics)* **75**, 041101 (2007).

[219] G. Travaglini and P. Wachter, *Phys. Rev. B* **29**, 893 (1984).

[220] H. Okamura, S. Kimura, H. Shinozaki, T. Nanba, F. Iga, N. Shimizu, and T. Takabatake, *Phys. Rev. B* **58**, R7496 (1998).

[221] G. C. Allen and N. S. Hush, *Prog. Inorg. Chem.* **8**, 357 (1967).

[222] M. B. Robin and P. Day., *Adv. Inorg. Chem. Radiochem.* **10**, 247 (1967).

[223] A. Jayaraman, V. Narayanamurti, E. Bucher, and R. G. Maines, *Phys. Rev. Lett.* **25**, 368 (1970).

[224] M. B. Maple and D. Wohlleben, *Phys. Rev. Lett.* **27**, 511 (1971).

[225] L. M. Falicov and J. C. Kimball, *Phys. Rev. Lett.* **22**, 997 (1969).

[226] R. M. Martin and J. W. Allen, *Journal of Applied Physics* **50**, 7561 (1979).

[227] B. Bucher, Z. Schlesinger, P. C. Canfield, and Z. Fisk, *Phys. Rev. Lett.* **72**, 522 (1994).

[228] J. C. Cooley, M. C. Aronson, Z. Fisk, and P. C. Canfield, *Phys. Rev. Lett.* **74**, 1629 (1995).

[229] T. Kasuya, *Physica B* **223-224**, 402 (1996).

[230] K. Takegahara and T. Kasuya, *Journal of the Physical Society of Japan* **59**, 3299 (1990).

[231] H. Harima, S. Miyahara, and A. Yanase, *Physica B* **163**, 205 (1990).

[232] T. Saso and H. Kato, *Progress of Theoretical Physics* **87**, 331 (1992).

[233] V. N. Antonov, B. N. Harmon, and A. N. Yaresko, *Phys. Rev. B* **66**, 165209 (2002).

[234] T. Saso and H. Harima, *Journal of the Physical Society of Japan* **72**, 1131 (2003).

[235] A. Svane, *Solid State Commun.* **140**, 364 (2006).

[236] S. Lebègue, G. Santi, A. Svane, O. Bengone, M. I. Katsnelson, A. I. Lichtenstein, and O. Eriksson, *Phys. Rev. B* **72**, 245102 (2005).

[237] S. Lebègue, A. Svane, M. I. Katsnelson, A. I. Lichtenstein, and O. Eriksson, *Journal of Physics: Condensed Matter* **18**, 6329 (2006).

[238] X. Dai, K. Haule, and G. Kotliar, *Phys. Rev. B* **72**, 045111 (2005).

[239] O. Eriksson, M. S. S. Brooks, and B. Johansson, *Phys. Rev. B* **41**, 7311 (1990).

[240] C. Herring, *Exchange interactions among itinerant electrons*, volume 4 of *Magnetism*, Academic Press, New York, 1966.